Transport in open quantum systems

A thesis

submitted to

TATA INSTITUTE OF FUNDAMENTAL RESEARCH, MUMBAI, INDIA,

for the degree of

DOCTOR OF PHILOSOPHY

in

PHYSICS

by

ARCHAK PURKAYASTHA

International Centre for Theoretical Sciences

Tata Institute of Fundamental Research

Bangalore 560089, India

September 4, 2018

Declaration

This thesis is a presentation of my original research work. Wherever contributions of others are involved, every effort is made to indicate this clearly, with due reference to the literature, and acknowledgement of collaborative research and discussions. The work was done under the guidance of Professor Abhishek Dhar, at the International Centre for Theoretical Sciences, Tata Institute of Fundamental Research, Bangalore.

Archak Purkayastha

In my capacity as supervisor of the candidates thesis, I certify that the above statements are true to the best of my knowledge.

Prof. Abhishek Dhar

Date: 4. 9. 2018

Acknowledgements

I thank Madhumita for some of the schematic diagrams and for teaching me to draw the schematic diagrams. I also thank her for being the person continuously at the receiving end of my outbursts of joys and frustrations that are an inevitable part of a PhD life, thereby providing the much needed emotional support.

I thank my parents for their immense sacrifices and unyielding support. Any number of words I say in this respect is not enough.

Finally, I thank Prof. Spenta Wadia for building this beautiful institute in India. It is an Indian institute in whose name 'I' stands for 'International' and not 'Indian', and truly so.

Dedication

I dedicate my thesis to my parents.

Collaborators

- Most of the work in the thesis has been done with my thesis advisor Prof. Abhishek Dhar, and Prof. Manas Kulkarni.

- The work on linear open quantum system under a time-periodic drive from the bath has been done with Prof. Yonatan Dubi.

- The work on the Aubry-André-Harper model has had some contributions from Sambuddha Sanyal.

Contents

Publications related to this thesis

(i) Out-of-equilibrium open quantum systems: A comparison of approximate quantum master equation approaches with exact results, Archak Purkayastha, Abhishek Dhar, Manas Kulkarni, Phys. Rev. A **93**, 062114, (2016).

(https://doi.org/10.1103/PhysRevA.93.062114)

(ii) Quantum transport under AC drive from the leads : A Quantum Master Equation approach, Archak Purkayastha, Yonatan Dubi, Phys. Rev. B **96**, 085425 (2017).

(https://doi.org/10.1103/PhysRevB.96.085425)

(iii) Non-linear transport in an out-of-equilibrium single-site Bose Hubbard model: scaling, rectification and time dynamics, Archak Purkayastha, Abhishek Dhar, Manas Kulkarni, Phys. Rev. A **94**, 052134 (2016).

(https://doi.org/10.1103/PhysRevA.94.052134)

(iv) Anomalous transport in the Aubry-André-Harper model in isolated and open systems, Archak Purkayastha, Sambuddha Sanyal, Abhishek Dhar, Manas Kulkarni, Phys. Rev. B **97**, 174206 (2018)

(https://doi.org/10.1103/PhysRevB.97.174206)

(v) Non-equilibrium phase diagram of a 1D quasiperiodic system with a single-particle mobility edge, Archak Purkayastha, Abhishek Dhar, Manas Kulkarni, Phys. Rev. B **96**, 180204(R) (2017).

(https://doi.org/10.1103/PhysRevB.96.180204)

(vi) Current fluctuations is general open quantum systems and crossover to the isolated thermodynamic limit, Archak Purkayastha, arXiv:1712.01068v2 .

(https://arxiv.org/abs/1712.01068v2)

Chapter 1

Introduction

1.1   Background

Transport properties of materials are regularly measured in experiments. But, a microscopic theory for calculating transport properties is far from complete. For isolated systems in the thermodynamic limit, the standard linear response theory can be used to extract transport coefficients from various equilibrium correlation functions of the isolated system. An important virtue of this approach is to connect transport coefficients to spread of equilibrium correlations following a small perturbation. Such spread of correlations is routinely used to characterize transport behavior. However, in many experimental situations where the system is of finite size such an approach cannot be applied (for example, [1, 2, 3, 4, 5, 6, 7]). Such far-from-equilibrium set-ups beyond the validity of standard linear response approach are becoming increasingly of interest in both theory and experiments. Their investigation is important fundamentally [8, 9, 10] as well as for device applications such as optomechanical cooling [3], masing (microwave lasing) [11], amplification of light [4], rectification of bosonic and fermionic currents [12, 13, 14] etc.

For describing transport properties in such set-ups we need the open (quantum) system approach. This involves connecting the system to baths which have different temperatures and chemical potentials and looking at the non-equilibrium steady state (NESS) currents. This approach of describing transport is more akin to the standard experimental set-up for measuring electrical conductance. In this approach there is no restriction on system size. It can be applied to finite-size and extended systems alike. However, for extended systems, where the standard linear response theory is also applicable, a rigorous relation between the two approaches has been missing.
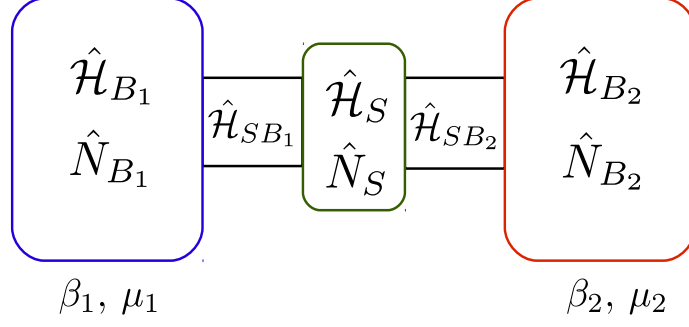
Figure 1.1: *The general set-up for obtaining open system transport. $\hat{N}_S, \hat{N}_{B_1}, \hat{N}_{B_2}$ are operators corresponding to total number of particles in system, left bath and right bath. The initial state of the set-up is the direct product state of an arbitrary state of the system with thermal states of the two baths. β_1, μ_1 (β_2, μ_2) are the temperatures and chemical potentials of the initial thermal state of the left (right) bath.*

1.2   The general idea

Let us now present the general idea for obtaining quantum transport via open quantum set-ups. Consider the set-up described by the Hamiltonian,

$$\hat{\mathcal{H}} \equiv \hat{\mathcal{H}}_{B_1} + \hat{\mathcal{H}}_{SB_1} + \hat{\mathcal{H}}_S + \hat{\mathcal{H}}_{SB_2} + \mathcal{H}_{B_2}. \tag{1.1}$$

Here $\hat{\mathcal{H}}_S$ is the system of interest, $\hat{\mathcal{H}}_{B_1}$ and $\hat{\mathcal{H}}_{B_2}$ are two baths which are attached to the system of interest via the system-bath coupling Hamiltonians $\hat{\mathcal{H}}_{SB_1}$, $\hat{\mathcal{H}}_{SB_2}$. In our microscopic theories of transport, we model each bath via a quadratic Hamiltonian with infinite degrees of freedom (fermionic or bosonic). Moreover, the system-bath coupling will always be considered bilinear. The full system+bath set-up described by $\hat{\mathcal{H}}$ is considered isolated. All Hamiltonians considered in this thesis will be particle number conserving and having time-reversal symmetry. The initial state of the whole system+bath set-up is chosen as a direct product state of the system and the baths, each bath being in its own thermal state with its own temperature and chemical potential.

$$\rho_{tot}(0) = \frac{e^{-\beta_1(\hat{\mathcal{H}}_{B_1} - \mu_1 \hat{N}_{B_1})}}{Tr(e^{-\beta_1(\hat{\mathcal{H}}_{B_1} - \mu_1 \hat{N}_{B_1})})} \otimes \rho(0) \otimes \frac{e^{-\beta_2(\hat{\mathcal{H}}_{B_2} - \mu_2 \hat{N}_{B_2})}}{Tr(e^{-\beta_2(\hat{\mathcal{H}}_{B_2} - \mu_2 \hat{N}_{B_2})})}, \tag{1.2}$$

where $\rho(0)$ is the initial density matrix of the system and $\rho_{tot}(0)$ is the initial density matrix of the whole system+bath set-up. The schematic of the set-up is given in Fig. 1.1. This set-up is now evolved with the full system+bath Hamiltonian $\hat{\mathcal{H}}$ and evolution of

the system state is obtained by tracing out the bath degrees of freedom,

$$\rho_{tot}(t) = e^{-i\hat{\mathcal{H}}t}\rho_{tot}(0)e^{i\hat{\mathcal{H}}t}, \ \ \rho(t) = Tr_B(\rho_{tot}(t)), \tag{1.3}$$

where $Tr_B(...)$ refers to tracing over bath degrees of freedom. The expectation value of some system observable of interest, $\hat{O}$, is calculated in the evolved state, $\langle\hat{O}(t)\rangle = Tr(\hat{O}\rho(t))$. The entire protocol can be straightforwardly extended to cases where there are multiple (i.e, more than two) baths attached to the system.

If the temperatures and chemical potentials of the initial states of the baths are different, in all the cases of our interest, in the long time limit, a unique non-equilibrium steady state (NESS) will be reached which is independent of the initial state of the system. This is generically expected [15, 16]. There may be cases where this does not happen [15, 17, 18], but those cases are outside the scope of this thesis. We will look at energy and particle transport properties.

Several formalisms exist in the literature for studying open quantum set-ups, such as, non-equilibrium Greens functions (NEGF) [19], quantum Langevin equations (QLE) [20, 15, 16], quantum master equations (QME) [21, 22, 23] etc. This thesis is based on QME and QLE approaches. Though the set-up described above is for two baths, some of the formalisms we will develop in the thesis will be for an arbitrary number of baths attached to the system. In this thesis, we will

- investigate and improve the QME approach to quantum transport and give the connection between the QME and QLE formalisms for obtaining transport properties of various set-ups [Publications related to the thesis (i), (ii)],

- apply our improved formalisms to some small quantum systems thereby discovering rich and interesting physics, much of which would be missed or would be harder to obtain by other formalisms [Publications related to the thesis (i), (iii), (ii)],

- explore transport behavior in 1D quasiperiodic systems, obtaining their high temperature non-equilibrium phase diagrams, and explicitly showing a case where open system approach and standard linear response theory give very different results [Publications related to the thesis (iv), (v)],

- explore the connection between transport properties obtained via the standard linear response theory for isolated systems and via the open system approach [Publications related to the thesis (vi)].

1.3   Outline

This thesis is organized as follows.

Chapter 2: Formalism   In this chapter, first we provide the necessary background for Markovian QMEs. We discuss the Lindblad form of the Markovian QME as well as the Redfield QME (RQME) which is obtained via Born-Markov approximation. Then we review the QLE formalism for a very general non-interacting system in arbitrary dimensions and geometry with arbitrary number of sites attached to baths. The QLE formalism can be used to easily obtian exact (i.e. without Born-Markov approximation) steady state results. After that, we explore the same general non-interacting set-up under the Born-Markov approximation. We show the equivalence between QLE and RQME in such set-ups. Finally, we extend the RQME to the AC case, where the temperatures and chemical potentials of the baths are periodic functions of time.

Chapter 3: Transport through small systems   In this chapter, first we apply the Born-Markov approximated formalism developed in the previous chapter to the simple case of a two site non-interacting system connected to two baths. We use this simple case to test the Born-Markov approximated results against exact results. We also compare the results with two other phenomenologically written Lindblad QMEs which are often used. The RQME has a much wider range of validity than the Lindblad QMEs. For the AC case, we obtain several experimentally relevant results, such as hysteresis-like loops of instantaneous current vs voltage plots. Then, we employ the RQME approach to a simple interacting system of a single site with Bose-Hubbard interaction connected to two baths at different temperatures. We obtain extremely interesting rectification effects and high temperature scaling. We also find that the time to reach steady state has non-trivial dependences on interaction strength and temperatures of the baths.

Chapter 4: Transport in extended systems   In this chapter, first we review the ways of characterizing transport via standard linear response theory and via the open system approach. We then look at transport through two 1D quasiperiodic systems, the Aubry-André-Harper model and a generalization of it. We show that at the critical point of the Aubry-André-Harper model, the standard linear response theory characterization of transport and the open system characterization of transport give drastically different

results. The open system result can be understood as a property of system single particle eigenfucntions in terms of the simple expression for current derived in Chapter 2. For the generalized model, we obtain the high temperature non-equilibrium phase diagram, which can be explained by its connections with the Aubry-André-Harper model and the fractal properties of the spectrum. Finally, we derive open system current fluctuation-dissipation relations for general open quantum set-ups and give the relation between standard linear response theory and open system approaches of characterizing transport.

Chapter 5: Conclusions   This gives the summary and the concluding remarks of the thesis.

Chapter 2

Formalism

In this chapter, we first review and discuss the standard QME and the QLE approaches in sections 2.1,2.2. Then, in section 2.3, we formulate a microscopically derived QME approach for a very general non-interacting set-up for both DC and AC transport cases under weak system-bath coupling and Markovian assumptions (Born-Markov approximation). We show the equivalence of QME and QLE approaches for such set-ups. We obtain various general results that are valid in arbitrary geometry and dimensions. This chapter is dedicated to development of the formalisms only, along with some physics that can be directly read-off from the resulting equations. The explicit application of the formalisms as well as the numerical checks validating the formalisms will be taken up in subsequent chapters.

2.1   Review: Markovian Quantum Master Equations (QMEs)

Quamtum Master Equaiton (QME) is an equation of motion for the density matrix of an open system. In this thesis, we will only consider Markovian QMEs (see Appendix. 6.1 for a definition of quantum Markov process). There exists exact non-Markovian QMEs also, which give formally exact results (for example, [24]). However, non-Markovian QMEs are much more difficult to solve numerically. When the Markovian approximation holds, the Markovian QMEs provide huge simplification (as we will see).

2.1.1 Lindblad QME

Gorini, Kossakowski, Sudarshan [25] and Lindblad [26] (GKSL) mathematically proved a theorem which says that when a non-unitary term is added to the unitary equation of motion for the density matrix such that the resulting equation is Markovian and preserves all properties of the density matrix at all time for all initial conditions, the resulting equation has to be of the form

$$\frac{\partial \rho}{\partial t} = i[\rho, \hat{H}] + \sum_{\alpha, \nu} \mathfrak{g}_{\alpha\nu} \big(\hat{\mathfrak{D}}_\alpha \rho \hat{\mathfrak{D}}_\nu^\dagger - \frac{1}{2} \{ \hat{\mathfrak{D}}_\nu^\dagger \hat{\mathfrak{D}}_\alpha, \rho \} \big). \tag{2.1}$$

Here $\mathfrak{g}_{\alpha\nu}$ are elements of matrix $\mathfrak{g}$ which is Hermitian and positive semi-definite, $\hat{H}$ is a Hermitian system operator encoding the unitary part of the time evolution, and $\hat{\mathfrak{D}}_\alpha$ is some system operator. Here and henceforth, we set $\hbar = 1$. $\mathfrak{g}$ being positive semi-definite is the necessary and sufficient condition for the complete positivity of the density matrix ρ at all time. This point will be important later. We will call the Eq. 2.1 as a QME of the GKSL form.

Eq. 2.1 can be further simplified by diagonalizing $\mathfrak{g}$ and defining new operators $\hat{D}_m$,

$$\sum_{\alpha, \nu} U_{m\alpha} \mathfrak{g}_{\alpha\nu} U_{p\nu}^* = \gamma_m \delta_{mp}, \quad \hat{D}_m \equiv \sum_\nu U_{m\nu} \mathfrak{D}_\nu. \tag{2.2}$$

The resulting equation is commonly called the Lindblad QME and has the form

$$\frac{\partial \rho}{\partial t} = i[\rho, \hat{H}] + \sum_m \gamma_m \big(\hat{D}_m \rho \hat{D}_m^\dagger - \frac{1}{2} \{ \hat{D}_m^\dagger \hat{D}_m, \rho \} \big) \tag{2.3}$$

with $\gamma_m \geq 0$ for all m now being the requirement to preserve complete positivity. The operators $\{\hat{D}_m\}$ are often called Lindblad operators. Note that the Lindblad operators are not specified. The Lindblad QME is widely used across many fields in physics. In most applications of the Lindblad QME, the Lindblad operators are written down phenomenologically. *In this thesis, we do not use this approach, except for comparison with the other approaches described below.* Instead, we will use the Redfield QME which can be rigorously derived from a microscopic system+bath Hamiltonian approach via Nakajima-Zwanzig projection operators method under Born-Markov approximation (Appendix. 6.2,[21]).

2.1.2 Redfield QME (RQME): Born-Markov approximation

Born-approximation corresponds to deriving QMEs up to leading order in system-bath coupling. We take the rigorously derived time-convolution-less QME up to second order

11

(which is the leading order) in system-bath coupling (Appendix. 6.2),

$$\frac{\partial\rho}{\partial t} = i[\rho, \hat{\mathcal{H}}_S] - \varepsilon^2 \int_0^{t-t_0} dt' Tr_B[\hat{\mathcal{H}}_{SB}, [\hat{\mathcal{H}}_{SB}^I(-t'), \rho(t) \otimes \rho_B]], \qquad (2.4)$$

where $\hat{\mathcal{H}}_{SB}^I(t') = e^{i(\hat{\mathcal{H}}_S + \hat{\mathcal{H}}_B)t} \hat{\mathcal{H}}_{SB} e^{-i(\hat{\mathcal{H}}_S + \hat{\mathcal{H}}_B)t}$. Now, we do the Markov approximation, i.e, we only look at long time dynamics such that $t_0 \to -\infty$. Reducing to this actually makes the assumption that observation time t is much larger than the decay time scale of some bath-correlations. To see this, we note that any system-bath coupling Hamiltonian can be written in the following form,

$$\hat{\mathcal{H}}_{SB} = \sum_\ell \hat{S}_\ell \hat{B}_\ell \qquad (2.5)$$

where $\hat{S}_\ell$ is some system operator, and $\hat{B}_\ell$ is some bath operator. Using this in Eq. 2.4 and after some simplification we obtain [21, 23]

$$\frac{\partial\rho}{\partial t} = i[\rho, \hat{\mathcal{H}}_S]$$
$$- \varepsilon^2 \int_0^{t-t_0} dt' \sum_{\ell,m} \left([\hat{S}_\ell, \hat{S}_m(-t')\rho(t)] \langle \hat{B}_\ell \hat{B}_m(-t') \rangle_B + [\rho(t)\hat{S}_m(-t'), \hat{S}_\ell] \langle \hat{B}_m(-t')\hat{B}_\ell \rangle_B \right),$$
$$(2.6)$$

where $\hat{S}_m(t) = e^{i\hat{\mathcal{H}}_S t} \hat{S}_m e^{-i\hat{\mathcal{H}}_S t}$, $\hat{B}_m(t) = e^{i\hat{\mathcal{H}}_B t} \hat{B}_m e^{-i\hat{\mathcal{H}}_B t}$ and $\langle ... \rangle_B = Tr(\rho_B...)$. Let τ_B be the bath relaxation time scale, defined as the time in which all the $\langle \hat{B}_\ell \hat{B}_m(-t') \rangle_B$ and $\langle \hat{B}_m(-t')\hat{B}_\ell \rangle_B$ decay to $O(\varepsilon)$. Since, within Born approximation we are anyway neglecting higher orders of ε, contributions smaller than $O(\varepsilon)$ from $\langle \hat{B}_\ell \hat{B}_m(-t') \rangle_B$ and $\langle \hat{B}_m(-t')\hat{B}_\ell \rangle_B$ are irrelevant. If $t - t_0 \gg \tau_B$, it is justified to take $t_0 \to -\infty$, thereby making the Markovian approximation. Note that τ_B depends only on properties of the bath, and not on any system properties. Thus, finally, we have the Born-Markov approximated QME, which is the RQME,

$$\frac{\partial\rho}{\partial t} = i[\rho, \hat{\mathcal{H}}_S]$$
$$- \varepsilon^2 \int_0^\infty dt' \sum_{\ell,m} \left([\hat{S}_\ell, \hat{S}_m(-t')\rho(t)] \langle \hat{B}_\ell \hat{B}_m(-t') \rangle_B + [\rho(t)\hat{S}_m(-t'), \hat{S}_\ell] \langle \hat{B}_m(-t')\hat{B}_\ell \rangle_B \right).$$
$$(2.7)$$

Eq. 2.7 is the one of the important equations used in the first part of the thesis. Various results will be obtained simply by using Eq. 2.7 for specific models.

2.1.3 Accuracy of the RQME

The RQME is an equation of the form

$$\frac{\partial \rho}{\partial t} = \left(\mathcal{L}_{[0]} + \mathcal{L}_{[2]} \right) \rho(t), \tag{2.8}$$

where $\mathcal{L}_{[p]}$ is the Liovillian of order ε^p. $\mathcal{L}_{[0]}\bullet = i[\bullet, \hat{\mathcal{H}}_S]$. This has the solution

$$\rho(t) = e^{(\mathcal{L}_{[0]} + \mathcal{L}_{[2]})t} \rho(0). \tag{2.9}$$

Even though the equation was derived correct to $O(\varepsilon^2)$, the solution has answers to all orders of ε. Clearly, the solution is not accurate to all orders. The question we now ask is up to how many orders in ε can the solution of the RQME be trusted. The naive expectation for this is up to $O(\varepsilon^2)$. However, this is not true. It has been succinctly shown in Ref. [27] that an equation of this form will give diagonal elements in the eigenbasis of system Hamiltonian correct to $O(\varepsilon^0)$ and off-diagonal elements correct to $O(\varepsilon^2)$.

2.1.4 Difference between RQME and Lindblad QMEs

Since, the RQME is a Markovian equation of motion for the density matrix of the system, one can expect that RQME for any given set-up will be reducible to the Lindblad form (Eq. 2.1 or Eq. 2.3). But this is not true in general and holds only under very special conditions. For example, if the system is a single harmonic oscillator, then the RQME is exactly of the Lindblad form (Eq. 2.3). However, for even slightly more complicated systems, for example, a system consisting of two coupled harmonic oscillators, the RQME has a form similar to Eq. 2.1, but some γ_m's may be < 0. As a result the RQME may not preserve complete positivity of system density matrix at all time under specific conditions [21, 22, 23]. The positivity problem of the RQME remains a major issue, and one has to be careful in applying the RQME. This drawback often does not show up in physical quantities and the RQME is widely used. In many cases, however, the phenomenological Lindblad QMEs are preferred over RQME because RQME is numerically more difficult.

In this thesis, we will provide a simple way to handle RQME for non-interacting set-ups, and also use RQME to extract analytical non-equilibrium results in a simple interacting problem.
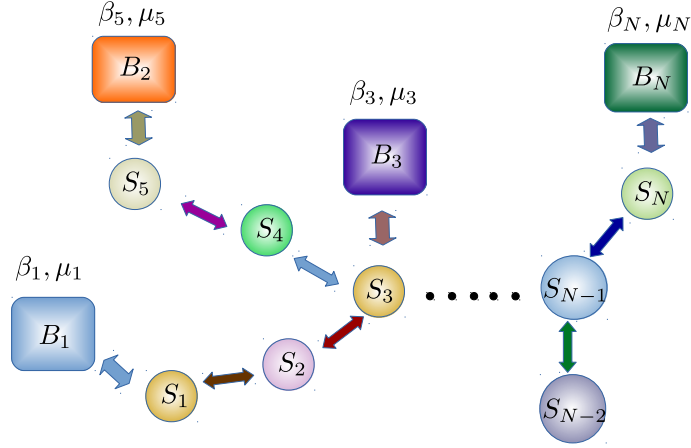
Figure 2.1: *The schematic diagram for our general non-interacting set-up. S_p represents the pth site of the system attached. B_p represents the bath with inverse temperature and chemical potential β_p, μ_p that is attached to the pth site of the system. The sites and the baths can be all fermionic or bosonic. The on-site energies of the sites are arbitrary. The arrows represent the hopping between the sites. The hopping strengths are also arbitrary. An arbitrary number of sites are attached to the baths.*

2.2   Review: Quantum Langevin Equation

Having reviewed Markovian QMEs, we now review the Quantum Langevin Equation (QLE) formalism. This formalism that will be extensively used in the thesis to obtain exact non-equilibrium steady states (NESS), is based on Heisenberg equations of motion. It gives exact results for NESS if the system Hamiltonian is quadratic, i.e, for non-interacting systems [20, 15, 16]. In this approach, the Heisenberg equations of motion for the bath degrees of freedom are first formally solved. This solution is then used in writing the Heisenberg equations of motion for the system degrees of freedom. The resulting system equations of motion has the form a generalised Langevin equation with colored noise and non-Markovian dissipation. The NESS properties are easily obtained exactly by solving the equations of motion by Fourier transform. For non-interacting systems, this approach is exactly equivalent to the NEGF approach [15].

A general non-interacting set-up is written as

$$\hat{\mathcal{H}}_S = \sum_{\ell m} \mathbf{H}^S_{\ell m} \hat{a}^\dagger_\ell \hat{a}_m, \;\; \hat{\mathcal{H}}_B = {\sum_\ell}' \sum_{r=1}^\infty \Omega_{\ell r} \hat{B}^\dagger_{\ell r} \hat{B}_{\ell r}, \;\;\; \hat{\mathcal{H}}_{SB} = {\sum_\ell}' \sum_r \kappa_{\ell r} (\hat{B}^\dagger_{\ell r} \hat{a}_\ell + \hat{a}^\dagger_\ell \hat{B}_{\ell r}),$$

(2.10)

where $\sum'_\ell$ denotes sum over the sites ℓ of the system where the baths are attached. $\hat{B}_{\ell r}$ is the annihilation operator of the $r$the mode of the bath attached to site ℓ with coupling strength $\kappa_{\ell r}$ and $\hat{a}_\ell$ is the annihilation operator of the system at site ℓ. Either all operators are bosonic or all operators are fermionic. $\mathbf{H}^S$ is a symmetric matrix. In general, if $\hat{\mathcal{H}}_S$ did not have time-reversal symmetry, $\mathbf{H}^S$ would have been a Hermitian matrix. But, in this thesis, we will restrict ourselves to systems with time reversal symmetry. However, the formalisms discussed can be straightforwardly carried over to cases without time-reversal symmetry. A schematic diagram of the set-up is given in Fig. 2.1.

The set-up is initially taken to be at a direct product state with each bath being at its own thermal state with corresponding temperature and chemical potential. This, of course, assumes that such thermal state is well-defined for the bath Hamiltonians, and pathological cases where the bath Hamiltonians do not have a minimum of energy are to be excluded. In the QLE approach, we will work in Heisenberg picture where the operators evolve but density matrix does not evolve. Thus the initial state has thermal properties

$$\langle \hat{B}_{\ell r}(0) \rangle = 0, \quad \langle \hat{B}^\dagger_{\ell r}(0) \hat{B}_{\ell s}(0) \rangle = \mathfrak{n}_\ell(\Omega_{\ell r})\delta_{rs}, \quad \mathfrak{n}_\ell(\omega) = [e^{\beta_\ell(\omega - \mu_\ell)} \pm 1]^{-1}, \qquad (2.11)$$

where $\mathfrak{n}_\ell(\omega)$ is the fermionic or bosonic distribution function. We also introduce the bath spectral functions

$$\mathfrak{J}_\ell(\omega) = 2\pi \sum_r \mid \kappa_{\ell r} \mid^2 \delta(\omega - \Omega_{\ell r}). \qquad (2.12)$$

We will assume that the baths are such that the bath spectral functions can be well-approximated as a continuous function of ω. The set-up described by Eqs. 2.10, 2.11, is an extremely general non-interacting set-up, and can be in arbitrary lattice in arbitrary dimensions and geometry with arbitrary number of sites attached to baths. In this chapter, henceforth, we will only look at this set-up in great detail.

The system Hamiltonian can be diagonalized in single particle basis by diagonalizing $\mathbf{H}^S$. Let Φ be the orthogonal matrix diagonalizing $\mathbf{H}^S$,

$$\mathbf{D} = \Phi^T \mathbf{H}^S \Phi, \qquad (2.13)$$

where $\mathbf{D}$ is a diagonal matrix with the elements ω_ν, which are the single-particle energy eigenvalues. The eigenbasis annihilation operators are defined via $\hat{A}_\nu = \sum_\ell \Phi_{\ell\nu} \hat{a}_\ell \Rightarrow \hat{a}_\ell = \sum_\nu \Phi_{\ell\nu} \hat{A}_\nu$. In terms of eigenbasis operators we have,

$$\hat{\mathcal{H}}_S = \sum_\nu \omega_\nu \hat{A}^\dagger_\nu \hat{A}_\nu, \quad \hat{\mathcal{H}}_{SB} = \sum_\ell{}' \sum_{r,\nu} \kappa_{\ell r} \Phi_{\ell\nu} (\hat{B}^\dagger_{\ell r} \hat{A}_\nu + \hat{A}^\dagger_\nu \hat{B}_{\ell r}) \qquad (2.14)$$

. The QLE can be derived either in the eigenbasis (i.e, in terms of the operators $\hat{A}_\nu$) or in the real basis (i.e, in terms of the operators $\hat{a}_\ell$). For future reference, we will here give the derivation in the eigenbasis. The corresponding derivation in the real basis can be found in [15].

The Heisenberg equation of motions for the bath operators and the system operators in our set-up are given by

$$\frac{d\hat{B}_{\ell r}}{dt} = -i\Omega_{\ell r}\hat{B}_{\ell r}(t) - i\kappa_{\ell r}\sum_\nu \Phi_{\ell\nu}\hat{A}_\nu(t),$$

$$\frac{d\hat{A}_\nu}{dt} = -i\omega_\nu\hat{A}_\nu(t) - i\sum_\ell{}' \sum_r \kappa_{r\ell}\Phi_{\ell\nu}\hat{B}_{\ell r}(t). \tag{2.15}$$

We can formally solve the equation of motion for the bath operators to obtain

$$\hat{B}_{\ell r}(t) = e^{-i\Omega_{\ell r}t}\hat{B}_{\ell r}(0) - i\kappa_{\ell r}\sum_{\nu=1}^N \Phi_{\ell\nu}\int_0^t dt'\, e^{-i\Omega_{\ell r}(t-t')}\hat{A}_\nu(t'). \tag{2.16}$$

Using this formal solution in the equation of motion for system operators, and using Eq. 2.12 we get the exact quantum Langevin equation

$$\frac{d\hat{A}_\nu}{dt} = -i\omega_\nu\hat{A}_\nu(t) - i\hat{\xi}_\nu(t) - \sum_\ell{}' \sum_\sigma \Phi_{\ell\nu}\Phi_{\ell\sigma}\int_0^t \mathfrak{f}_\ell(t-t')\hat{A}_\sigma(t')dt' \tag{2.17}$$

where

$$\mathfrak{f}_\ell(t) = \int\frac{d\omega}{2\pi}\mathfrak{J}_\ell(\omega)e^{-i\omega t}, \quad \hat{\xi}_\nu(t) = \sum_\ell{}' \sum_r \Phi_{\ell\nu}\kappa_{\ell r}\hat{B}_{\ell r}(0)e^{-i\Omega_{\ell r}t}. \tag{2.18}$$

From the initial bath correlation functions, we have,

$$\langle\hat{\xi}_\nu(t)\rangle = 0, \quad \langle\hat{\xi}_\nu^\dagger(t)\hat{\xi}_\sigma(t')\rangle = \sum_\ell{}' \Phi_{\ell\nu}\Phi_{\ell\sigma}\mathfrak{F}_\ell(t-t'), \quad \mathfrak{F}_\ell(t) = \int\frac{d\omega}{2\pi}\mathfrak{J}_\ell(\omega)\mathfrak{n}_\ell(\omega)e^{i\omega t}. \tag{2.19}$$

Thus $\hat{\xi}_\nu(t)$ is the colored noise operator of the quantum Langevin equation, and the noise comes from the thermal fluctuations in the initial condition. In this thesis, Eq. 2.17 will be used as a the starting point in analytical comparison between RQME and QLE.

Eq. 2.17 can be easily solved for steady state by taking long time limit and Fourier transforming to frequency space. Let

$$\hat{A}_\nu(t) = \int_{-\infty}^\infty \frac{d\omega}{2\pi}\hat{\tilde{A}}_\nu(\omega)e^{-i\omega t}, \quad \hat{\xi}_\nu(t) = \int_{-\infty}^\infty \frac{d\omega}{2\pi}\hat{\tilde{\xi}}_\nu(\omega)e^{-i\omega t}. \tag{2.20}$$

It can be checked that $\hat{\tilde{\xi}}_\nu(\omega)$ satisfies

$$\langle\hat{\tilde{\xi}}_\nu^\dagger(\omega)\hat{\tilde{\xi}}_\sigma(\omega')\rangle = 4\pi F_{\nu\sigma}(\omega)\delta(\omega-\omega'), \quad F_{\nu\sigma}(\omega) = \sum_\ell{}' \Phi_{\ell\nu}\Phi_{\ell\sigma}\frac{\mathfrak{J}_\ell(\omega)\mathfrak{n}_\ell(\omega)}{2}. \tag{2.21}$$

16

Eq. 2.17 written after taking $t \to \infty$ and Fourier transforming gives

$$(\omega - \omega_\nu)\hat{\tilde{A}}_\nu(\omega) + \sum_\sigma v_{\nu\sigma}(\omega)\hat{\tilde{A}}_\sigma(\omega) = \hat{\tilde{\xi}}_\nu(\omega), \tag{2.22}$$

where

$$f_{\nu\sigma}(\omega) = \sum_\ell{}' \Phi_{\ell\nu}\Phi_{\ell\sigma}\frac{\mathfrak{J}_\ell(\omega)}{2}, \quad f^\Delta_{\nu\sigma}(\omega) = \mathcal{P}\int\frac{d\omega'}{\pi}\frac{f_{\nu\sigma}(\omega')}{\omega' - \omega}, \tag{2.23}$$

where $\mathcal{P}$ denotes principal value. Eq. 2.22 can be written in matrix notation as

$$(\omega\mathbb{I} - \mathbf{D} + \mathbf{f}(\omega) + i\mathbf{f}^\Delta(\omega))\tilde{A}_{vec}(\omega) = \tilde{\xi}_{vec}(\omega), \tag{2.24}$$

where $\mathbb{I}$ is N dimensional identity matrix, $\mathbf{D}$ is as defined in Eq. 2.13, $\tilde{A}_{vec}(\omega)$ and $\tilde{\xi}_{vec}(\omega)$ are N dimensional column vectors with elements $\{\hat{\tilde{A}}_\nu(\omega)\}$ and $\{\hat{\tilde{\xi}}_\nu(\omega)\}$ respectively, and $\mathbf{f}(\omega)$ and $\mathbf{f}^\Delta(\omega)$ are matrices $N\mathrm{x}N$ with elements $\{f_{\nu\sigma}(\omega)\}$ and $\{f^\Delta_{\nu\sigma}(\omega)\}$ respectively. At this stage, one can go back from the eigenbasis to the real space basis,

$$\Phi(\omega\mathbb{I} - \mathbf{D} + \mathbf{f}(\omega) + i\mathbf{f}^\Delta(\omega))\Phi^T\Phi\tilde{A}_{vec}(\omega) = \Phi\tilde{\xi}_{vec}$$
$$\Rightarrow (\omega\mathbb{I} - \mathbf{H}^S - \mathbf{\Sigma}(\omega))\tilde{a}_{vec}(\omega) = \tilde{\eta}_{vec}(\omega), \tag{2.25}$$

with $\tilde{a}_{vec}(\omega) = \Phi\tilde{A}_{vec}(\omega)$, $\tilde{\eta}_{vec}(\omega) = \Phi\tilde{\xi}_{vec}$, $\mathbf{\Sigma}(\omega) = \Phi\mathbf{f}(\omega) + i\mathbf{f}^\Delta(\omega)\Phi^T$.

$$\tilde{a}_{vec}(\omega) = \mathbb{G}(\omega)\tilde{\eta}_{vec}(\omega),$$
$$\mathbb{M}(\omega) = \omega\mathbb{I} - \mathbf{H}^S - \mathbf{\Sigma}(\omega), \quad \mathbb{G}(\omega) = \mathbb{M}(\omega)^{-1}. \tag{2.26}$$

$\mathbf{\Sigma}(\omega)$ is called the bath self-energy matrix. It is a diagonal matrix with the only non-zero elements

$$\mathbf{\Sigma}_{pp}(\omega) = -\mathcal{P}\int\frac{d\omega'\mathfrak{J}_p(\omega')}{2\pi(\omega' - \omega)} - \frac{i}{2}\mathfrak{J}_p(\omega), \tag{2.27}$$

where p labels a site attached to a bath. $\mathbb{G}(\omega)$ is exactly the same Green's function as obtained from the NEGF formalism [19], [15]. $\tilde{\eta}_{vec}(\omega)$ is the 'noise' vector with non-zero elements $\hat{\tilde{\eta}}_p(\omega)$, where, again p labels a site attached to a bath. $\hat{\tilde{\eta}}_p(\omega)$ has the property

$$\langle\hat{\tilde{\eta}}^\dagger_p(\omega)\hat{\tilde{\eta}}_q(\omega')\rangle = 2\pi\mathfrak{J}_p(\omega)\mathfrak{n}_p(\omega)\delta(\omega - \omega')\delta_{pq}. \tag{2.28}$$

$\tilde{a}_{vec}(\omega)$ is a vector containing the Fourier transformed operators $\hat{\tilde{a}}_\ell(\omega) = \int dt\hat{a}_\ell(t)e^{i\omega t}$.

Though the steady state can be easily calculated exactly via QLE, transient dynamics of approach to steady state is much more difficult to obtain via QLE than by QME methods. This is because one would require a Laplace transform instead of a Fourier transform,

17

and inverting a Laplace transform is quite challenging numerically. It is here that the Born-Markov approximaiton becomes useful, simplifying the problem of obtaining time-dynamics significantly. In the following, we will look into the general non-interacting system in Eq. 2.10 under Born-Markov approximation.

2.3 Non-interacting systems under Born-Markov approximation

We now look at treatment of the same general non-interacting set-up as in Eq. 2.10 under the Born-Markov approximation. To do this, we will need weak system-bath coupling, i.e,

$$\hat{\mathcal{H}}_{SB} \to \varepsilon \hat{\mathcal{H}}_{SB}, \tag{2.29}$$

where $\varepsilon \ll 1$ is the small parameter. Apart from this, all other Hamiltonians are exactly same as in Eq. 2.10.

We will first look at the 'DC case', which is the case discussed above. By 'DC case', we mean that the temperatures and chemical potentials of the baths are not functions of time. This is in contrast with the 'AC case' which will be discussed next, where temperatures and chemical potentials of the baths will be periodic functions of time.

2.3.1 DC case

We do the Born-Markov approximation on the general non-interacting set-up defined by Eqs. 2.10, 2.11, 2.12 in two different methods. The first is by using the RQME Eq. 2.7, and the second is via directly doing the approximations on top of the QLE equation Eq. 2.17. Both give exactly same result, but the QLE approach makes the meaning of the Markov approximation more explicit.

RQME

Using Eq. 2.7 to treat the set-up gives,

$$
\begin{aligned}
\frac{\partial \rho}{\partial t} =& i[\rho, \hat{\mathcal{H}}_S^{eff}] + \varepsilon^2 \sum_{\alpha,\nu=1}^{N} [Q_{\alpha\nu}^* \mp (v_{\alpha\nu} + v_{\nu\alpha}^*)] \, (\hat{A}_\nu \rho \hat{A}_\alpha^\dagger - \frac{1}{2}\{\hat{A}_\alpha^\dagger \hat{A}_\nu, \rho\}) \\
&+ \varepsilon^2 \sum_{\alpha,\nu=1}^{N} Q_{\alpha\nu}(\hat{A}_\nu^\dagger \rho \hat{A}_\alpha - \frac{1}{2}\{\hat{A}_\alpha \hat{A}_\nu^\dagger, \rho\}),
\end{aligned}
\tag{2.30}
$$

where

$$\hat{\mathcal{H}}_S^{eff} = \hat{\mathcal{H}}_S + \varepsilon^2 \sum_{\alpha,\nu=1}^{N} \left[f_{\nu\alpha}^{\Delta}(\omega_\alpha) + f_{\alpha\nu}^{\Delta}(\omega_\nu) \right] \hat{A}_\alpha^\dagger \hat{A}_\nu,$$

$$Q_{\alpha\nu} = F_{\alpha\nu}(\omega_\nu) + iF_{\alpha\nu}^{\Delta}(\omega_\nu) + (\alpha \leftrightarrow \nu)^*, \quad F_{\alpha\nu}^{\Delta}(\omega) = \mathcal{P} \int \frac{d\omega'}{\pi} \frac{F_{\alpha\nu}(\omega')}{\omega' - \omega},$$

$$v_{\alpha\nu} = f_{\alpha\nu}(\omega_\nu) + if_{\alpha\nu}^{\Delta}(\omega_\nu) \tag{2.31}$$

and $F_{\alpha\nu}(\omega)$, $f_{\alpha\nu}(\omega)$ and $f_{\alpha\nu}^{\Delta}(\omega)$ are as defined in Eqs. 2.21, 2.23. We note that Eq. 2.30 is exactly of the GKSL form Eq. 2.1. Let $\mathbf{Q}$ and $\mathbf{v}$ be matrices with the elements $\{Q_{\alpha\nu}\}$ and $\{v_{\alpha\nu}\}$ respectively. Then, by GKSL's theorem discussed in Sec. 2.1.1, for ρ to preserve complete positivity at all time, we need $\mathbf{Q} + \mathbf{v} + \mathbf{v}^\dagger \to$ positive semi-definite, $\mathbf{Q} \to$ positive semi-definite. However, as is known [21], these conditions are not always satisfied in a microscopic derivation. So it is important to ensure that this equation gives correct answers. We will check this for a simple model in the next chapter.

For non-interacting systems, a more useful equation than the QMEs is the evolution equation for the two-point equal time correlation functions

$$C_{\alpha\nu}(t) = Tr(\rho(t)\hat{A}_\alpha^\dagger \hat{A}_\nu). \tag{2.32}$$

This is directly obtained from the RQME Eq. 2.30 by multiplying by $\hat{A}_\alpha^\dagger \hat{A}_\nu$ and taking trace. These correlation functions form a Hermitian matrix which we will call the correlation matrix. This is also sometimes called single-particle density matrix. The evolution equation for these correlation functions form a complete set of N^2 linear differential equations,

$$\frac{dC_{\alpha\nu}}{dt} = i(\omega_\alpha - \omega_\nu)C_{\alpha\nu}(t) + \varepsilon^2 Q_{\alpha\nu} - \varepsilon^2 \sum_{\sigma=1}^{N} \left[v_{\alpha\sigma}C_{\sigma\nu}(t) + C_{\alpha\sigma}(t)v_{\nu\sigma}^* \right], \tag{2.33}$$

where $Q_{\alpha\nu}$ and $v_{\alpha\nu}$ are as defined in Eq. 2.31. We will have a lot to discuss on Eq. 2.33. But first, we will show that the exact same equation can also be derived via the QLE by doing Born-Markov approximation.

QLE

The derivation of the RQME is long and involved as given in Appendix. 6.2 and Sec. 2.1.2. However, Eq. 2.33 can be more directly derived starting from the QLE equation Eq. 2.17, written for weak system-bath coupling (Eq. 2.29),

$$\frac{d\hat{A}_\nu}{dt} = -i\omega_\nu \hat{A}_\nu(t) - i\varepsilon\hat{\xi}_\nu(t) - \varepsilon^2 \sum_{\ell}' \sum_{\sigma} \Phi_{\ell\nu}\Phi_{\ell\sigma} \int_0^t dt' \int \frac{d\omega}{2\pi} \mathfrak{I}_\ell(\omega)e^{-i\omega(t-t')}\hat{A}_\sigma(t'), \tag{2.34}$$

19

where $\mathfrak{J}_\ell(\omega)$ and $\hat{\xi}_\nu(t)$ are as defined in Eq. 2.12, 2.19. First, for Born approximation, we will neglect all terms higher than $O(\varepsilon^2)$. The last term in above equation is already $O(\varepsilon^2)$. Also, we note that $\hat{A}_\sigma(t') = \hat{A}_\sigma(t)e^{i\omega_\sigma(t-t')} + O(\varepsilon)$. Since, the last term is already $O(\varepsilon^2)$, we can neglect all higher order corrections to obtain

$$\varepsilon^2 \sum_\ell{}' \sum_\sigma \Phi_{\ell\nu} \Phi_{\ell\sigma} \int_0^t \int \frac{d\omega}{2\pi} \mathfrak{J}_\ell(\omega) e^{-i\omega(t-t')} \hat{A}_\sigma(t') dt'$$

$$\simeq \varepsilon^2 \sum_\ell{}' \sum_\sigma \Phi_{\ell\nu} \Phi_{\ell\sigma} \hat{A}_\sigma(t) \int_0^t dt' \int \frac{d\omega}{2\pi} \mathfrak{J}_\ell(\omega) e^{-i(\omega-\omega_\sigma)t'}. \qquad (2.35)$$

Now, we do the Markov approximation. Let τ_{B_1} be the time in which $\int \frac{d\omega}{2\pi} \mathfrak{J}_\ell(\omega) e^{-i\omega t'}$ for all sites attached to baths decay to $O(\varepsilon)$. Note that τ_{B_1} depends on the bath spectral functions but not on the temperatures and the chemical potentials of the baths. Specifically, it depends on the 'width' of $\mathfrak{J}_\ell(\omega)$, and hence the bandwidth of the bath. The larger the bandwidth, the smaller is τ_{B_1}. For Markov approximation, observation time $t \gg \tau_{B_1}$, so that we can extend the time integration to infinity. So, after Born-Markov approximation we have

$$\frac{d\hat{A}_\nu}{dt} \simeq -i\omega_\nu \hat{A}_\nu(t) - i\varepsilon\hat{\xi}_\nu(t) - \varepsilon^2 \sum_{\sigma=1}^N v_{\nu\sigma}^* \hat{A}_\sigma(t), \qquad (2.36)$$

with $v_{\nu\sigma}$ defined as in Eq. 2.31. Using this equation, for equal time two point correlation functions $C_{\alpha\nu}(t) = \langle \hat{A}_\alpha^\dagger(t) \hat{A}_\nu(t) \rangle$ we have,

$$\frac{dC_{\alpha\nu}}{dt} = \langle \frac{d\hat{A}_\alpha^\dagger}{dt} \hat{A}_\nu(t) \rangle + (\alpha \leftrightarrow \nu)^\dagger$$

$$= i(\omega_\alpha - \omega_\nu)C_{\alpha\nu}(t) + i\varepsilon \left[\langle \hat{\xi}_\alpha^\dagger(t) \hat{A}_\nu(t) \rangle - \langle \hat{A}_\alpha^\dagger(t) \hat{\xi}_\nu(t) \rangle \right] - \varepsilon^2 \sum_{\sigma=1}^N \left[v_{\alpha\sigma} C_{\sigma\nu}(t) + C_{\alpha\sigma}(t) v_{\nu\sigma}^* \right].$$

$$(2.37)$$

Now, we need to evaluate $\langle \hat{\xi}_\alpha^\dagger(t) \hat{A}_\nu(t) \rangle$ up to $O(\varepsilon)$. To do this, we write the formal solution of Eq. 2.36 up to $O(\varepsilon)$,

$$\hat{A}_\nu(t) = \hat{A}_\nu(0)e^{-i\omega_\nu t} - i\varepsilon \int_0^t dt' \hat{\xi}_\nu(t') e^{-i\omega_\nu(t-t')} + O(\varepsilon^2). \qquad (2.38)$$

We then note, $\langle \hat{\xi}_\alpha^\dagger(t) \hat{A}_\nu(0) \rangle = \langle \hat{\xi}_\alpha^\dagger(t) \rangle \langle \hat{A}_\nu(0) \rangle = 0$, because, initially the set-up was taken to be in the direct product state of the system and the baths. So multiplying above equation from the left with $\hat{\xi}_\alpha^\dagger(t)$ and taking expectation value, we have

$$\langle \hat{\xi}_\alpha^\dagger(t) \hat{A}_\nu(t) \rangle = -i\varepsilon \int_0^t dt' \langle \hat{\xi}_\alpha^\dagger(t) \hat{\xi}_\nu(t') \rangle e^{-i\omega_\nu(t-t')} + O(\varepsilon^2)$$

$$= -i\varepsilon \sum_\ell{}' \Phi_{\ell\alpha} \Phi_{\ell\nu} \int_0^t dt' \int \frac{d\omega}{2\pi} \mathfrak{J}_\ell(\omega) \mathfrak{n}_\ell(\omega) e^{i(\omega-\omega_\nu)t'} + O(\varepsilon^2). \qquad (2.39)$$

Now, again we do the Markov approximation. Let τ_{B_2} be the time in which $\int \frac{d\omega}{2\pi} \mathfrak{J}_\ell(\omega) \mathfrak{n}_\ell(\omega) e^{i\omega t'}$ for all sites attached to baths decay to $O(\varepsilon)$. Note that τ_{B_2}, unlike τ_{B_1}, depends on the bandwidths as well as on the temperatures and the chemical potentials of the baths. Then, for Markov approximation, observation time $t \gg \tau_{B_2}$, so that we can extend the time integration to infinity. So, with Born-Markov approximation we have

$$i\varepsilon \left[\langle \hat{\xi}_\alpha^\dagger(t) \hat{A}_\nu(t) \rangle - \langle \hat{A}_\alpha^\dagger(t) \hat{\xi}_\nu(t) \rangle \right] \simeq \varepsilon^2 \left[F_{\alpha\nu}(\omega_\nu) + i F_{\alpha\nu}^\Delta(\omega_\nu) + (\alpha \leftrightarrow \nu)^* \right] = \varepsilon^2 Q_{\alpha\nu}, \quad (2.40)$$

with $F_{\alpha\nu}(\omega)$ and $Q_{\alpha\nu}$ as defined in Eqs. 2.21 and 2.31 respectively. Putting this result in Eq. 2.37, we recover Eq. 2.33. Thus, we have shown that the RQME and the QLE methods are exactly equivalent under Born-Markov approximation. Further, we have gained crucial insight into what controls the Markov approximation. Clearly, for Markov approximation to be valid $t \gg \tau_B = max\{\tau_{B_1}, \tau_{B_2}\}$. τ_{B_1} is controlled by the bandwidths of the baths, and τ_{B_2} is controlled by the bandwidths, as well as, the temperatures and chemical potentials of the baths.

The Lyapunov equation and unique NESS

Having derived the evolution equation for the correlation matrix, Eq. 2.33 in two different ways, we now look at the equation in more detail. The most crucial observation is that Eq. 2.33 can be written in the form of a Lyapunov equation as follows

$$\frac{d\mathbf{C}}{dt} = -(\mathcal{G}\mathbf{C} + \mathbf{C}\mathcal{G}^\dagger) + \varepsilon^2 \mathbf{Q}, \quad (2.41)$$

$$\mathcal{G} = -i\mathbf{D} + \varepsilon^2 \mathbf{v}, \quad (2.42)$$

where $\mathbf{C}(t)$ is the NxN Hermitian matrix with elements $\{C_{\alpha\nu}(t)\}$, $\mathbf{Q}$ and $\mathbf{v}$ are as defined after Eq. 2.31, $\mathbf{D}$ is the diagonalized $\mathbf{H}^S$ defined in Eq. 2.13. Note that $\mathbf{Q}$ is Hermitian and $\mathbf{v}$ is non-Hermitian. $\mathbf{Q}$ depends on bath spectral functions and temperatures and chemical potentials of the baths, whereas, $\mathbf{v}$ depends only on the bath spectral functions, and is independent of temperatures and chemical potentials of the baths. This point will be important later, while discussing the 'AC case', where it will be more helpful to write Eq. 2.41 in a different but equivalent form

$$\frac{dC_{vec}}{dt} = -\mathbf{M}C_{vec} + \varepsilon^2 Q_{vec}, \quad \mathbf{M} = \mathbb{I}_N \otimes \mathcal{G} + \mathcal{G}^* \otimes \mathbb{I}_N, \quad (2.43)$$

$\mathbb{I}_N$ is the N dimensional identity matrix and $\otimes$ denotes Kronecker product, and C_{vec} (Q_{vec}) is a N^2 column matrix having all the elements of $\mathbf{C}$ ($\mathbf{Q}$). The Lyapunov equation

is a well-studied equation in mathematics and occurs widely in control theory. It is interesting that the equation for correlation matrix has the form of a Lyapunov equation. Apart from this, having the Lyapunov equation will also allow us to find conditions for a unique NESS. To see this we first note that solution to the Lyapunov equation Eq. 2.41 can be written as follows

$$\mathbf{C}(t) = e^{-\mathcal{G}t}\mathbf{C}(0)e^{-\mathcal{G}^\dagger t} + \varepsilon^2 \int_0^t dt' e^{-\mathcal{G}t'}\mathbf{Q}e^{-\mathcal{G}^\dagger t'}. \tag{2.44}$$

If real parts of eigenvalues of $\mathcal{G}$ are positive (this is called the stability condition for the Lyapunov equation), it is clear from Eq. 2.44 that the system approaches a unique NESS given by

$$\mathbf{C}(\infty) = \varepsilon^2 \int_0^\infty dt' e^{-\mathcal{G}t'}\mathbf{Q}e^{-\mathcal{G}^\dagger t'}, \tag{2.45}$$

which is the solution of the so called continuous time algebraic Lyapunov equation,

$$\mathcal{G}\mathbf{C}(\infty) + \mathbf{C}(\infty)\mathcal{G}^\dagger = \varepsilon^2\mathbf{Q}. \tag{2.46}$$

The sufficient condition for this is $\mathbf{v} + \mathbf{v}^\dagger$ being positive definite. The algebraic Lyapunov equation greatly simplifies the problem of finding $\mathbf{C}(\infty)$ numerically. It is complete set of N^2 linear equations. Usually, time taken to solve such a system of equations scales as N^6. However, for the algebraic Lyapunov equation, standard efficient algorithms (standard packages in Mathematica, python, Matlab etc.) are available for which the time taken to solve scales as N^3. In this thesis we will only consider the cases where a unique steady state exists.

Although the Lyapunov equation can be exactly solved, it is insightful to have perturbative solutions of the Lyapunov equation up to leading order in ε. From such solutions it can be shown that the gives proper thermalization in equilibrium. Applying the perturbative solution to a 1D nearest neighbour chain a simple expression for current can be obtained. These derivations are straightforward, but quite lengthy. So we will defer them to Appendix. 6.3 and Appendix. 6.4. Instead, in the next chapter, we will explicitly work out the case for the two-site system and compare with exact results.

Summary

Thus, we have developed the formalism for the most general non-interacting open quantum set-up, under Born-Markov approximation. We have shown the equivalence of RQME

and QLE in such set-ups. We have further shown that the evolution equation for correlation matrix has the form of a Lyapunov equation, which greatly simplifies the problem numerically.

2.3.2 AC case

[This subsection closely follows parts of discussions in the published paper (ii).]

We now extend the above formalism to the case where the temperatures and chemical potentials of the baths are periodic functions of time. For this, we again go back to the most general non-interacting open-quantum set-up defined by Eqs. 2.10, 2.11. We have previously seen above that in the Lyapunov equation Eq. 2.41, the inhomogeneous part $\mathbf{Q}$ depends on the temperatures and chemical potentials of the baths, while the matrix $\mathcal{G}$ in the homogeneous part is independent of them. This immediately suggests that if a periodic time-dependence of temperatures or chemical potentials can be built in such that correlation matrix still has the form of the Lyapunov equation, it will provide a tremendously simplified way to obtain results for such an AC driven case. Such a time dependence can be indeed built via the following physically motivated protocol.

Protocol for AC drive

In the following, χ is the full density matrix of system+bath, ρ_B is the density matrix of the bath, and ρ is density matrix of the system obtained by tracing χ over bath variables. Let us, for the time being, assume one bath. The protocol can readily be generalized to multiple baths.

The protocol for a single bath is as follows :

a) At time $t = 0$, $\chi = \rho \otimes \rho_B(0)$, with $\rho = \rho_0(0)$, which is some arbitrary initial system state, and $\rho_B(0) = exp[-\beta(0)(\hat{\mathcal{H}}_B - \mu(0)\hat{N}_B)]/Z(0)$. That is, the inital state is a product state of an arbitrary system state and a thermal bath state.

b) We evolve the system for a time τ_D. After time τ_D, the system reaches the state $\rho_0(\tau_D)$. Note that during this time, the temperatures and chemical potentials of the bath has not changed.

c) At $t = \tau_D$, we restart the entire system+bath setup with the initial state $\chi = \rho \otimes \rho_B(\tau_D)$, with $\rho = \rho_1(0) = \rho_0(\tau_D)$ and $\rho_B(\tau_D) = exp[-\beta(\tau_D)(\hat{\mathcal{H}}_B - \mu(\tau_D)\hat{N}_B)]/Z(\tau_D)$. That is, at time τ_D, the bath is changed into the thermal state with new inverse temperature and chemical potential $\beta(\tau_D), \mu(\tau_D)$, and the full system+bath state is again taken

as the product state. This step implicitly assumes weak-system bath coupling. This is because, under weak system-bath coupling, we can assume that the bath is hardly affected by the system, and to leading order in system-bath coupling, the full density matrix is in product form.

d) We again let the system density matrix evolve under this new bath for time τ_D starting from the new initial state. Again, after time τ_D, we restart the entire set-up with initial state $\chi = \rho(0) \otimes \rho_B(2\tau_D)$, with $\rho = \rho_2(0) = \rho_1(\tau_D)$ and $\rho_B(2\tau_D) = exp[-\beta(2\tau_D)(\hat{\mathcal{H}}_B - \mu(2\tau_D)\hat{N}_B)]/Z(2\tau_D)$. This protocol continues for a very long time and we will be mostly interested in the long time dynamics of this process.

In the limit of very small τ_D, the above protocol gives a nearly continuous evolution of temperatures and chemical potentials of the baths. In particular, if the temperature and chemical potential vary periodically with a period T, and $\tau_D \ll T$, then the above protocol describes dynamics of a system evolving under a continuous periodic drive from the temperature and chemical potential of the bath.

Till now, this protocol only assumed weak system-bath coupling, i.e, the Born approximation. To get to the Lyapunov equation form we also need the Markov assumption. Let τ_B be the characteristic time-scale of relaxation of the effects of system-bath coupling on the bath. Then, we assume that $\tau_B \ll \tau_D$. So, if τ_{expt} be experimentally the smallest time scale, most of our following discussion holds if the following condition on time-scales is maintained

$$\tau_B \ll \tau_D \ll \tau_{expt} \ll T. \tag{2.47}$$

This condition may be a bit restrictive, but when applicable allow for tremendous simplification easily capturing very non-trivial and interesting physics (as we will explicitly see in simple case in a later chapter). For multiple baths, the above protocol is followed for each bath. τ_B is then taken as the largest of the relaxation times of the baths, so that τ_D is much larger than relaxation time scales of all baths.

RQME for AC drive and periodic steady state

The above protocol, along with the condition (Eq. 2.47) on time scales, breaks down the ac drive process into steps of time independent processes where Born-Markov approximation and hence the Lyapunov equation Eq. 2.41 can be applied. For the ac case, it will be more helpful to use the form given in Eq. 2.43. Between the $(r-1)$th and the rth steps of the

protocol, the evolution equation for correlation matrix is as given by time-independent RQME

$$\frac{dC_{vec}((r-1)\tau_D)}{dt} = -\mathbf{M}C_{vec}((r-1)\tau_D) + \varepsilon^2 Q_{vec}((r-1)\tau_D). \tag{2.48}$$

The correlation matrix at time $r\tau_D$ is then given by the formal solution of this equation which can be written as

$$e^{\mathbf{M}\tau_D}C_{vec}(r\tau_D) = C_{vec}((r-1)\tau_D) + \varepsilon^2 \int_0^{\tau_D} dt' e^{\mathbf{M}t'} Q_{vec}((r-1)\tau_D + t'). \tag{2.49}$$

If τ_D is small, t' is also small. But $r\tau_D$ can still be large for $r \gg 1$. In such case, we can expand each term to the linear order in τ_D to obtain

$$(1 + \mathbf{M}\tau_D)C_{vec}(r\tau_D) = C_{vec}((r-1)\tau_D) + \varepsilon^2 Q_{vec}((r-1)\tau_D)\tau_D$$
$$\Rightarrow \frac{C_{vec}(r\tau_D) - C_{vec}((r-1)\tau_D)}{\tau_D} = -\mathbf{M}C_{vec}(r\tau_D) + \varepsilon^2 Q_{vec}((r-1)\tau_D). \tag{2.50}$$

$\tau_{expt} \gg \tau_D$ means we can take $\tau_D \to 0$, so that we have

$$\frac{dC_{vec}}{dt} = -\mathbf{M}C_{vec}(t) + \varepsilon^2 Q_{vec}(t). \tag{2.51}$$

Thus, as we wanted, we have only time dependence in the inhomogeneous part. Writing this equation absolutely explicitly, we have

$$\frac{dC_{\alpha\nu}}{dt} = i(\omega_\alpha - \omega_\nu)C_{\alpha\nu}(t) + \varepsilon^2 Q_{\alpha\nu}(t) - \varepsilon^2 \sum_{\sigma=1}^N \left[v_{\alpha\sigma}C_{\sigma\nu}(t) + C_{\alpha\sigma}(t)v_{\nu\sigma}^* \right], \tag{2.52}$$

$$Q_{\alpha\nu}(t) = [F_{\alpha\nu}(\omega_\nu, t) + iF_{\alpha\nu}^\Delta(\omega_\alpha, t) + (\alpha \leftrightarrow \nu)^*], \quad F_{\alpha\nu}(\omega, t) = \sum_{\ell=1}^N c_{\ell\alpha}^* c_{\ell\nu} \frac{\mathfrak{J}_\ell(\omega)\mathfrak{n}_\ell(\omega, t)}{2},$$

and $v_{\alpha\nu}$ are as defined previously in Eq. 2.31. Eq. 2.51 has the formal solution

$$C(t) = e^{-\mathbf{M}t}C(0) + \varepsilon^2 \int_0^t dt' e^{-\mathbf{M}(t-t')} Q(t'). \tag{2.53}$$

We wish to look at the long time properties of Eq. 2.53. Let our ac drive be periodic with a time period T. Then, for integer r,

$$Q(t + rT) = Q(t), \quad r \in \mathbb{Z}. \tag{2.54}$$

We break up the observation time t into steps of T, so that, for integer m,

$$t = mT + \tau \quad m \in \mathbb{Z}. \tag{2.55}$$

25

Then Eq. 2.53 can be written as

$$C(mT + \tau) = \varepsilon^2 \sum_{r=1}^{m} \left(e^{-\mathbf{M}rT} \right) \int_0^T dt' e^{-\mathbf{M}(\tau-t')} Q(t')$$

$$+ \varepsilon^2 \int_0^\tau dt' e^{-\mathbf{M}(\tau-t')} Q(t') + e^{-\mathbf{M}(mT+\tau)} C(0). \tag{2.56}$$

Now, assuming the real part of all the eigenvalues of $\mathbf{M}$ are positive, we can perform the sum in above equation. Also, we are interested in the long time limit, $m \gg 1$. Hence we have

$$C(mT + \tau) = \varepsilon^2 (e^{\mathbf{M}T} - \mathbb{I}_{N^2})^{-1} \int_0^T dt' e^{-\mathbf{M}(\tau-t')} Q(t') + \varepsilon^2 \int_0^\tau dt' e^{-\mathbf{M}(\tau-t')} Q(t'). \tag{2.57}$$

Note that, in the long time limit, the RHS is independent of m, and is also independent of the initial condition. This means that in the long time limit, the correlation functions settle down in a periodic state, with period same as the ac drive. This is consistent with Floquet theory. However, note that, Floquet theory was not used explicitly to derive this result.

Resonances and Currents

Now, let us go back to Eq. 2.52. Since in the long time limit the periods of $C(t)$ and $Q(t)$ are same, we can perform a Fourier series expansion :

$$C_{\alpha\nu}(t) = \sum_{p=-\infty}^{\infty} C_{\alpha\nu}^p e^{ip\Omega_0 t}, \ Q_{\alpha\nu}(t) = \sum_{p=-\infty}^{\infty} Q_{\alpha\nu}^p e^{ip\Omega_0 t} \tag{2.58}$$

where $\Omega_0 = \frac{2\pi}{T}$. Substituting in Eq. 2.52, we obtain the following equation for each Fourier mode,

$$i(\omega_\alpha - \omega_\nu - p\Omega_0) C_{\alpha\nu}^p + \varepsilon^2 Q_{\alpha\nu}^p - \varepsilon^2 \left[\sum_{\sigma=1}^{N} C_{\alpha\sigma}^p v_{\nu\sigma} + C_{\sigma\nu}^p v_{\alpha\sigma}^* \right] = 0. \tag{2.59}$$

This immediately gives us two important results. First, we note that for the time-average correlation functions, $\overline{C}_{\alpha\nu}(t) = \frac{1}{T} \int_t^{t+T} dt' C_{\alpha\nu}(t') = C_{\alpha\nu}^0$, and similarly for $Q_{\alpha\nu}$. With this we find that the equation averaged over one time period gives exactly the steady state equation for a dc bias given by the time-period averaged bose or fermi distribution functions $\overline{n_\ell(\omega, t)}$. Even when the time-period averaged temperature or chemical potential difference between the various baths may be zero, the difference between the time-period averaged bose or fermi distribution functions may not be zero. In such cases, we will get

26

a time-period averaged current even though there is no time period averaged bias. This is the phenomenon of charge or energy pumping.

Second, we see that when $\omega_\alpha - \omega_\nu = p\Omega_0$, Eq. 2.59 becomes independent of system-bath coupling ε^2. This is the phenomenon of resonance. At resonance, the leading term of system correlation functions do not depend on system bath coupling. So all system properties, like current between two sites inside the system, which were otherwise proportional to ε^2 in the leading term, become larger by orders of magnitude.

Even though system properties become large at resonance, the current from any of the baths still remain small. To see this, we need the expression for current from the baths in terms of the correlation functions. The expression for particle current is obtained from the continuity equation for conservation of particles

$$\frac{d}{dt}\Big(\sum_{\alpha=1}^{N} C_{\alpha\alpha}\Big) = \sum_{\ell} I_{B^{(\ell)} \to \ell}. \tag{2.60}$$

$I_{B^{(\ell)} \to \ell}$ is the particle current from bath attached to the ℓth site. Under dc bias, in steady state, the LHS of above equation is zero, and hence the currents from the baths are equal. However, under ac drive, even at long time, the LHS is not zero, and thus, instantaneous currents from the baths can be different. The summation on the right runs over all lattice sites connected to bath. The expressions for the currents from the baths obtained from above continuity equations and Eq. 2.52 are

$$I_{B^{(\ell)} \to \ell} = \varepsilon^2 \Big[\sum_{\alpha=1}^{N} Q_\alpha^{(\ell)}(t) - \sum_{\sigma,\alpha=1}^{N} C_{\alpha\sigma}(t)\big(v_{\alpha\sigma}^{(\ell)} + v_{\sigma\alpha}^{(\ell)*}\big) \Big] \tag{2.61}$$

where

$$Q_\alpha^{(\ell)}(t) = |\Phi_{\alpha\ell}|^2 \mathfrak{J}_\ell(\omega_\alpha) n_\ell(\omega_\alpha, t)$$
$$v_{\alpha\sigma}^{(\ell)} = \Phi_{\alpha\ell}^* \Phi_{\sigma\ell} \Big(\frac{\mathfrak{J}_\ell(\omega_\sigma)}{2} - i\mathcal{P} \int \frac{d\omega}{2\pi} \frac{\mathfrak{J}_\ell(\omega)}{\omega - \omega_\sigma} \Big). \tag{2.62}$$

These expressions show that the currents from the baths are explicitly proportional to ε^2. So even when the system correlation functions are independent of ε^2 in the leading order, the currents from the baths are still $O(\varepsilon^2)$. However, this is not true for particle current between two sites which reside *within* the system. The current between ℓth and $\ell + 1$th lattice sites of the system is given by

$$I_{\ell \to \ell+1} = 2\,Im\Big(H_{\ell\,\ell+1}^{(s)} \hat{a}_\ell^\dagger \hat{a}_{\ell+1}\Big). \tag{2.63}$$

This current is not explicitly proportional to ε^2. At resonance, it is independent of ε^2 in the leading order. Thus, at resonance, the current between two adjacent lattice points in the system can be much larger than the current from the baths. On the other hand, the time-period averaged current, which corresponds to steady state of a dc bias, is same inside the system as from the baths.

The difference in frequency between adjacent resonances, which is given by

$$\frac{\omega_\alpha - \omega_\nu}{p} - \frac{\omega_\alpha - \omega_\nu}{p+1} = \frac{\omega_\alpha - \omega_\nu}{p(p+1)} \sim \frac{1}{p^2} \tag{2.64}$$

decreases as $1/p^2$. Hence small driving frequencies are always close to resonance with one of the higher modes (large p) of the steady state oscillations. So, for small driving frequencies, there is not much difference between the resonance and off-resonance condition. The values of the correlation functions, however, may not be so large as the first resonance ($p = 1$). This is because, the weight of the driving signal at higher modes may decrease.

It is also interesting to note that none of the expressions for currents can be reduced to the form of difference between fermi (bose) distributions of the various baths. Therefore, even when all the baths are driven by the exactly same time dependent temperature or chemical potential (symmetric ac drive), so that there is no instantaneous temperature or chemical potential difference, there can be an instantaneous current, both between the system and the baths and inside the system. At resonance, the internal currents may have a large amplitude (compared to the system-bath currents). The time-period averaged current is, of course, zero in this case.

It is important to state that we have *not* made the adiabatic approximation $T \gg t_{steady}$, where t_{steady} is the time to reach steady state, which corresponds to the smallest real part of eigenvalues of the matrix M in Eq. 2.51. If adiabatic approximation were made, then the expressions for the correlation functions at any time would be given by the dc-bias steady state results with the fermi (bose) distributions given by the instantaneous temperatures and chemical potentials. In that case, the expressions for currents *would have* reduced to the form of difference between fermi (bose) distributions of the various baths, and *no instantaneous current* would have been seen in the symmetric ac drive case.

Summary

Thus, we have looked at the same general non-interacting set-up as defined by Eqs. 2.10, 2.11, but this time, the thermodynamic parameters (i.e, temperatures and chemical potentials)

of the baths are periodically modulated. We have described the time-evolution of thermo-dynamic parameters of the bath by breaking up it up into small discrete time-steps within which the thermodynamic parameters of the baths do not change. Under Born-Markov approximation, evolution of the system density matrix within each of those discrete time-steps is given by the RQME. Taking the discrete time-step to zero gives a Born-Markov QME for such AC drive, from which the equation of motion for correlation functions can be derived. In the equation of motion for the correlation functions, tremendous simpli-fication occurs because the explicit time-dependence occurs only in the inhomogeneous part. From this equation, the following physical results have been directly shown: (a) the long time state is periodic with the same period as the drive (Floquet steady state), (b) a resonance will occur when the drive frequency is a multiple of an energy level spacing of the system, (c) at resonance, the instantaneous current inside the system can become orders of magnitude larger than the currents from the baths, (d) even if there is no in-stantaneous voltage or temperature bias, there can still be large non-zero instantaneous currents, (e) the time-period averaged quantities are given by the DC bias equation, with the DC bias given by the time-period averaged Bose or Fermi distribution functions, (f) there can be charge and energy pumping. Note that, these results are valid in arbitrary dimensions and geometry, and hold for any non-zero number of sites attached to baths.

A point to note is that there exists exact (i.e without Born-Markov approximation) methods of treating this AC drive set-up [28, 29, 30, 31, 32, 33, 34, 35, 36]. However, the exact methods are generally quite difficult numerically. Often, a simplifying assumption of adiabatic modulation of bath parameters is made [37, 38, 39]. But, such adiabatic approximation would not capture many of the interesting physics which can be directly read off from the RQME approach. Thus, under Born-Markov approximation, which is often true in generic experimental set-ups, the RQME method leads to tremendous simplification of the problem, yet captures very interesting physics beyond the adiabatic approximation.

In the next chapter, we will apply the formalism developed in this chapter to small systems. Taking simple cases, we will explicitly check that the results obtained from RQME agree with exact results. Then we will also use the RQME to investigate a simple interacting system.

Chapter 3

Transport through small systems

In this chapter, we investigate small systems within the validity regime of Born-Markov approximation. In section 3.1, we apply the formalism developed in the previous section for non-interacting set-ups to systems consisting of two-sites, each connected to its own bath. We look at both DC and AC transport cases. We validate our theory by comparison with exact (i.e, without Born-Markov approximation) results and also discuss the interesting physics of such systems. Then, in section 3.2, we use the RQME formalism to investigate transport through a small interacting system, namely a non-linear oscillator.

3.1 Two-sites without interactions

[This section closely follows parts of discussions in the published papers (i), (ii).]

We consider the following specific two-site system coupled to baths which are one-dimensional chains:

$$\hat{\mathcal{H}}_S = \omega_0(\hat{a}_1^\dagger \hat{a}_1 + \hat{a}_2^\dagger \hat{a}_2) + g(\hat{a}_1^\dagger \hat{a}_2 + \hat{a}_2^\dagger \hat{a}_1), \ \hat{\mathcal{H}}_B = \hat{\mathcal{H}}_B^{(1)} + \hat{\mathcal{H}}_B^{(2)}, \ \hat{\mathcal{H}}_B^{(\ell)} = t_B(\sum_{s=1}^\infty \hat{b}_s^{\ell\dagger}\hat{b}_{s+1}^\ell + h.c.),$$

$$\hat{\mathcal{H}}_{SB} = \varepsilon\gamma_1(\hat{a}_1^\dagger \hat{b}_1^1 + \hat{a}_1 \hat{b}_1^{1\dagger}) + \varepsilon\gamma_2(\hat{a}_2^\dagger \hat{b}_1^2 + \hat{a}_2 \hat{b}_1^{2\dagger}), \tag{3.1}$$

where the operators are all fermionic or all bosonic and $\hat{b}_s^\ell$ is the annihilation operator of the sth bath site of the ℓth bath, $\hat{a}_1$ ($\hat{a}_2$) is annihilation operator of the first (second) site. The bosonic version of this set-up can be realized in optical cavities, circuit QED, cavity optomechanics etc [1, 2, 3]. while the fermionic version can be realized using quantum dots, molecular junctions etc [4, 5] (see Fig. 3.1).

The eigenmodes of the system are given by $\hat{A}_1 = (\hat{a}_1 - \hat{a}_2)/\sqrt{2}$, $\hat{A}_2 = (\hat{a}_1 + \hat{a}_2)/\sqrt{2}$ with eigenvalues $\omega_1 = \omega_0 - g$, $\omega_2 = \omega_0 + g$. We assume $\omega_0 \gg \varepsilon$, so that QME can be
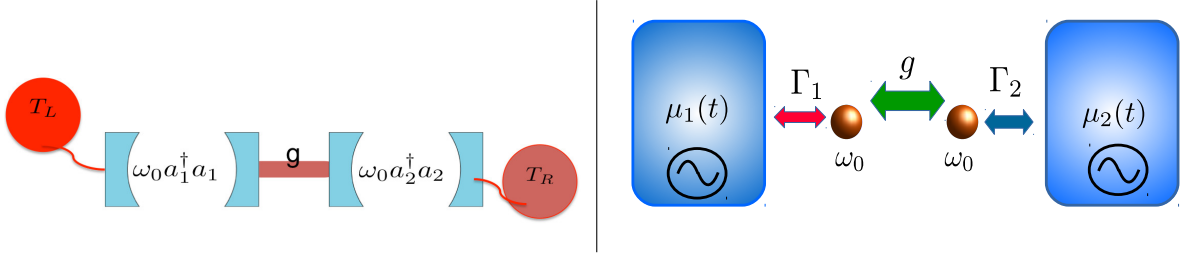
Figure 3.1: *Schematic diagram for the two-site set-up. The left corresponds to the bosonic case of two optical cavities connected to two baths at different temperatures. The right corresponds to the fermionic case of two non-interacting quantum dots connected to two baths at same temperature but with different chemical potentials. For AC case, the chemical potentials can be periodically modulated, as shown in the diagram. For DC case, they do not change with time.*

applied, while the parameter g can be varied freely. The bath spectral functions, defined in Eq. 2.12, can be obtained explicitly by going to eigenmodes of the baths. Note that since in our derivation of RQME, the system couples to the eigenmodes of the baths, $\kappa_{\ell r}$ are proportional to the eigenfunctions of the bath Hamiltonian. Because of infinite degrees of freedom, the energy spectrum of the bath can be considered continuous. For our case of the Hamiltonian in Eq. 3.1, bath eigen-energies are $\Omega(q_\ell) = -2t_B \cos q_\ell$ and $\kappa(q_\ell) = \gamma_\ell \sqrt{\frac{2}{\pi}} \sin q_\ell$, with $0 \le q_\ell \le \pi$. Thus,

$$\mathfrak{J}_\ell(\omega) = 4\gamma_\ell \int_0^\pi dq_\ell \sin^2 q_\ell \, \delta(\omega + 2t_B \cos q_\ell) = \Gamma_\ell \sqrt{1 - \frac{\omega^2}{4t_B^2}}, \quad \Gamma_\ell = \frac{2\gamma_\ell^2}{t_B}. \tag{3.2}$$

We also need to the following result $\mathcal{P} \int \frac{d\omega' \mathfrak{J}_\ell(\omega')}{2\pi(\omega'-\omega)} = -\frac{\gamma_\ell^2 \omega}{2t_B^2}$ to calculate $f_{\alpha\nu}^\Delta(\omega)$ [in Eq. 2.33]. $F_{\alpha\nu}^\Delta(\omega)$ cannot be written in a simple closed form and is calculated numerically. The functions $f_{\alpha\nu}(\omega), F_{\alpha\nu}(\omega)$ can be written down in matrix form as :

$$\mathbf{f}(\omega) = \frac{1}{4} \begin{bmatrix} \mathfrak{J}_1(\omega) + \mathfrak{J}_2(\omega) & \mathfrak{J}_1(\omega) - \mathfrak{J}_2(\omega) \\ \mathfrak{J}_1(\omega) - \mathfrak{J}_2(\omega) & \mathfrak{J}_1(\omega) + \mathfrak{J}_2(\omega) \end{bmatrix} \tag{3.3}$$

$$\mathbf{F}(\omega) = \frac{1}{4} \begin{bmatrix} \mathfrak{J}_1(\omega)\mathfrak{n}_1(\omega) + \mathfrak{J}_2(\omega)\mathfrak{n}_2(\omega) & \mathfrak{J}_1(\omega)\mathfrak{n}_1(\omega) - \mathfrak{J}_2(\omega)\mathfrak{n}_2(\omega) \\ \mathfrak{J}_1(\omega)\mathfrak{n}_1(\omega) - \mathfrak{J}_2(\omega)\mathfrak{n}_2(\omega) & \mathfrak{J}_1(\omega)\mathfrak{n}_1(\omega) + \mathfrak{J}_2(\omega)\mathfrak{n}_2(\omega) \end{bmatrix}. \tag{3.4}$$

We look at both DC and AC transports in this set-up.

3.1.1 DC case

We first look at the DC case. The goal is to check the Born-Markov approximated results of the previous chapter against exact calculations, which is possible for such simple

two-site systems. We will also compare the results with those obtained from two other commonly used phenomenological Lindblad QMEs for the set-up. We will do the comparisons by directly computing some physical observables from all the different formalisms. The observables we will be looking at are NESS current I, site occupations $\langle \hat{a}_\ell^\dagger \hat{a}_\ell \rangle$ and the mode occupations $N_\alpha = \langle \hat{A}_\alpha^\dagger \hat{A}_\alpha \rangle$.

Exact results : steady state via QLE

The NESS current and occupation obtained via exact QLE are given by

$$I = g^2 \varepsilon^2 \int \frac{d\omega}{2\pi} \frac{\mathfrak{J}_1(\omega)\mathfrak{J}_2(\omega)\big[\mathfrak{n}_1(\omega) - \mathfrak{n}_2(\omega)\big]}{|\mathcal{M}(\omega)|^2} \ , \tag{3.5}$$

$$\langle \hat{a}_1^\dagger \hat{a}_1 \rangle = \varepsilon \int \frac{d\omega}{2\pi} \Big[\frac{\mathcal{K}(\omega)\mathfrak{J}_1(\omega)\mathfrak{n}_1(\omega)}{|\mathcal{M}(\omega)|^2} + \frac{g^2 \mathfrak{J}_2(\omega)\mathfrak{n}_2(\omega)}{|\mathcal{M}(\omega)|^2} \Big] \ , \tag{3.6}$$

where

$$\mathfrak{J}_\ell^\Delta(\omega) = \mathcal{P} \int \frac{d\omega'}{2\pi} \frac{\mathfrak{J}_\ell(\omega')}{\omega' - \omega} \ ,$$

$$\mathcal{M}(\omega) = \Big[\big(\omega_0 - \omega - i\varepsilon^2 \frac{\mathfrak{J}_1(\omega)}{2} - \varepsilon^2 \mathfrak{J}_1^\Delta(\omega)\big)\big(\omega_0 - \omega - i\varepsilon^2 \frac{\mathfrak{J}_2(\omega)}{2} - \varepsilon^2 \mathfrak{J}_2^\Delta(\omega)\big) - g^2 \Big] \ ,$$

$$\mathcal{K}(\omega) = \Big| \omega_0 - \omega - i\varepsilon^2 \frac{\mathfrak{J}_2(\omega)}{2} - \varepsilon^2 \mathfrak{J}_2^\Delta(\omega) \Big|^2 \ . \tag{3.7}$$

The occupation of the second site is just $< a_2^\dagger a_2 > = 1 \leftrightarrow 2$ in Eq. (3.6). All integrals over ω go over all possible values of ω. Note that Eq. (3.5),(3.6) are exact results without any approximation. However, they are not closed form results and involve some complicated integrals. As mentioned in previous chapter, obtaining exact transient behaviour by this method is difficult. But transient behaviour for such small non-interacting systems can be easily obtained by exact numerics.

Exact results : time dynamics via system+bath numerics

To check the time dynamics we do numerical simulations. For this purpose, we choose a bath of finite size and evolve the full system+bath Hamiltonian $\hat{\mathcal{H}}$ using unitary Hamiltonian dynamics. Let us collectively denote by "d" a column vector with all annihilation operators of both system and baths. The full Hamiltonian can be written as $\hat{\hat{\mathcal{H}}} = \sum_{i,j} H_{ij} d_i^\dagger d_j$ where i now refers to either system or bath sites. If $D = \langle dd^\dagger \rangle$ denotes the full correlation matrix of system and baths, its time evolution is given by $D(t) = e^{iHt} D e^{-iHt}$. In our simulations we considered the system described by Eq. (3.1)

of two sites connected to baths each with 511 sites which are large enough to show negligible finite size effects.

Sysmmetric coupling to baths : $\gamma_1 = \gamma_2$: Full solution :

In Eq. 2.33, this corresponds to the special case of all system bath couplings being equal, i.e, when, $J_\ell(\omega) = J(\omega)$. Under this condition Eq. 2.33 can be solved exactly using the fact that $f_{\nu\sigma}(\omega) = [J(\omega)/2] \sum_{r=1}^{N} c_{\ell\nu}^* c_{\ell\sigma} = [J(\omega)/2]\delta_{\nu\sigma}$ due to orthonormality of the eigenfunctions. Thus, $v_{\nu\sigma} = 0 \ \forall \ \nu \neq \sigma$. Then Eq. 2.33 admits the exact solution :

$$C_{\alpha\nu}(t) = C_{\alpha\nu}(0)e^{-w_{\alpha\nu}t} + \varepsilon^2 \frac{Q_{\alpha\nu}}{w_{\alpha\nu}}(1 - e^{-w_{\alpha\nu}t}) \tag{3.8}$$

where $w_{\alpha\nu} = -i\omega_\alpha + \varepsilon^2(-if_{\alpha\alpha}^\Delta(\omega_\alpha) + f_{\alpha\alpha}(\omega_\alpha)) + (\alpha \rightarrow \nu)^*$. Note that the baths can still be at different temperatures and chemical potentials. So in this case, we have full time-dependent analytical closed form results for out of equilibrium correlation functions that hold for all values of g.

Asymmetric couplings to baths : $\gamma_1 \neq \gamma_2$, $g \gg \frac{\varepsilon^2}{t_B}$:

For asymmetric couplings, we do not have the above simplification any more. But we can obtain perturbative results up to leading order in ε assuming $g \gg \frac{\varepsilon^2}{t_B}$,

$$N_\alpha(t) \simeq N_\alpha(0)e^{-2\varepsilon^2 f_{\alpha\alpha}(\omega_\alpha)t} + \frac{F_{\alpha\alpha}(\omega_\alpha)}{f_{\alpha\alpha}(\omega_\alpha)}(1 - e^{-2\varepsilon^2 f_{\alpha\alpha}(\omega_\alpha)t}) \tag{3.9a}$$

$$C_{12}(t) \simeq C_{12}(0)e^{-w_{12}t} + \frac{i\varepsilon^2}{g}\Big[(F_{12}(\omega_2) - iF_{12}^\Delta(\omega_2))(1 - e^{-w_{12}t}) + v_{21}(N_1(0)e^{-w_{12}t} - N_1(t))$$

$$+ (1 \leftrightarrow 2)^*\Big] \tag{3.9b}$$

where $N_\alpha(t) = C_{\alpha\alpha}(t)$, and $w_{12} = -i\omega_1 + \varepsilon^2(-if_{11}^\Delta(\omega_1) + f_{11}(\omega_1)) + (1 \rightarrow 2)^*$.

The steady state values of mode occupation N_α^{ss} and current between 1st and 2nd site $I_{1\rightarrow2} = -g\,i\langle\hat{a}_1^\dagger\hat{a}_2 - \hat{a}_2^\dagger\hat{a}_1\rangle = g\,i\langle\hat{A}_1^\dagger\hat{A}_2 - \hat{A}_2^\dagger\hat{A}_1\rangle = 2g\,Im(C_{12})$:

$$N_\alpha^{ss} \simeq \frac{\mathfrak{J}_1(\omega_\alpha)\mathfrak{n}_1(\omega_\alpha) + \mathfrak{J}_2(\omega_\alpha)\mathfrak{n}_2(\omega_\alpha)}{\mathfrak{J}_1(\omega_\alpha) + \mathfrak{J}_2(\omega_\alpha)}, \tag{3.10a}$$

$$I_{1\rightarrow2} \simeq \frac{\varepsilon^2}{2}\sum_{\alpha=1}^{2}\frac{\mathfrak{J}_1(\omega_\alpha)\mathfrak{J}_2(\omega_\alpha)\big[\mathfrak{n}_1(\omega_\alpha) - \mathfrak{n}_2(\omega_\alpha)\big]}{\mathfrak{J}_1(\omega_\alpha) + \mathfrak{J}_2(\omega_\alpha)}. \tag{3.10b}$$

As mentioned in previous chapter, in equilibrium $\mathfrak{n}_1(\omega) = \mathfrak{n}_2(\omega) = \mathfrak{n}(\omega)$, $N_\alpha = \mathfrak{n}(\omega)$ and current is zero, which are the expected thermal values. Thus RQME shows proper thermalization and approach to steady state. This is also true in the more general cases than the two-site system, as shown in Appendix. 6.3.

Reduction to Lindblad form

The RQME is not in the Lindblad form. But it can be reduced to the Lindblad form by making certain further approximations. There are two popular forms of the Lindblad equations using either the local operators a_ℓ or the eigenbasis operators A_ν. We briefly discuss how they are obtained from the RQME and their expected regimes of validity.

Local Lindblad QME (LLQME) ($g < \varepsilon$) The local Lindblad equation for this system has the form $\partial \rho / \partial t = i[\rho, \hat{\mathcal{H}}_S] + \varepsilon^2 \left(\mathcal{L}_1^{LL} \rho + \mathcal{L}_2^{LL} \rho \right)$ where

$$\mathcal{L}_\ell^{LL} \rho = \mathfrak{J}(\omega_0) e^{\beta_\ell(\omega_0 - \mu_\ell)} \mathfrak{n}(\omega_0)(\hat{a}_\ell \rho \hat{a}_\ell^\dagger - \frac{1}{2}\{\hat{a}_\ell^\dagger \hat{a}_\ell, \rho\}) + \mathfrak{J}(\omega_0)\mathfrak{n}(\omega_0)(\hat{a}_\ell^\dagger \rho \hat{a}_\ell - \frac{1}{2}\{\hat{a}_\ell \hat{a}_\ell^\dagger, \rho\}).$$
$$(3.11)$$

For $g < \varepsilon$, RQME Eq. 2.30 can be reduced to LLQME by expanding the non-unitary dissipative part about $g = 0$ and keeping the first term. This is because, the dissipative part is already $O(\varepsilon^2)$, and since $g < \varepsilon$, higher order terms in g will give higher order terms in ε, which we neglect in RQME treatment. This amounts to putting $\omega_\nu = \omega_0$ in the dissipative part of Eq. 2.30. The same result is more conventionally obtained by considering the inter-site hopping term in the system Hamiltonian to be small and treating it as a part of the system-bath Hamiltonian while deriving the QME. This directly leads to the LLQME. Thus LLQME is valid when $g < \varepsilon$. LLQME results for current and occupation for this problem have been derived in various papers [40, 41]. The equilibrium condition $N_\alpha = n(\omega)$ is not obtained from LLQME, since for $g < \varepsilon$, each site interacts with its bath more strongly than with the other site, thereby thermalizing with its own bath. It clearly follows that if there was only one site, it would show thermalization. Thus the regime of validity of LLQME is too restrictive to show thermalization for a system with more than one non-interacting degrees of freedom.

Eigenbasis Lindblad QME (ELQME) ($g \gg \frac{\varepsilon^2}{t_B}, C_{12}^{ss} = 0$) The eigenbasis Lindblad equation for this system has the form $\frac{\partial \rho}{\partial t} = i[\rho, \hat{\mathcal{H}}_S] + \varepsilon^2 \left(\mathcal{L}_1^{EL} \rho + \mathcal{L}_2^{EL} \rho \right)$ where

$$\mathcal{L}_\alpha^{EL} \rho = (f_{\alpha\alpha}(\omega_\alpha) \mp F_{\alpha\alpha}(\omega_\alpha))(2\hat{A}_\alpha \rho \hat{A}_\alpha^\dagger - \{\hat{A}_\alpha^\dagger \hat{A}_\alpha, \rho\}) + F_{\alpha\alpha}(\omega_\alpha)(2\hat{A}_\alpha^\dagger \rho \hat{A}_\alpha - \{\hat{A}_\alpha \hat{A}_\alpha^\dagger, \rho\}).$$
$$(3.12)$$

Eq. 2.30 is reduced to ELQME under rotating wave / secular approximation [21, 42], which amounts to neglecting $\alpha \neq \nu$ terms in the sum in Eq. 2.30. The rotating wave approximation assumes that the observation time $t \gg \frac{1}{g}$. On the other hand, to give the

correct steady state, the QME must be valid for times shorter that time taken to reach steady state. This means that we need the QME to be valid at times $t \lesssim \frac{t_B}{\varepsilon^2}$, since we have already seen that the time taken to reach steady state $\sim \frac{t_B}{\varepsilon^2}$. The two conditions are valid together if $g \gg \frac{\varepsilon^2}{t_B}$. This seems like a rather weak condition.

However we note that, while these are the necessary conditions for obtaining ELQME, there is no guarantee that the resulting ELQME reproduces all physical observables accurately. In particular, neglecting $\alpha \neq \nu$ terms in the sum in Eq. 7 means ELQME has no terms connecting $\hat{A}_1$, $\hat{A}_2$. Therefore it gives $C_{12}^{ss} = 0$, where C_{12}^{ss} is the steady state value of C_{12}. This condition is of course valid only in equilibrium, where there is no current. Thus though rotating wave / secular approximation is a good approximation for equilibrium properties, it is a bad approximation in non-equilibrium. This point has also been succinctly discussed in Ref. [43].

However, ELQME still can be used to correctly obtain some non-eqilibrium results. For example, for $g \gg \frac{\varepsilon^2}{t_B}$ ELQME gives the same equation for N_α as Eq. 3.9a, 3.10a. This result then can be used to obtain the correct current between the left bath and the system [44, 45]. Thus ELQME suffers from a drawback that one is only able to compute the net current flowing between the two reservoirs in the NESS but not the current distributions in the system (e.g current flowing along two arms in a ring geometry). This also indicates a physical inconsistency of the ELQME formalism in non-equilibrium (see Appendix. 6.5).

Comparison of results from various methods and discussions

Finally we now present a detailed comparison of results obtained using the various approaches, for both steady state and time-dependent properties. For the two site problem we consider the bosonic and fermionic versions and compute quantities such as the occupation number and particle current from site 1 to site 2. We again summarize the various approaches that we use:

(a) For steady state properties, these are exactly computed using Eqs. 3.5,3.6 following from the QLE approach.

(b) Exact time dependent properties are obtained from the numerical approach discussed in Sec. (3.1.1).

(c) The Lyapunov equation, Eqs. 2.41, is solved to obtain the predictions of RQME. We also evaluate the perturbative solution of these equations given in Eqs. 3.9a,3.9b.

(d) One can also write the equations for two-point correlations obtained from the
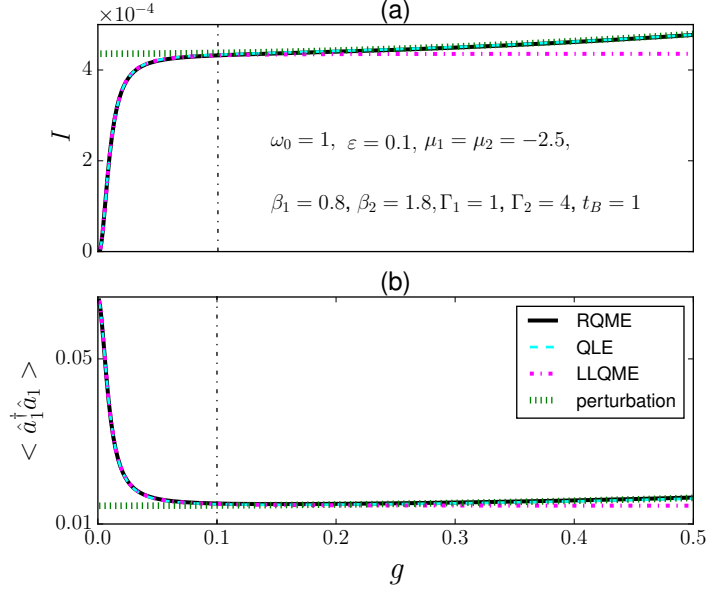
Figure 3.2: *Bosonic model-steady state properties: the figure shows (a) particle current, (b) the occupation number in the left site, as a function of inter-site hopping g for the 2 site boson problem. RQME shows near perfect agreement with exact results from QLE for all values of g, while LLQME and perturbation results [Eqs. 3.10a,3.10b] are valid in their respective limits. The vertical line marks the position of $g = \varepsilon$, below which LLQME is valid. The parameter $\Gamma_{1,2} = 2\gamma_{1,2}^2/t_B$ is related to the system-bath couping [see Eq. 3.2]. Current is measured in units of ω_0 and all energy variables are measured in units of $\hbar\omega_0$.*

Lindblad approach, and these are solved to obtain the predictions from LLQME.

(e) The ELQME approach cannot directly give the current inside the system. The predictions for the occupation number are the same as those from the perturbative solution of Eq. 3.9a.

We emphasize that all the approaches that we discuss are based on the same starting microscopic model of system and baths, given by Eqs. 3.1, which lead to the bath spectral function Eq. 3.2.

For the bosonic case, the steady state results for current and occupation number are shown in Fig. (3.2), and results from time-dynamics in Fig. (3.3,3.4). For the time dynamics, for the results presented here, the initial condition corresponds to no particles inside the system and baths in equilibrium at different μ and T. But we have tested with other initial conditions like a finite number of particles in the system and random initial values of the correlation functions. An estimate of bath relaxation time τ_B is important to ensure time-dynamics is in the validity regime of Born-Markov approximation. For our
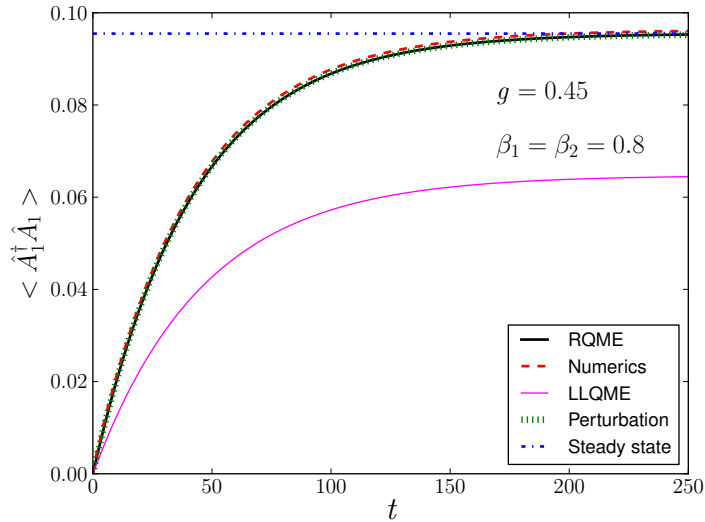
Figure 3.3: *Bosonic model - thermalization: we show the time evolution of occupation of the lower energy mode $\hat{A}_1$, corresponding to energy $\omega_1 = \omega_0 - g$, in equilibrium for the 2 site boson problem, starting from an empty system, for $g = 0.45$. The steady state (horizontal line) corresponds to the value of bose distribution $n(\omega_1) = [e^{\beta(\omega_1 - \mu)} - 1]^{-1}$ with the equilibrium bath temperatures and chemical potentials. LLQME does not show thermalization because it is not valid for $g > \varepsilon$, while exact numerical results, RQME results and the perturbation result [Eqs. 3.9a] match and show thermalization. All parameters not explicitly specified are same as Fig. (3.2). Current is measured in units of ω_0 and all energy variables are measured in units of $\hbar\omega_0$. Time is measured in units of ω_0^{-1}.*

parameters, $\tau_B \sim 7$ in units of ω_0^{-1} (see Appendix. 6.6). Our following observations are true for such generic initial conditions for the system. For the fermionic case, the results for the steady state current as a function of voltage difference and of the intra-system coupling g, are shown in Fig. (3.5). In all cases, the system-bath coupling is chosen to be asymmetric, i.e, $\gamma_1 \neq \gamma_2$.

Our most important observation is that RQME results obtained from the solution of Eq. 2.41 agree very well with exact results from QLE and numerics, for all values of g for steady state, as well as for long time dynamics. The LLQME agrees well for $g < \varepsilon$ as expected. In Fig. (3.3), we show that the system indeed thermalizes in equilibrium, and this is perfectly captured by RQME, and not by LLQME since it is invalid for $g > \varepsilon$. For $g \gg \frac{\varepsilon^2}{t_B}$, our analytical closed form perturbation results match quite well with the exact results, showing correct approach to steady state and thermalization. Therefore,
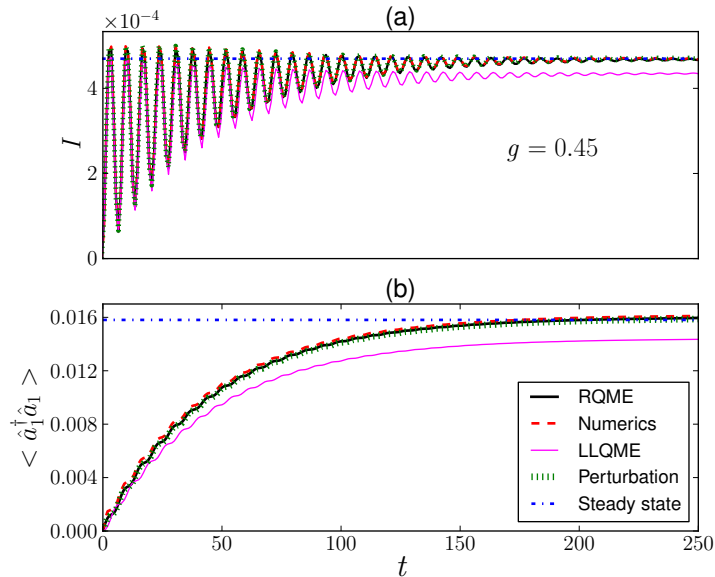
Figure 3.4: *Bosonic model - non-equilibrium time dynamics: we show the time evolution of (a) particle current (b) occupation number of left site for the 2 site boson problem, starting from an empty system, for $g = 0.45$. RQME results show good agreement with exact numerics. Since $g > \varepsilon$, LLQME does not match, while the perturbation result [Eqs. (3.9a,3.9b)] matches with the RQME. The horizontal line shows the exact steady state result obtained from QLE. All parameters not explicitly specified are same as Fig. (3.2). Current is measured in units of ω_0 and all energy variables are measured in units of $\hbar\omega_0$. Time is measured in units of ω_0^{-1}.*

we conclude that RQME gives the correct physics under Born-Markov approximation.

Apart from validating the RQME description, we also observe interesting physical trends. The boson problem may be realised in bosonic cold atom experiments or in optical cavity experiments with suitable choice of parameters and spectral functions. We see in Fig. 3.2 that steady state properties have markedly different behaviour depending on whether $g < \varepsilon$ or $g > \varepsilon$. For $g < \varepsilon$, the current increases rapidly, but after that there is a slow increase in current. Also, for $g < \varepsilon$ the occupation of the left cavity becomes minimum when $g \simeq \varepsilon$. However, beyond this point, the occupation of the left cavity increases slowly with increase in tunnelling probability g. These trends may be experimentally observed. However, these trends depend on the choice of the bath spectral function $\mathfrak{J}_\ell(\omega)$. For example, for optical cavity experiments, the commonly used Ohmic dissipation $\mathfrak{J}_\ell(\omega) \propto \omega$ will give slow decrease of current with g for $g > \varepsilon$, still showing a markedly different behaviour from $g < \varepsilon$ case. Here we microscopically derived $\mathfrak{J}_\ell(\omega)$
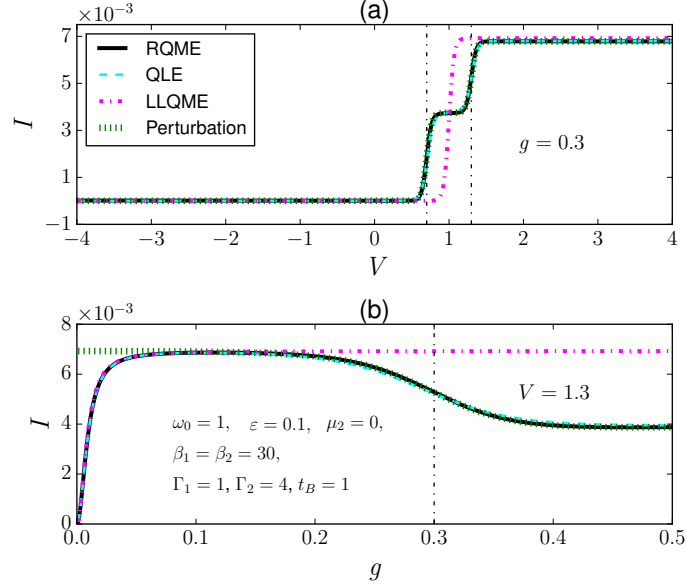
Figure 3.5: *Fermionic model - steady state properties: the plot shows (a) particle current vs voltage (b) particle current vs inter-site hopping in the 2 site fermion problem. The vertical lines correspond to positions where potential difference $V = \mu_1 - \mu_2 = \omega_\alpha$, where ω_α are the system energy levels. RQME shows near perfect agreement with exact results from QLE for all values of g, while LLQME and perturbation results [Eqs. 3.10a,3.10b] are valid in their respective limits. The graphs demonstrate the effect of conductance quantisation at low temperatures. The parameter $\Gamma_{1,2} = 2\gamma_{1,2}^2/t_B$. Current is measured in units of ω_0 and all energy variables are measured in units of $\hbar\omega_0$.*

assuming a microscopic model of the bath.

The fermionic system of two-sites may be experimentally realized in non-interacting quantum dots or in fermionic cold atom experiments. The current versus voltage plot of the fermionic system shows effect of conductance quantization. The current versus hopping g plot shows suppression of current after a value of g. These observations can be explained as follows. The two site system has two eigen-energy levels of energy $\omega_0 - g$ and $\omega_0 + g$ respectively. In Fig. 3.5, the right bath is held at zero chemical potential while the chemical potential of the left bath, μ_1, is varied. When $\mu_1 \ll \omega_0 - g$, no fermion from the left bath has the energy to enter the system. So there is no flow of current. When $\omega_0 - g \ll \mu_1 \ll \omega_0 + g$, the fermions can hop through the system via the lower energy level. So a finite current flows through the system. When $\mu_1 \gg \omega_0 + g$, fermion transport through system can occur through both energy levels. Since all system levels are now participating in transport, increasing μ_1 beyond this point does not affect current any

more. For similar reason, suppression of current occurs when $g \gg \mu_1 - \omega_0$ in current versus g plot. These observations can be easily obtained for larger systems also.

Summary

Thus, we have used the DC bias case of the set-up to investigate the validity of the various QME approaches. To test the validity of the RQME, we have compared results from RQME against (a) exact NESS results obtained by QLE, (b) exact time dynamics obtained by direct simulation of the set-up of the full system+bath Hamiltonian considering finite but large baths. We also compare the results with those obtained from two other commonly used phenomenological Lindblad QMEs for the set-up [40, 41, 44, 45]. We have found that, the RQME describes the set-up perfectly as long as system-bath coupling is weak (Born approximation) and the bath energy scales are much larger than system energy scales (Markov approximation). The phenomenologically written Lindblad QMEs have more much limited regimes of validity. This is true for both steady state and transient dynamics, and for both the fermionic and bosonic versions of the set-up [VI. (i)].

3.1.2 AC case

Now, to validate our theory of AC drive, as well as to better understand the physics of such ac drive, we apply this theory to the fermionic version of the set-up described in Eq. 3.1. This generic model can be used to describe physical systems such as driven double quantum dots[4] or single-molecule junctions with two molecular moieties (e.g. biphenyl-dithiol molecular junctions [5]). We will now take the two baths at the same temperature. Inverse temperature β is taken to be constant and the ac drive is given by periodic chemical potential :

$$\mathfrak{n}_\ell(\omega, t) = [e^{\beta(\omega - \mu_\ell(t))} + 1]^{-1}, \ \ \mu_\ell(t + rT) = \mu_\ell(t) \, \forall r \in \mathbb{Z}. \tag{3.13}$$

We choose the drive frequency as

$$\Omega_0 = \frac{\omega_2 - \omega_1}{p} = \frac{2g}{p}. \tag{3.14}$$

If p is integer, the system is at one of the resonances. If p is not an integer, it is away from resonance.

We look at the particle current in the ac driven steady state. The expressions for the currents are given in Eq. 2.60, 2.63. For the $N = 2$ case, the expression for $I_{1\to2}$ simplifies to $I_{1\to2} = 2g \, Im(C_{12})$. Two different ac drives are considered:
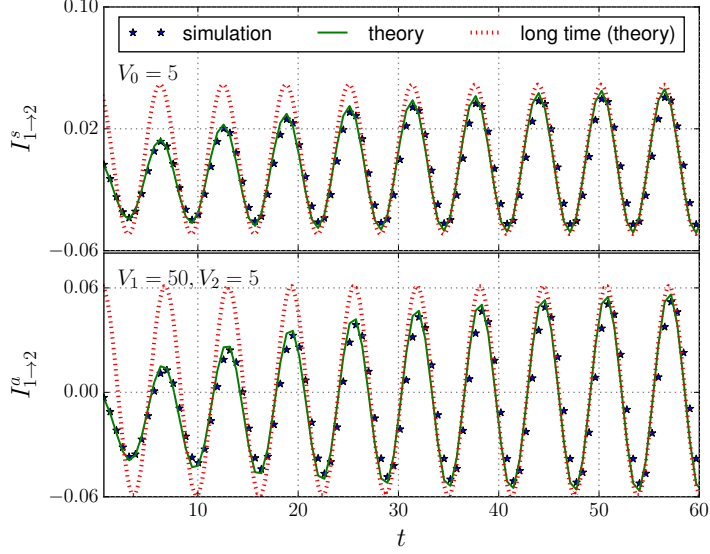
Figure 3.6: *Internal current $I_{1 \to 2}$ as a function of time, for the two cases (i) for symmetric ac drive: $\mu_1(t) = \mu_2 = V_0 \cos(\Omega_0 t)$ (top panel), (ii) for asymmetric ac drive :$\mu_1(t) = V_1 \cos(\Omega_0 t)$, $\mu_2 = V_2 \sin(\Omega_0 t)$ (bottom panel). The figure compares numerically exact simulation results for current inside the system (stars) with those obtained from our theory Eq. 2.53 for all times (solid line), and Eq. 2.57 for long times (dashed line). The near perfect agreement validates our theory. Other parameters $\Omega_0 = 2g, g = 0.5, t_B = 200, \omega_0 = 1, \beta_1 = \beta_2 = 0.1, \Gamma_1 = 1, \Gamma_2 = 9, \varepsilon = 0.1$. For these parameters, $\tau_B \sim 0.1$ (see Appendix. 6.6). For numerical simulation, $\tau_D = 0.2\pi$. All times are measured in units of ω_0^{-1}, all energies are measured in units of ω_0.*

(i) symmetric ac drive or zero voltage drive :

$$\mu_1(t) = \mu_2(t) = V_0 \sin(\Omega_0 t). \tag{3.15}$$

(ii) asymmetric ac drive :

$$\mu_1(t) = V_1 \cos(\Omega_0 t), \ \ \mu_2(t) = V_2 \sin(\Omega_0 t). \tag{3.16}$$

Comparison between analytic formula and exact numerics

Before proceeding to elucidate the physics dominating the driven system, we wish to validate the analytic derivation. For this we compare results obtained from Eq. 2.53 with that obtained from full numerical simulation of our protocol. For small systems like the two-site case considered here, the protocol for our ac drive set-up can be simulated exactly with finite but large baths. For each time-independent step of our protocol, we choose a

bath of finite size with bath correlations satisfying fermi distributions and evolve the full system+bath Hamiltonian $\hat{\mathcal{H}}$ using unitary Hamiltonian dynamics. Let us collectively denote by "d" a column vector with all annihilation operators of both system and baths. The full Hamiltonian can be written as $\hat{\mathcal{H}} = \sum_{i,j} H_{ij} d_i^\dagger d_j$ where i now refers to either system or bath sites. If $D = \langle dd^\dagger \rangle$ denotes the full correlation matrix of system and baths, its time evolution is given by $D(t) = e^{iHt} D e^{-iHt}$. The bath correlations are then changed according to the protocol, and the process is repeated. Various observables like current inside the system calculated using this exact numerical simulation can be compared with that obtained from Eq. 2.53, thus providing a way to validate our theory. Note that the numerical simulation does not take into consideration the 'Markov' condition on time scales given in Eq. 2.47. It holds even when Eq. 2.47 is not respected. Thus it allows us to check the validity of the crucial assumption on time scales required for our analytical treatment.

Fig. 3.6 shows the results for current inside the system $I_{1\rightarrow2}^s$ and $I_{1\rightarrow2}^a$ for cases (i) Eq. 3.15 and (ii) Eq. 3.16 respectively (superscripts in I stand for symmetric and asymmetric currents), as obtained from exact numerics as well as from our theory. Eq. 2.57 has been used to obtain the long time result, while Eq. 2.53 has been used to get the result at all times, showing approach to the long time dynamics. Numerical simulation has been done with baths of size 256 sites, which are large enough to have negligible finite-size effects. The near perfect agreement with exact numerical simulations validate our theory. For this plot, the drive frequency is chosen to be $\Omega_0 = \omega_1 - \omega_2 = 2g$, so that the set-up is at the first resonance. The near perfect match occurs for other frequencies also as long as Eq. 2.47 is satisfied. For our choice of parameters, $\tau_B \sim 0.1$ (see Appendix. 6.6), and for numerical simulation, $\tau_D = 0.1T = 0.2\pi$ in units of ω_0^{-1}. Thus Eq. 2.47 is satisfied. The initial condition for plots shown in the figure corresponds to no particle in the system, but the agreement with numerical simulations has been checked for other initial conditions (like randomly chosen initial values of correlation functions etc.) also.

Note that numerical validation was only possible owing to the small size of the system, which allowed for using reasonably sized finite baths. For larger system sizes, much larger baths will be required and the set-up will not be amenable to numerical simulation. However, the theory can be easily used for much larger systems connected to infinite baths.

Having validated the theory, we now look at the physics of the long time dynamics

for both the cases.

Symmetric - or zero voltage - ac drive

First, we look at long time dynamics of the symmetric drive (Eq. 3.15). In this case, both chemical potentials are the exact same sinusoidal so that there is no instantaneous voltage difference, i.e, $\mu_1(t) - \mu_2(t) = 0$. Even though there is no voltage difference, as discussed before, because of being a driven system, there can still be an instantaneous current. Moreover, because of presence of displacement current, the current from the left bath, current in the system, current from the right bath can be different.

Panel (a) of Fig. 3.7 shows currents from the left (right) bath to site 1(2), $I^s_{B^{(1)} \to 2}$ ($I^s_{B^{(2)} \to 2}$), and current inside the system over one time period for the case of first resonance ($p = 1$ in Eq. 3.14). As expected from our discussion of resonance, the current inside the system is much larger than the currents from the baths. A physical explanation for the non-zero instantaneous current for zero voltage drive can be given as follows.

Let $V_0 > \omega_2$ (see Eq. 3.15). As the chemical potential varies, the Fermi energy of the particles in the bath varies. When it exceeds ω_2, particles flow into the system from the baths. When the Fermi energy of the particles in the bath is smaller than ω_1, particles flow out of the system into the baths. If the time to reach steady state is larger than the time period of the drive, this transient behavior is observed, which leads to the instantaneous current.

It is clear from this argument, that the instantaneous current increases with increase in V_0. Particularly, if $V_0 < \omega_1$, there will be a small instantaneous current. This behaviour is shown in panel (b) of Fig. 3.7 which shows the maximum instantaneous currents from the baths and inside the system as a function of V_0. The current increases continuously with V_0 and finally saturates. The saturation occurs because there are only two eigen-energy levels of the system. Actually, because of the fermionic nature of the set-up, one would expect steps or kinks at the positions $V_0 = \omega_1$ and $V_0 = \omega_2$. However, such behaviour is not observed because temperature is not low enough. On the other hand, it is important to note that the time-period averaged current is zero always because it is proportional to the difference between time-period averaged fermi distributions of the two baths.

We note that the internal current, while strictly speaking cannot be measured directly, nevertheless may have physical consequences. Specifically, such internal current may lead to local heating of the junction (due to Joule heating). This can lead for instance, to
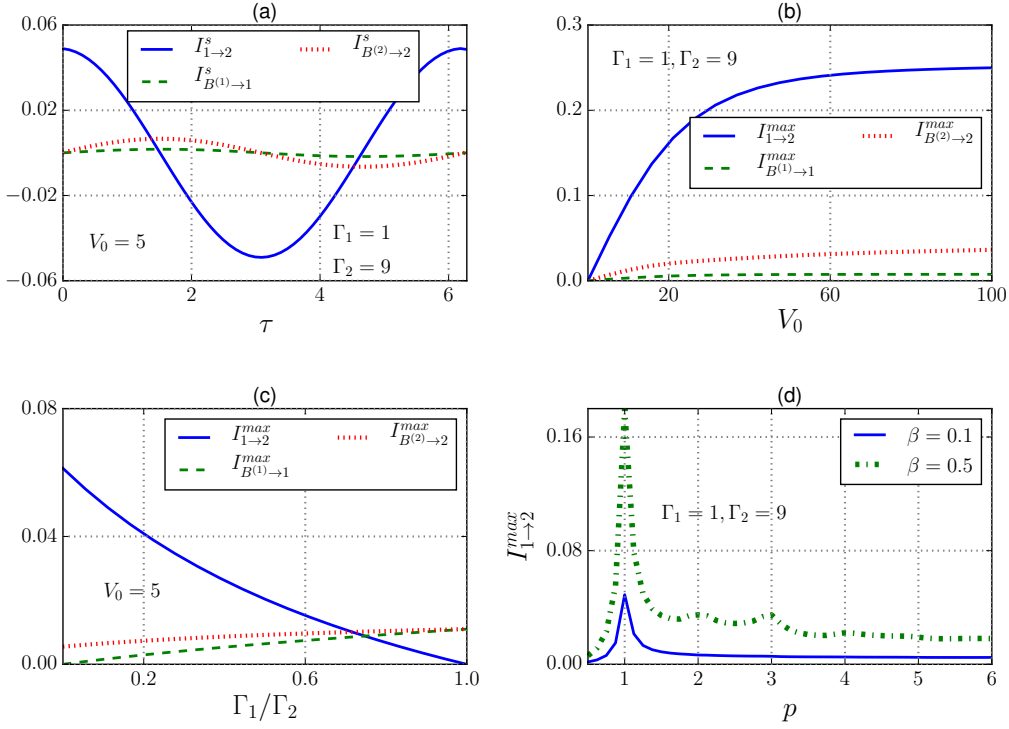
Figure 3.7: *Various currents under symmetric ac drive ($\mu_1(t) = \mu_2(t) = V_0 \sin(\Omega_0 t)$).*
Panel (a), (b), (c) describes the set-up at first resonance ($\Omega_0 = \omega_2 - \omega_1 = 2g$). Panel
(a) shows long time results of $I_{1 \to 2}^s$ and currents from the baths ($I_{B^{(1)} \to 1}^s, I_{B^{(2)} \to 2}^s$) with
asymmetric system-bath coupling ($\Gamma_1 \neq \Gamma_2$) as a function of time over one time period of
the ac drive. $I_{B^{(1)} \to 1}^s, I_{B^{(2)} \to 2}^s$ are much smaller than $I_{1 \to 2}^s$. Panel (b) shows the behavior
of the maximum currents with V_0 for asymmetric system-bath coupling. The maximum
currents increase with V_0 and finally saturates. Panel (c) shows behavior of the maximum
currents with the degree of asymmetry (Γ_1/Γ_2). The maximum current inside the system
($I_{1 \to 2}^{max}$) decreases with increase in degree of asymmetry, and becomes zero for symmetric
coupling. In contrast, maximum current from baths ($I_{B^{(1)} \to 1}^{max}, I_{B^{(2)} \to 2}^{max}$) remain non-zero and
become same for symmetric coupling. This shows a stark difference between symmetric and
asymmetric system-bath coupling, and gives an experimental way to determine asymmetry
of system-bath coupling. Panel (d) shows the maximum current in the system as a function
of $p = 2g/\Omega_0$ (Eq. 3.14) at two different temperatures. p being integer corresponds to
resonances. The first resonance peak is very strong. Higher resonance peaks are much
weaker, and are washed out by increasing temperature. Other parameters $g = 0.5, t_B =$
$200, \omega_0 = 1, \beta_1 = \beta_2 = 0.1$. All times are measured in units of ω_0^{-1}, all energies are
measured in units of $\hbar \omega_0$.

44

a breakdown of the system (in molecular junctions) or to heating-induced observable changes in current (for a double quantum dot).

Panel (c) of Fig. 3.7 shows a more interesting effect. The plot shows the maximum instantaneous current from the baths and inside the system as a function of asymmetry Γ_1/Γ_2 of the system-bath coupling (note that the chemical potentials are still symmetric). The set-up is still at first resonance. The maximum current inside the system decreases with decrease in asymmetry, and vanishes for the fully symmetric junction, $\Gamma_1/\Gamma_2 = 1$. At the same time, in the symmetric point the maximum currents from left and right baths are equal. This can be physically explained as follows. If the baths are identically coupled as well as identically driven, the particles come into the system at exactly same rate leading to same current from both baths. Since the particles are fermions, if one particle occupy each site, there can be no current in between the two sites due to Pauli exclusion principle. This leads to the fact that if rate of inflow of particles from both baths is same, there is no current between the two sites. Thus, current between the two sites of the system comes from a mismatch between rate of inflow of particles from the baths. Therefore, current inside the system increases with increase in asymmetry of system-bath coupling.

Panel (d) of Fig. 3.7 shows plots of the maximum current inside the system for asymmetric system-bath coupling with p (as defined in Eq. 3.14) for two different temperatures. When p is equal to an integer, the set-up is at resonance. Thus, from our previous discussion, the maximum current inside the system should show peaks at integer values of p. The first resonance peak is strong. However, lower frequency resonance peaks are much weaker. This is because the driving signal itself has a small contribution from such modes. Moreover, we see that higher temperature washes out the lower frequency resonances.

We point out that asymmetry in molecular junctions may be a key ingredient in deciphering its electronic transport properties and in designing single-molecule devices (see, e.g., [46, 47, 48]). Our results demonstrate that measuring the time-dependent current (for zero voltage bias but time-dependent voltages) is a direct way to measure asymmetry in molecular junctions, which can serve (in parallel to usual transport measurements) for junction characterization.
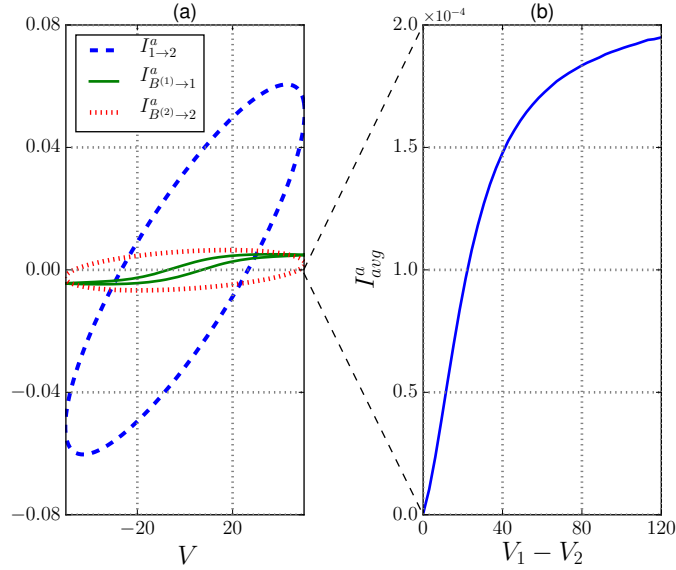
Figure 3.8: *Panel (a) shows long time results of currents vs voltage $V = \mu_1(t) - \mu_2(t)$ over one time period of ac drive ($V_1 = 50, V_2 = 5$). The system is driven by $\mu_1(t) = V_1 \cos(\Omega_0 t)$, $\mu_2(t) = V_2 \sin(\Omega_0 t)$, system-bath coupling is asymmetric ($\Gamma_1 = 0.01, \Gamma_2 = 0.09$) and system is at first resonance ($\Omega_0 = \omega_2 - \omega_1 = 2g$). The currents show hysteretic behavior, due to the dynamical nature of the charge transport in and out of the system. Because of the resonance, the current inside the system is much greater than currents from the baths. Panel (b) shows the time-period-averaged current as a function of difference between amplitudes of drives $V_1 - V_2$. ($V_2 = 5$, V_1 is varied.) The current increases first and then reaches a plateau. The averaged current is much smaller than the maximum instantaneous current. The dotted lines between the two panels highlights the difference in scale of the plots. Other parameters $g = 0.5, t_B = 200, \omega_0 = 1, \beta_1 = \beta_2 = 0.1$. All times are measured in units of ω_0^{-1}, all energies are measured in units of $\hbar\omega_0$.*

Asymmetric ac drive

Having discussed the physics of long time dynamics of the symmetric ac drive, we move to the case of the asymmetric ac drive. Consider the situation where the left chemical potential and right chemical potentials vary sinusoidally out of phase with same frequency but have different amplitude in general.

Unlike the symmetric ac drive case, here the voltage across the system $V = \mu_1 - \mu_2$ is non-zero. For $V_1 \neq V_2$. The difference between time-period averaged Fermi distributions of the two baths is not zero in this case. Hence, there is a net time-period averaged current through the system. Fig. 3.8 shows plots of currents from the baths and current

in the system at first resonance. Panel (a) shows current vs voltage ($V = \mu_1(t) - \mu_2(t)$) curve over one time period. We observe an interesting hysteresis behavior. Also, because of resonance, the current inside the system is much greater than current from the baths. This effect would not have been seen in the adiabatic limit. Panel (b) shows the time-period averaged current as a function of $V_1 - V_2$. The current increases, and finally saturates (similar to I_{max} vs V_0 curve for the symmetric drive case). Note that the time-averaged current is much smaller than the maximal instantaneous currents. This implies that perhaps time-dependent signals can be measured even when the average currents are small and below the noise level.

The hysteresis in I-V curve for asymmetric system bath coupling can potentially have device applications. This behavior depends intricately on the phase difference between the two drives, the amplitude difference of the two drives, as well as on the asymmetry of system-bath coupling. These dependences are quite complicated and a detailed investigation of the hysteresis behavior will be taken up in a future work.

The two site set-up described above is experimentally realizable using quantum dots. However, the bottleneck experimental parameter for observation of most of the above effects is frequency of the drive Ω_0. Our most interesting results are close to resonance $\Omega_0 = 2g$. The maximum frequency of ac drive currently experimentally realizable is $\sim 10 GHz$ [49]. This means to observe the above effects $g \sim 0.01 meV$. The baths must have much wider bandwidths than system energy scales, which can be easily arranged experimentally. As evidenced by Eq. 3.2, having wide bandwidths will automatically realize the weak system-bath coupling. Temperature $\sim 1mK$ (which is equivalent to $\beta \sim 0.1$) will be consistent with the Markov approximation. These experimental parameters may be challenging but not impossible. Our study thus points to new rich physics in such experimental domain.

Summary

Thus, we have tested our AC drive theory by applying it to the case of two fermionic sites with hopping between them, weakly coupled to two different baths at same constant temperature but with sinusoidally driven chemical potentials. In this we have considered two cases. We have validated our theory by comparing with exact numerics done with finite but large baths for both the cases. The first case is when the sinusoidal drive is symmetric, i.e, both chemical potentials vary in an exactly same manner so that there

is no instantaneous voltage difference. In this case, even though there is no net time-period averaged current, there is an instantaneous current, which can become quite large at resonance. Furthermore, inside the system, the instantaneous current depends on asymmetry of the system-bath coupling and becomes zero when system-bath coupling is symmetric. This gives an experimental way of detecting the asymmetry of system-bath coupling. The maximum instantaneous current increases with amplitude of drive and shows resonance peaks. Increase in temperature washes out the higher resonance peaks.

In the other case, the chemical potentials of the baths have an amplitude difference, as well as a phase difference. Due to amplitude difference, the net time-period averaged current is non-zero and increases with increase in amplitude difference. We find interesting hysteresis in the I-V curves.

In the next section, we use RQME to look at a simple interacting model.

3.2 Transport through a non-linear oscillator

[This subsection closely follows parts of discussions in the published paper (iii).]

Having dealt with linear systems, we now use the RQME approach to treat (DC) transport through a non-linear oscillator given by a single site with Bose-Hubbard interaction, , hereafter, called the single-site Bose Hubbard (SSBH) model,

$$\hat{\mathcal{H}}_S = \Omega_0 \hat{a}^\dagger \hat{a} + \chi (\hat{a}^\dagger \hat{a})^2. \tag{3.17}$$

In optics, such interaction is often called the Kerr interaction strength. In the field of hybrid quantum systems a Hamiltonian with such an interaction can be potentially experimentally realized in more than one way. The Jaynes-Cummings model, an experimentally realized light-matter system, can be tuned to the dispersive regime where it behaves like a SSBH model. The photon-spin interaction in this limit can be integrated out "pertubatively" to generate a non-linear Bose-Hubbard like interaction between photons [6, 7]. Alternatively there are interesting potential realizations of Bose-Hubbard interactions between photons which involve 4-level atoms in an optical cavity [50, 51]. These realizations offer large tunability of parameters. Specifically, while the former realization involving Jaynes-Cummings model has a small interaction strength compared to the linear term, the later realizations have very large interaction strength.

Another area of applicability for such interacting bosonic Hamiltonians, which is perhaps more suited to non-equilibrium measurements, are the fields of molecular thermo-
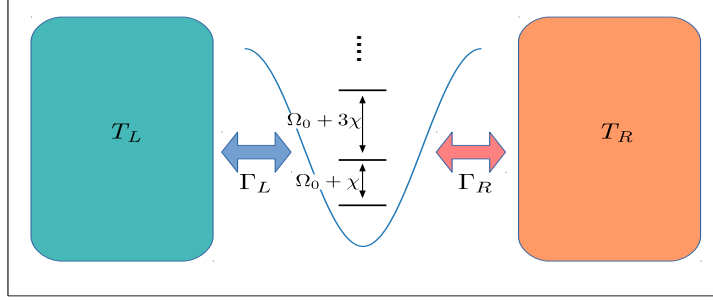
Figure 3.9: *The schematic set-up for studying transport through a non-linear oscillator described by a single-site Bose-Hubbard model (Eq. 3.17).*

electrics and nanophononics. These fields typically deal with molecular junctions connecting two reservoirs, experimentally, which are often two large chemical compounds [52, 53, 54, 55, 56, 57]. Role of interactions in phononic transport through such systems is of interest both experimentally and theoretically[58].

There has been a large amount of work on such a SSBH model with a finite interaction strength coupled to a single bath [59, 60, 61, 62, 63, 64]. On the other hand, non-equilibrium spin boson (NESB) model, which corresponds to the limit of very large interaction strength, has been well studied in out-of-equilibrium set-ups [12, 13, 65, 66, 67, 68] and is of growing experimental significance. The conductance of an anharmonic junction with quartic anharmonicity has been studied recently [69, 70]. However, there is essentially no investigation of the SSBH model with finite interaction strength in a far-from-equilibrium setup via connection with multiple reservoirs. Here, using RQME, we investigate the SSBH model weakly coupled to two bosonic baths at different temperatures beyond the linear response regime.

3.2.1 The RQME

The RQME provides a way to treat the set-up of the SSBH model connected to two baths at different temperatures (see Fig. 3.9) without any restrictions on the interaction strength χ. So, under Born-Markov approximation, we obtain results only to leading order in system-bath coupling, but arbitrary strength of interaction. The microscopically derived RQME for our system coupled to single bath was first written down in [60]. It is straightforward to generalize to two baths. Let us define $\rho \equiv Tr_B(\rho_{full})$ with ρ_{full} being the full density matrix of system+bath and $Tr_B(..)$ implying trace taken over bath

49

degrees of freedom. The RQME for the density matrix of the system ρ of our set-up is given by:

$$\frac{\partial \rho}{\partial t} = i[\rho, \hat{\mathcal{H}}_S] - \varepsilon^2 \left([\rho F(\hat{\tilde{\omega}})\hat{a}, \hat{a}^\dagger] + [\hat{a}^\dagger, G(\hat{\tilde{\omega}})\hat{a}\rho] + h.c. \right) , \qquad (3.18)$$

where

$$\hat{\tilde{\omega}} = \Omega_0 + \chi(2\hat{N} + 1),$$
$$F(\hat{\tilde{\omega}}) = F_1(\hat{\tilde{\omega}}) + F_2(\hat{\tilde{\omega}}), \ \ G(\hat{\tilde{\omega}}) = G_1(\hat{\tilde{\omega}}) + G_2(\hat{\tilde{\omega}}) \qquad (3.19)$$
$$F_\ell(\hat{\tilde{\omega}}) = \frac{1}{2}\mathfrak{J}_\ell(\hat{\tilde{\omega}})\mathfrak{n}_\ell(\hat{\tilde{\omega}}) - i\mathcal{P}\int_{-\infty}^{\infty} \frac{d\omega}{2\pi} \frac{\mathfrak{J}_\ell(\omega)\mathfrak{n}_\ell(\omega)}{\omega - \hat{\tilde{\omega}}}$$
$$G_\ell(\hat{\tilde{\omega}}) = \frac{1}{2}\mathfrak{J}_\ell(\hat{\tilde{\omega}})(\mathfrak{n}_\ell(\hat{\tilde{\omega}}) + 1) - i\mathcal{P}\int_{-\infty}^{\infty} \frac{d\omega}{2\pi} \frac{\mathfrak{J}_\ell(\omega)(\mathfrak{n}_\ell(\omega) + 1)}{\omega - \hat{\tilde{\omega}}}$$

and $h.c.$ stands for Hermitian conjugate. Note that the Redfield equation assumes $\varepsilon \ll 1$ and keeps terms only upto $O(\varepsilon^2)$, i.e, only upto quadratic in system-bath coupling (the Born approximation). In deriving the above equation, we have also done the Markov approximation which assumes that the observation time is much larger than the time scale of relaxation of bath correlation functions. To ensure weak system-bath coupling, we choose $\varepsilon = 0.1$ and $\kappa_{\ell r}$ to be of the same order as Ω_0.

In equilibrium, i.e, when $\beta_1 = \beta_2 = \beta$, $\mu_1 = \mu_2 = \mu$, it can be checked by direct substitution that the thermal state

$$\rho_{eq} = \frac{e^{-\beta(\hat{\mathcal{H}}_S - \mu\hat{N})}}{Z} \qquad (3.20)$$

is the steady state of the Eq. (3.18), where $Z = Tr\left[e^{-\beta(\hat{\mathcal{H}}_S - \mu\hat{N})}\right]$ is the equilibrium partition function.

The quantitative nature of some of our results will depend on our choice of spectral function. We assume a general spectral function which is commonly used in bosonic systems:

$$\mathfrak{J}_\ell(\omega) = \Gamma_\ell \omega^s e^{-\omega/\omega_c}\theta(\omega) , \qquad (3.21)$$

where ω_c gives the cut-off frequency and $\theta(\omega)$ is Heaviside step function. The cut-off frequency is considered very large so that the system energy levels near the edge of the bath spectrum correspond to extremely high energies, which do not really contribute to the system properties at the chosen set of temperatures and chemical potentials. This

is satisfied when $\omega_c \gg \Omega_0, \chi, \beta_1^{-1}, \beta_2^{-1}, \mu_1, \mu_2$. Also, we are concerned with a photonic or phononic system, so we will set $\mu_1 = \mu_2 = 0$ finally. Most of our results will be for the Ohmic bath, i.e, for $s = 1$. Other cases will be commented up on. The sub-ohmic bath, $s < 1$ is not consistent with the Born-Markov approximation in this case.

3.2.2 The NESS

To calculate various physical observables in NESS beyond linear response, we need to find the NESS density matrix. Also, in non-equilibrium, since we have no guess for direct substitution, we need to find the ρ directly from Eq 3.18. Since both the number operator $\hat{N}$ and the system Hamiltonian H_S are diagonal in occupation number basis, the NESS transport properties as well as average occupation and energy of the system can be found from the steady state diagonal elements of ρ in this basis. The occupation number basis satisfies

$$\hat{a}|n\rangle = \sqrt{n}|n-1\rangle, \ \ \hat{a}^\dagger|n\rangle = \sqrt{n+1}|n+1\rangle \ . \tag{3.22}$$

The evolution equation for the diagonal elements $\rho_n = \langle n|\rho|n \rangle$ is given by

$$\frac{d\rho_n}{dt} = -\varepsilon^2 \left[\rho_n(C_n + D_n) - \rho_{n-1}C_{n-1} - \rho_{n+1}D_{n+1} \right] \ , \tag{3.23}$$

where

$$C_n = C_n^{(1)} + C_n^{(2)}, \ \ D_n = D_n^{(1)} + D_n^{(2)}$$

$$C_n^{(\ell)} = (n+1)\mathfrak{J}_\ell(\omega_n)\mathfrak{n}_\ell(\omega_n), \ \ \ D_n^{(\ell)} = n\mathfrak{J}_\ell(\omega_{n-1})(\mathfrak{n}_\ell(\omega_{n-1}) + 1)$$

$$\omega_n = \Omega_0 + \chi(2n+1) \ . \tag{3.24}$$

In the steady state we set the LHS of Eq. 3.23) to zero. This leads to a difference equation. Noting that $C_{-1}^{(\ell)} = C_{-1} = 0, D_0^{(\ell)} = D_0 = 0$, we obtain, by recursion, the solution

$$\rho_n D_n = \rho_{n-1}C_{n-1} \tag{3.25}$$

$$\Rightarrow \rho_n = \rho_0 \prod_{p=1}^{n} \frac{C_{p-1}}{D_p} = \rho_0 \prod_{p=1}^{n} \frac{\sum_{\ell=1}^{2} \Gamma_\ell \mathfrak{n}_\ell(\omega_{p-1})}{\sum_{\ell=1}^{2} \Gamma_\ell(\mathfrak{n}_\ell(\omega_{p-1}) + 1)}$$

$$\text{for } n = 1, 2, 3, \dots \ . \tag{3.26}$$

The constant ρ_0 is fixed from the normalization condition $\sum_n \rho_n = 1$, i.e, trace of density matrix is unity. Thus,

$$\rho_0 = \tilde{Z}^{-1} = \left[1 + \sum_{n=1}^{\infty} \prod_{p=1}^{n} \frac{\sum_{\ell=1}^{2} \Gamma_\ell \mathfrak{n}_\ell(\omega_{p-1})}{\sum_{\ell=1}^{2} \Gamma_\ell(\mathfrak{n}_\ell(\omega_{p-1}) + 1)} \right]^{-1} \ , \tag{3.27}$$
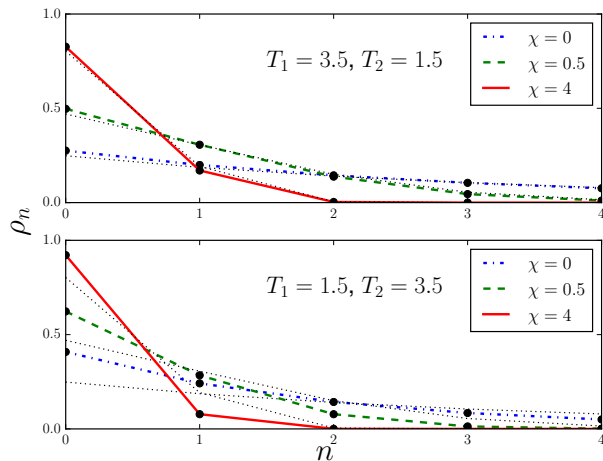
Figure 3.10: *The plot of population density (diagonal elements of density matrix in eigen-basis of system Hamiltonian) of SSBH model in equilibrium and under thermal bias with assymetric system-bath coupling ($\Gamma_1 = 0.4, \Gamma_2 = 1.6$) and $\Omega_0 = 1$. The top and bottom panels are for interchanged hot and cold baths. The three dotted lines (in each plot) are the corresponding equilibrium distributions ($T_1 = T_2 = 3.5$), i.e, Eq. 3.20 for the values of χ mentioned in the legend. The deviation from equilibrium is more prominent in the bottom panel. For large interaction strength ($\chi = 4$), only two levels have non-negligible probability, like a spin-boson model. All energy variables are measured in units of Ω_0.*

where $\tilde{Z}$ is a normalization constant and is analogous to the partition function in equilibrium systems. It can be easily checked by putting $\mathfrak{n}_1(\omega) = \mathfrak{n}_2(\omega) = \mathfrak{n}(\omega)$ in Eq. (3.26) that ρ_n indeed gives Eq. (3.20) in equilibrium. Also, in the equilibrium case, Eq. (3.25) corresponds to the detailed balance condition. In the non-equilibrium case, while this still looks like the detailed balance condition, we note that in general it is not possible to define an effective temperature. Also note that ρ_n is independent of the choice of spectral function of the bath.

The explicit expression for population ρ_n of bosons in NESS, given by Eq. 3.26, is the central result that allows us to go beyond linear response in this interacting bosonic problem. The population, in itself, is a physically measurable quantity and, as we show below, can be used to compute various other physical observables.

In Fig. 3.10, we show the plots of population density ρ_n of the system under asymmetric system-bath coupling. Since system-bath coupling is asymmetric, the out-of-equilibrium distribution changes under interchange of hot and cold baths. For high interaction

strength, i.e, for $\chi \gg \Omega_0, T_1, T_2$, only the lowest two levels have non-negligible probability. In this regime, we can truncate the energy spectrum in just two levels. Then ρ_0 and ρ_1 become

$$\rho_0 \approx \frac{\sum_{\ell=1}^2 \Gamma_\ell \big(\mathfrak{n}_\ell(\omega_0) + 1\big)}{\sum_{\ell=1}^2 \Gamma_\ell (1 + 2\mathfrak{n}_\ell(\omega_0))}, \rho_1 \approx \frac{\sum_{\ell=1}^2 \Gamma_\ell \mathfrak{n}_\ell(\omega_0)}{\sum_{\ell=1}^2 \Gamma_\ell (1 + 2\mathfrak{n}_\ell(\omega_0))}$$

$$\forall \; \chi \gg \Omega_0, T_1, T_2 \qquad (3.28)$$

with $\omega_0 = \Omega_0 + \chi$. The above results are exactly the same as obtained for a non-equilibrium spin-boson model (NESB) by using the Redfield equation [12]. Thus for $\chi \gg \Omega_0, T_1, T_2$, the system becomes identical to the NESB. Since NESB is already a well explored problem, in the following, we will be mainly interested in the physics beyond this regime. We also note that for $\chi = 0$ the system reduces to a harmonic oscillator and in this case the population $\rho_n^{\chi=0}$ is given in terms of an effective temperature $T_{eff} = 1/\beta_{eff}$, i.e $\rho_n^{\chi=0} \propto e^{-\beta_{eff}\Omega_0 n}$ with

$$\coth(\beta_{eff}\Omega_0) = \frac{\Gamma_1 \coth(\beta_1 \Omega_0) + \Gamma_2 \coth(\beta_2 \Omega_0)}{\Gamma_1 + \Gamma_2} \qquad (3.29)$$

which is consistent with the finding in Ref. [71].

3.2.3 Average occupation and energy

First we will look at the average occupation and energy of the system. These quantities are measurable in current state-of-the-art experiments in quantum light-matter hybrid systems [7, 72]. The expressions for these are given by

$$\langle \hat{N} \rangle = \sum_{n=1}^{\infty} n\rho_n = \frac{1}{\tilde{Z}} \sum_{n=1}^{\infty} n \prod_{p=1}^{n} \frac{\sum_{\ell=1}^2 \Gamma_\ell \mathfrak{n}_\ell(\omega_{p-1})}{\sum_{\ell=1}^2 \Gamma_\ell (\mathfrak{n}_\ell(\omega_{p-1}) + 1)} \; ,$$

$$\langle \hat{\mathcal{H}}_S \rangle = \sum_{n=1}^{\infty} E_n\rho_n = \frac{1}{\tilde{Z}} \sum_{n=1}^{\infty} E_n \prod_{p=1}^{n} \frac{\sum_{\ell=1}^2 \Gamma_\ell \mathfrak{n}_\ell(\omega_{p-1})}{\sum_{\ell=1}^2 \Gamma_\ell (\mathfrak{n}_\ell(\omega_{p-1}) + 1)} \; , \qquad (3.30)$$

with $E_n = \Omega_0 n + \chi n^2$.

In NESB limit, these average quantities can be trivially found from Eq. 3.28. They become $\langle \hat{N} \rangle \approx \rho_1$, and $\langle \hat{\mathcal{H}}_S \rangle \approx \omega_0 \rho_1$. We are interested in going beyond the NESB regime. So let us look at the regime of high temperatures $T_1, T_2 \gg \chi, \Omega_0$. First, we look at the normalization constant defined in Eq. 3.27. which can be written as

$$\tilde{Z} = 1 + \sum_{n=1}^{\infty} \exp\left[-\sum_{p=1}^{n} \log\left(f(\omega_{p-1})\right)\right], \quad f(\omega_p) = \frac{\sum_{\ell=1}^2 \Gamma_\ell (\mathfrak{n}_\ell(\omega_p) + 1)}{\sum_{\ell=1}^2 \Gamma_\ell \mathfrak{n}_\ell(\omega_p)} \; . \qquad (3.31)$$

Note that $f(\omega_p) > 1$, and hence $log\big(f(\omega_p)\big) > 0$. It follows that there is a energy level cut-off n^* beyond which the energy levels have negligible contribution to $\tilde{Z}$. For high enough temperatures, we can assume, $\beta_\ell \omega_p \ll 1 \; \forall p < n^*$. Under this condition, we can expand $f(\omega_p)$ to obtain (after some amount of algebra),

$$f(\omega_p) \approx 1 + \frac{\omega_p}{\tilde{T}}, \quad log\big(f(\omega_p)\big) \approx log\big(1 + \frac{\omega_p}{\tilde{T}}\big) \approx \frac{\omega_p}{\tilde{T}} \; , \tag{3.32}$$

with

$$\tilde{T} = \frac{\Gamma_1 T_1 + \Gamma_2 T_2}{\Gamma_1 + \Gamma_2} \; . \tag{3.33}$$

The contribution of terms $n > n^*$ is small and so their precise form is irrelevant. Hence we get

$$\tilde{Z} \approx 1 + \sum_{n=1}^{\infty} \exp\left[-\frac{1}{\tilde{T}} \sum_{p=1}^{n} \big(\Omega_0 + (2p-1)\chi\big) \right] = \sum_{n=0}^{\infty} \exp\left[-\frac{1}{\tilde{T}}(\Omega_0 n + \chi n^2) \right] \; . \tag{3.34}$$

Thus, for $T_1, T_2 \gg \Omega_0, \chi$ the normalization constant has the same form as the equilibrium partition function with the effective temperature $\tilde{T}$. This is consistent with the effective temperature for harmonic oscillator ($\chi = 0$) given in Eq. 3.29. For high temperatures, $\beta_{eff} = 1/\tilde{T}$. It is also interesting to note that for symmetric system-bath coupling, i.e, $\Gamma_1 = \Gamma_2$, the effective temperature is just the mean temperature, $\tilde{T} = T_m = (T_1 + T_2)/2$. However, the description in terms of an effective temperature is not possible for low temperatures, except when $\chi = 0$.

The high temperature scaling of the normalization constant can now be easily found by noting that for high temperatures, the summation can be converted into an integral. So we have

$$\tilde{Z} \approx \int_0^{\infty} dx \exp\left[-\frac{1}{\tilde{T}}(\Omega_0 x + \chi x^2) \right] \approx \frac{\sqrt{\pi}}{2} \sqrt{\frac{\tilde{T}}{\chi}} \; . \tag{3.35}$$

The second step requires the condition $\tilde{T}\chi \gg \Omega_0^2$, under which we see that the normalization constant scales as $\sqrt{\tilde{T}/\chi}$.

The above trick can be used to find high temperature scaling of average of any operator which is diagonal in the eigenbasis of the system Hamiltonian. The average of any operator $\hat{\mathcal{H}}$ which is diagonal in the eigenbasis of the system has the form

$$\langle \hat{\mathcal{H}} \rangle = \sum_{n=0}^{\infty} \rho_n h(n) = \frac{[h(0) + \sum_{n=1}^{\infty} e^{-\sum_{p=1}^{n} \log(f(\omega_{p-1}))} h(n)]}{\tilde{Z}} \; , \tag{3.36}$$
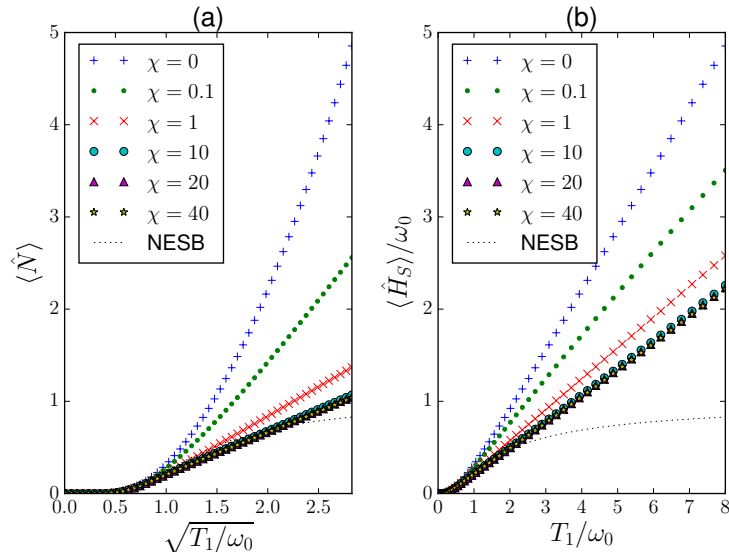
Figure 3.11: *The plot shows scaling behaviour of average occupation and average energy of the single site Bose-Hubbard model for fixed $r = T_2/T_1 = 1/3$. Here $\omega_0 = \Omega_0 + \chi$. The dotted plots correspond to the NESB model. For $\chi \gg \Omega_0$ ($\Omega_0 = 1$), there is data collapse over the entire range of temperature. Even for small $\chi(= 0.1)$, there is substantial deviation from linear ($\chi = 0$) behaviour. For high temperatures, $\langle \hat{N} \rangle$ scales as $\sqrt{T_1/\omega_0}$, while, $\langle \hat{\mathcal{H}}_S \rangle$ scales as T_1. Here the system-bath coupling is taken symmetric : $\Gamma_1 = \Gamma_2 = 1$. All energy variables are measured in units of Ω_0.*

which, for $T_1, T_2 \gg \Omega_0, \chi$, exactly following above arguments, becomes

$$\langle \hat{\mathcal{H}} \rangle \approx \frac{\sqrt{2}}{\pi} \sqrt{\frac{\chi}{\tilde{T}}} \int_0^\infty dx \exp\left[-\frac{\Omega_0 x + \chi x^2}{\tilde{T}}\right] h(x) . \tag{3.37}$$

Using this, we readily obtain the high temperature behaviour of $\langle \hat{N} \rangle$ and $\langle \hat{\mathcal{H}}_S \rangle$

$$\langle \hat{N} \rangle \approx \sqrt{\frac{\tilde{T}}{\pi \chi}}, \ \langle \hat{\mathcal{H}}_S \rangle \approx \tilde{T} + (\Omega_0 + 2\chi)\sqrt{\frac{\tilde{T}}{\pi \chi}} . \tag{3.38}$$

Thus $\langle \hat{N} \rangle$ should show a data collapse for various χ and vary as a function of $\sqrt{\tilde{T}/\chi}$, whereas, $\langle \hat{\mathcal{H}}_S \rangle / \chi$ varies as $\tilde{T}/\chi$ and should show a data collapse for $\chi \gg \Omega_0$.

To check the above high temperature discussion and the connection with equilibrium behaviour, we now first define

$$r = \frac{T_2}{T_1} , \tag{3.39}$$

which quantifies the degree of deviation from equilibrium, $r = 1$ corresponding to equilibrium. To ensure that the system is far from equilibrium, we keep r fixed at $r < 1$. We note that, if r is kept fixed, all the NESS results become a function of only one temperature, say, T_1. We choose T_1/ω_0, where $\omega_0 = \Omega_0 + \chi$, as the scaling variable since it can be used both in the highly interacting regime (where $\chi \approx \omega_0$) and the linear regime (where $\chi = 0$). Also in the NESB regime, with r fixed, all NESS quantities vary as a function of T_1/ω_0, as can be checked from Eq. 3.28.

In Fig. 3.11, we plot $\langle \hat{N} \rangle$ and $\langle \hat{\mathcal{H}}_S \rangle / \omega_0$ as a function of T_1/ω_0. Note that Eq. 3.30, and not any simplified expression, was used to calculate $\langle \hat{N} \rangle$ and $\langle \hat{\mathcal{H}}_S \rangle$ in the plots. The plots clearly show data collapse over the entire temperature regime for $\chi \gg \Omega_0$. Also, important to note, is the substantial effect of small interaction strengths at high temperatures. The high temperature scaling behaviour for small interaction strengths is same as that for large interaction strengths, but there is no data collapse. This is because, the condition $\tilde{T}\chi \gg \Omega_0^2$ means that, for small χ, there are large subleading terms. The low temperature behaviour matches with NESB. Since all these observations are valid for any choice of r, it follows that they are all valid in equilibrium (i.e, $r = 1$) also. This is consistent with previous results in [60].

The crucial point in above discussion was to find that high temperature non-equilibrium results can be described via an effective temperature $\tilde{T}$. In the following, we will see that even transport properties at high temperatures can be described in terms of $\tilde{T}$.

3.2.4 Currents

Now we look at the average transport properties of the system, in particular we compute particle and energy currents. To calculate current we look at the evolution equations of the expectation values $\langle \hat{N} \rangle$ and $\langle \hat{\mathcal{H}}_S \rangle$ of $\hat{N}$ and $\mathcal{H}_S$. Since $\hat{N}$ and $\hat{\mathcal{H}}_S$ are diagonal in the eigenbasis of the system Hamiltonoan we can directly obtain the evolution of their expectation values from Eq. (3.23). This gives

$$\frac{d\langle \hat{N} \rangle}{dt} = \sum_n n \frac{d\rho_n}{dt} = \varepsilon^2 \sum_n \left(\rho_n C_n - \rho_n D_n \right) , \tag{3.40}$$

$$\frac{d\langle \hat{\mathcal{H}}_S \rangle}{dt} = \sum_n (\Omega_0 n + \chi n^2) \frac{d\rho_n}{dt} = \varepsilon^2 \sum_n \left(\omega_n \rho_n C_n - \omega_{n-1} \rho_n D_n \right) . \tag{3.41}$$

Collecting all terms depending on each bath separately, the above equations can be written like continuity equations of the forms $d\langle \hat{N} \rangle/dt = I_1 - I_2, d\langle \hat{\mathcal{H}}_S \rangle/dt = J_1 - J_2$, where I_ℓ (J_ℓ) is the particle (energy) current flowing into the system from ℓth bath. In steady state, $I_1 = I_2 = I$ and $J_1 = J_2 = J$. The steady state expressions for currents are :

$$I = \varepsilon^2 \sum_{n=0}^{\infty} \rho_n (C_n^{(1)} - D_n^{(1)}) = \sum_{n=1}^{\infty} \rho_n n \mathcal{I}(\omega_{n-1}) ,$$

$$J = \varepsilon^2 \sum_{n=0}^{\infty} \rho_n (\omega_n C_n^{(1)} - \omega_{n-1} D_n^{(1)}) = \sum_{n=1}^{\infty} \rho_n \omega_{n-1} n \mathcal{I}(\omega_{n-1}) , \tag{3.42}$$

with

$$\mathcal{I}(\omega_{n-1}) = \varepsilon^2 \left[\frac{\Gamma_1 \Gamma_2 \mathfrak{J}(\omega_{n-1})(\mathfrak{n}_1(\omega_{n-1}) - \mathfrak{n}_2(\omega_{n-1}))}{\Gamma_1 \mathfrak{n}_1(\omega_{n-1}) + \Gamma_2 \mathfrak{n}_2(\omega_{n-1})} \right] . \tag{3.43}$$

The second steps of Eq. 3.42 have been arrived at from the first steps after some simplification using the property of NESS density matrix given in Eq. 3.25. Note that energy and particle currents are not independent. But, in general, there is no way of directly finding one current given the other and they can have quite different behaviour. Fig. 3.12 shows variation of energy and particle currents with interaction strength χ for Ohmic baths ($(s = 1$ in Eq. 3.21)), for both forward ($\Delta T > 0$) and backward ($\Delta T < 0$) biases. The mean temperature $T_m = (T_1 + T_2)/2$ is kept fixed in the plots, and system-bath coupling is asymmetric ($\Gamma_1 \neq \Gamma_2$). The plots immediately show us a number of physical aspects of the system.

Firstly, we note that the particle current decreases with increase in interaction strength χ. This is expected because of increasing repulsive interaction in the system. On the other hand, energy current shows non-monotonic behaviour with χ. This is plausible because,
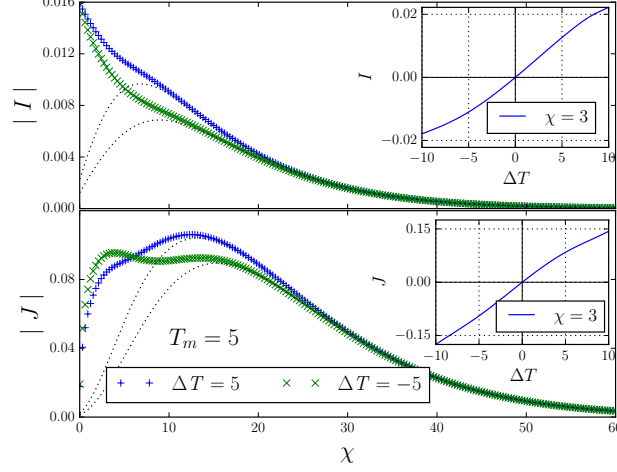
Figure 3.12: *Plot of particle (top panel) and energy (bottom panel) currents as a function of interaction strength χ for transport under both forward and backward bias for Ohmic baths ($s = 1$ in Eq. 3.21) under asymmetric system bath coupling ($\Gamma_1 = 0.4, \Gamma_2 = 1.6$). Here mean temperature $T_m = (T_1 + T_2)/2 = 5$ for both plots. The two black dotted lines in each plot correspond to the NESB currents for $\Delta T = \pm 5$. The currents from our model match the NESB currents for large χ. Particle current decreases with χ, while energy current behaves non-monotonically with χ. The forward and backward currents do not match, thereby showing rectification effect. The direction of rectification of energy current is reversed beyond a value of χ. It follows that at this value of χ, the energy current does not show rectification. The insets show the corresponding currents as a function of $\Delta T = T_1 - T_2$ for a chosen value of $\chi = 3$ and $T_m = 5$. It can be seen that I and J deviate from odd-function behaviour which is signature of rectification. Other parameters are $\varepsilon = 0.1$, $\omega_c = 1000$. All energy variables are measured in units of Ω_0, and time is measured in units of Ω_0^{-1}.*

while, with increasing χ, system allows less number of particles to pass, higher energy particles have a larger probability to pass through the system.

Secondly, we see that there is rectification of both energy and particle currents, since the particle and energy currents for forward and backward biases do not match. This is to be expected because the expressions for currents in Eq. 3.42 are not antisymmetric under interchange of hot and cold baths (i.e, $\mathfrak{n}_1 \leftrightarrow \mathfrak{n}_2$) in general. It is only so under special conditions. Two of such special conditions where there is no rectification are when $\chi = 0$, i.e, when the system is linear, and when $\Gamma_1 = \Gamma_2$ (for any χ). These can be easily checked from the expressions for currents (Eq. 3.42). Hence, in general, there will be rectification effects in both particle and energy currents for $\chi \neq 0$ and $\Gamma_1 \neq \Gamma_2$. This is the generic behaviour in non-linear (interacting) systems.

Thirdly, as discussed before, for $\chi \gg \Omega_0, T_1, T_2$, the system behaves as NESB, and currents match with the NESB results. But, the rectification in the NESB limit is less than that for smaller interaction strengths. Thus rectification behaviour is non-monotonic as a function of χ. Our findings therefore suggest that a careful engineering of the system Hamiltonian is required to get maximum rectification from a given system.

Finally, and most interestingly, for small interaction strength, the rectification of energy current occurs in the opposite direction to rectification of particle current. Also, there is a non-zero value of χ where the forward and backward energy currents match, and hence there is no rectification. At this point, the system rectifies particle current but not the energy current. Beyond this value of χ, energy and particle rectification occur in the same direction (see Fig. 3.12, bottom panel).

In what follows, we investigate the behaviour of particle and energy currents and rectification in more detail along with their scaling behaviour.

Scaling behaviour of currents

As we have seen with average system properties, transport properties also behave differently for different relative values of temperatures and interaction strength. In the NESB regime, $\chi \gg \Omega_0, T_1, T_2$, the currents are given by

$$I_{SB} \approx \frac{\varepsilon^2 \Gamma_1 \Gamma_2 \mathfrak{J}(\omega_0)(\mathfrak{n}_1(\omega_0) - \mathfrak{n}_2(\omega_0))}{\Gamma_1(1 + 2\mathfrak{n}_1(\omega_0)) + \Gamma_2(1 + 2\mathfrak{n}_2(\omega_0))} \ ,$$

$$J_{SB} \approx \omega_0 I_{SB} \ , \tag{3.44}$$

with $\omega_0 = \Omega_0 + \chi$. This is identical to the expression for current previously derived for NESB [12]. Note that in NESB regime, energy current is proportional to particle current. This is because, in this limit, transport is allowed through transfer of exactly one particle through the system, and that particle has energy $\Omega_0 + \chi$. This is not valid beyond the NESB regime.

Now, let us look at the high temperature regime, $T_1, T_2 \gg \chi, \Omega_0$, where NESB results are not valid. We note that the expression for the currents in Eq. 3.42 has the same form as Eq. 3.36. So, the high temperature trick in Eq. 3.37 can be readily applied to obtain

$$I^{\tilde{T} \gg \Omega_0, \chi} \approx \sqrt{\frac{2\chi}{\pi^2 \tilde{T}}} \int_0^\infty dx\, e^{-\frac{\Omega_0 x + \chi x^2}{\tilde{T}}} (x+1) \mathcal{I}(\omega_x) \ ,$$

$$\approx \sqrt{\frac{2\chi}{\pi^2 \tilde{T}}} \int_0^\infty dx\, e^{-\frac{\Omega_0 x + \chi x^2}{\tilde{T}}} (x+1) A\mathfrak{J}(\omega_x) \frac{\Delta T}{\tilde{T}} \ ,$$

$$J^{\tilde{T} \gg \Omega_0, \chi} \approx \sqrt{\frac{2\chi}{\pi^2 \tilde{T}}} \int_0^\infty dx\, e^{-\frac{\Omega_0 x + \chi x^2}{\tilde{T}}} (x+1) \omega_x A\mathfrak{J}(\omega_x) \frac{\Delta T}{\tilde{T}} \ , \tag{3.45}$$

with $A = \varepsilon^2 \Gamma_1 \Gamma_2 / (\Gamma_1 + \Gamma_2)$ and $\Delta T = T_1 - T_2$. In the second step above, we have expanded the Bose distributions in $\mathcal{I}(\omega_n)$ (Eq. 3.43) for high temperatures to obtain $\mathcal{I}(\omega_n) \approx A\mathfrak{J}(\omega_n) \Delta T / \tilde{T}$. Using the general form of spectral function given in Eq. 3.21, and after some algebra, we obtain

$$I^{\tilde{T} \gg \Omega_0, \chi} \approx K(s) = \frac{A \Delta T}{\sqrt{\pi} \tilde{T}} \int_0^\infty dy \left[y^{-\frac{1}{2}} e^{-y} \left(\sqrt{\frac{\tilde{T} y}{\chi}} + 1 \right) \left(\Omega_0 + \chi + 2\sqrt{\tilde{T} \chi y} \right)^s \right] \ ,$$

$$J^{\tilde{T} \gg \Omega_0, \chi} \approx K(s+1). \tag{3.46}$$

For the choice of spectral function in Eq. 3.21, we can relate particle and energy currents via the function $K(s)$. We now look at the properties of the function $K(s)$. First, we look at the regime $\tilde{T} \gg \chi \gg \Omega_0$. In this regime, $K(s)$ becomes

$$\frac{K(s)}{\chi^{s-1} \Delta T} \approx \frac{A}{\sqrt{\pi}} \frac{\chi}{\tilde{T}} \mathcal{F}\left(\frac{\tilde{T}}{\chi}, s \right) \ , \tag{3.47}$$

$$\mathcal{F}(z, s) = \frac{A}{\sqrt{\pi}} \frac{\chi}{\tilde{T}} \int_0^\infty dy \left[y^{-\frac{1}{2}} e^{-y} \left(\sqrt{zy} + 1 \right) \left(1 + 2\sqrt{zy} \right)^s \right] \ .$$

This then gives

$$\frac{K(s)}{\chi^{s-1} \Delta T} \approx \frac{2^s A}{\sqrt{\pi}} \left(\frac{\tilde{T}}{\chi} \right)^{\frac{s-1}{2}} \int_0^\infty dy\, e^{-y} y^{\frac{s}{2}}, \quad \forall\ \tilde{T} \gg \chi \gg \Omega_0 \ . \tag{3.48}$$

We immediately make the following observations. Firstly, for $T_1, T_2 \gg \chi \gg \Omega_0$, $K(s)/(\chi^{s-1}\Delta T)$ varies as a function of $\tilde{T}/\chi$. Thus, $I/(\chi^{s-1}\Delta T)$ and $J/(\chi^s \Delta T)$ for various values of χ should show a data collapse when plotted with $\tilde{T}/\chi$.

Secondly, we see $K(1) \approx A\Delta T$. It follows that for Ohmic baths ($s = 1$ in Eq. 3.21) at high temperatures, particle current is independent of the interaction strength χ and one gets a linear-response-like relation $I \approx A\Delta T$, even for large temperature bias. This is consistent with high temperature result for a harmonic oscillator ($\chi = 0$). However, the energy current $J \sim \sqrt{\tilde{T}/\chi}\Delta T$ and shows the effect of interaction. On the other hand for constant bath ($s = 0$), the energy current J always satisfies the linear-response-like relation, whereas the particle current is suppressed by a factor $\sqrt{\chi/\tilde{T}}$.

Thirdly, we note that the quantity $J/(\chi I)$ varies as a function of $\tilde{T}/\chi$ and scales as $\sqrt{\tilde{T}/\chi}$ for any s,

$$\frac{J}{\chi I} \approx \frac{\mathcal{F}(\tilde{T}/\chi, s+1)}{\mathcal{F}(\tilde{T}/\chi, s)} \approx 2\sqrt{\frac{\tilde{T}}{\chi}}\left(\frac{\int_0^\infty y^{\frac{s+1}{2}}e^{-y}dy}{\int_0^\infty y^{\frac{s}{2}}e^{-y}dy}\right)$$

$$\forall \ T_1, T_2 \gg \chi \gg \Omega_0 \tag{3.49}$$

In the other regime, $T_1, T_2 \gg \Omega_0 \gg \chi$, the scaling behaviour is the same, but the data collapse is difficult to see because of large sub-leading terms.

Note that, $I/\Delta T$ and $J/\Delta T$ actually give the *beyond linear response* analog of particle and energy conductance. For linear response, $\tilde{T} = T$ in the RHS of Eq. 3.47, T being the equilibrium temperature. Then, the above discussion gives the high temperature scaling of conductance.

In Fig. 3.13, we show the scaling behaviour of $I/\Delta T$ and $J/\Delta T$ as a function of T_1/ω_0. As in Sec. (3.2.3), we have chosen T_1/ω_0 as the relevant scaling variable and have kept r fixed at $r < 1$ to ensure beyond linear response regime. $r \to 1$ gives the linear response conductance. The plots (a) and (b) of Fig. 3.13 are then the beyond-linear-response equivalent of temperature scaling of conductance. Note that Eq. 3.42 (and not any simplified expression) was used to calculate currents. The plots show the scaling behaviour discussed above. The plots for $\chi \gg \Omega_0$ show data collapse over the entire range of temperatures. Also, the low temperature behaviour is given by NESB.

In Fig. 3.13(a), we plot $I/\Delta T$ for fixed r for Ohmic baths ($s = 1$ in Eq. 3.21). We see that, for NESB, this quantity behaves non-monotonically with temperature, while for our non-equilibrium SSBH model, this quantity monotonically increases with temperature. In fact, the deviation from NESB result starts precisely at the point where the NESB result reaches a maximum. Similar behaviour is observed for $J/(\Delta T \omega_0)$ in Fig. 3.13(b). We conclude that, the non-monotonic behaviour of conductance of NESB, both at and beyond linear response, comes as a result of truncation of the energy spectrum and is
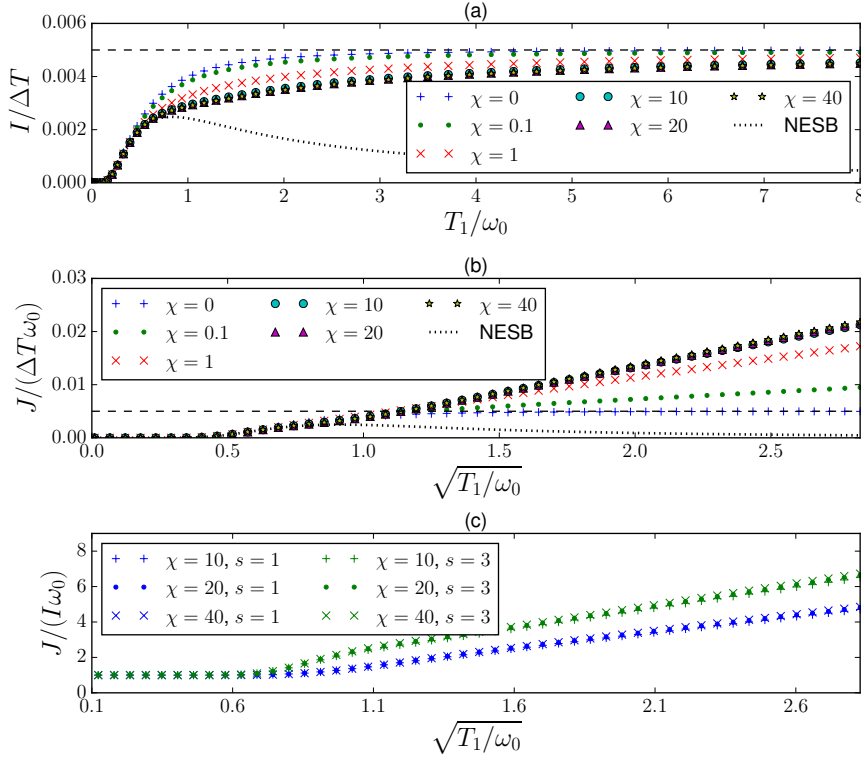
Figure 3.13: *Panel (a) and (b) show the scaling behaviour of $I/\Delta T$ and $J/(\Delta T \omega_0)$ for Ohmic baths ($s = 1$ in Eq. 3.21) and for fixed $r = \frac{T_2}{T_1} = \frac{1}{3}$. The dotted lines show the corresponding NESB result. The horizontal dashed lines in panel (a) and panel (b) correspond to $I/\Delta T = J/(\Delta T \omega_0) = A = \varepsilon^2 \Gamma_1 \Gamma_2/(\Gamma_1 + \Gamma_2)$, which is the high temperature result for the harmonic oscillator ($\chi = 0$). For $\chi \gg \Omega_0$ ($\Omega_0 = 1$), there is a data collapse for all temperatures. The NESB result matches with the non-equilibrium SSBH model for small temperatures. At higher temperatures, the NESB result shows non-monotonicity, which is not seen in the non-equilibrium SSBH model which demonstrates a stark difference between the two models. In panel (a), $I/\Delta T$ approaches a constant value at high temperatures irrespective of the strength of interaction strength. In panel (b), even for small interaction strength ($\chi = 0.1$), substantial deviation from linear ($\chi = 0$) behaviour is noticeable. Panel (c) shows data collapse of $J/(I\omega_0)$ for all temperatures for $\chi \gg \Omega_0$. Irrespective of choice of bath spectral function and for fixed $r(= \frac{1}{3})$, $J/(I\omega_0)$ shows a data collapse and goes as $\sim \sqrt{T_1/\omega_0}$ for $T_1 \gg \omega_0$. All observations are also valid in linear response regime (i.e, $r \approx 1$), and give the temperature scaling of conductance. Other parameters are: $\varepsilon = 0.1$, $\omega_c = 1000$, $\Gamma_1 = \Gamma_2 = 1$. All energy variables are measured in units of Ω_0, and time is measured in units of Ω_0^{-1}.*

not observed when all energy levels are considered. This demonstrates a major difference between the high temperature behaviour of non-equilibrium SSBH model and the NESB model.

Also, it follows from Fig. 3.13(a), that, for Ohmic baths ($s = 1$ in Eq. 3.21), at high temperatures the particle current (for fixed ΔT) becomes independent of both interaction strength and the effective temperature. Fig. 3.13(b) shows a considerable deviation from linear behaviour even for small interaction strengths.

Fig. 3.13(c) shows that, consistent with our previous discussion, irrespective of the choice of bath spectral function, the quantity $J/(I\omega_0)$, for $\chi \gg \Omega_0$, shows a data collapse and goes as $\sim \sqrt{T_1/\omega_0}$ for $T_1 \gg \omega_0$ (with r kept fixed).

Having discussed the scaling behaviour of currents in detail, we now look into another important property of interacting systems, the rectification of current.

Rectification

Rectification of current is a generic behaviour of non-linear (interacting) systems in non-equilibrium. As we have seen, in a non-equilibrium set-up, two kinds of currents through the system can be defined, the particle current and the energy current, and their rectification behaviour can also be quite different. To our knowledge, there has been no previous work where both particle and energy current rectification for a bosonic non-linear system has been investigated. Also, note that rectification can only be observed beyond linear response regime.

Since rectification occurs only for asymmetric system-bath coupling, we use the following definition to describe the degree of asymmetry

$$\Gamma_1 = \Gamma(1 - \gamma), \ \ \Gamma_2 = \Gamma(1 + \gamma) \ , \tag{3.50}$$

where $0 \leq \gamma \leq 1$ is dimensionless. Given a value of asymmetry parameter γ, we define a measure of rectification as

$$R_I = \frac{I(\Delta T, \gamma) + I(-\Delta T, \gamma)}{I(\Delta T, \gamma = 0)}, \ R_J = \frac{J(\Delta T, \gamma) + J(-\Delta T, \gamma)}{J(\Delta T, \gamma = 0)} \ . \tag{3.51}$$

R_I and R_J are the particle and energy current rectifications. This measure of rectification is as used in [12, 13]. Note that, by this definition, rectification is positive if higher current flows when the cold bath is more strongly coupled to the system. Also, R_I and R_J are zero when $\gamma = 0, 1$. In our following discussion of rectification, we will primarily confine ourselves to the Ohmic baths ($s = 1$ in Eq. 3.21).
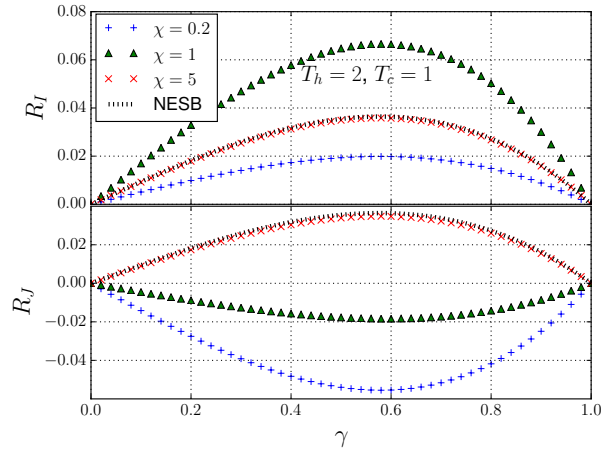
Figure 3.14: *The plot shows particle rectification R_I (top) and energy rectification R_J (bottom) as a function of asymmetry parameter γ for various values of interaction strength χ and Ohmic baths ($s = 1$ in Eq. 3.21). R_I and R_J are as defined in Eq. 3.51. The black dotted line corresponds to NESB. The rectfications become maximum when $\gamma \approx 0.6$. Also, rectification of both particle and energy currents show a non-monotonic change with χ. Rectification for large χ matches with the NESB result. Energy rectification changes direction with increase in χ. Other parameters are as folows: $\varepsilon = 0.1$, $\omega_c = 1000$. All energy variables are measured in units of Ω_0, and time is measured in units of Ω_0^{-1}.*

Figure 3.15: *The plot shows rectification of particle current (top panel) and of energy current (bottom panel) of SSBH model out-of-equilibrium for fixed $r = \frac{T_2}{T_1} = \frac{1}{3}$, for Ohmic baths ($s = 1$ in Eq. 3.21). $\omega_0 = \Omega_0 + \chi$. R_I and R_J are as defined in Eq. 3.51. The veritca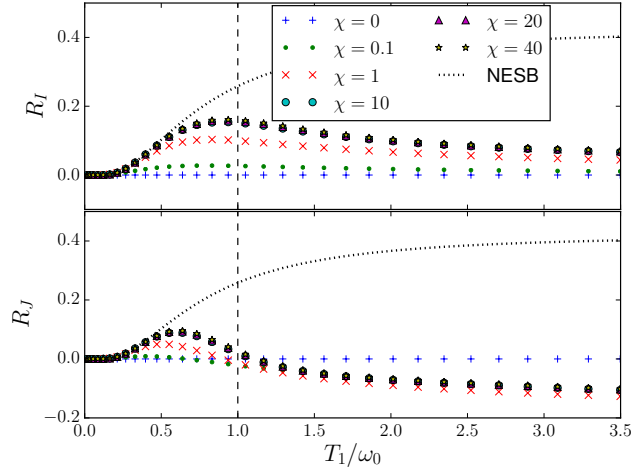l dashed line indicates the positions of $T_1/\omega_0 = 1$. The dotted plots correspond to the NESB model. For $\chi \gg \Omega_0$, ($\Omega_0 = 1$), there is data collapse. Both R_I and R_J has a maximum for $\omega_0 < T_1$. $R_J = 0$ for $\omega_0 \approx T_1$. R_J shows reversal in direction of rectification beyond this point. Other parameters are as folows: $\varepsilon = 0.1$, $\omega_c = 1000$. All energy variables are measured in units of Ω_0 and time is measured in units of Ω_0^{-1}.*

The variation of R_I and R_J with γ is shown in Fig. 3.14. Irrespective of the strength of interaction strength, we notice that the maximum rectification occurs when $\gamma \approx 0.6$. The figure also shows, both particle and energy rectifications behave non-monotonically with χ. For small χ, R_J is negative while R_I is positive, hence, direction of energy rectification is opposite to particle rectification. For large χ, the rectification is same as that obtained from NESB. In the NESB regime, particle and energy rectifications are same, because, particle current is proportional to energy current. All these observations are consistent with our discussion of Fig. 3.12.

To concisely investigate the rectification behaviour of the system as a function of the interaction strength and the temperatures, we again resort to the scaling variable T_1/ω_0 with r fixed at $r < 1$. The plots of R_I and R_J as a function of T_1/ω_0 for fixed r for Ohmic baths are shown in Fig. 3.15. We readily make the following observations :

Firstly, for $\chi < \Omega_0$, rectification is small. For $\chi \gg \Omega_0$, there is data collapse as expected from the scaling of currents.

Secondly, where NESB matches the non-equilibrium SSBH model, there is small rectification. This can be understood from expression for currents in NESB regime given in Eq. 3.44. NESB result holds when $\chi \gg \Omega_0, T_1, T_2$. Therefore, in this regime $\omega_0 \gg T_1, T_2$. So the bose distributions in Eq. 3.44 are exponentially small. Hence, $1 + \mathfrak{n}(\omega_0) \approx 1$. With this approximation, the expressions of currents in Eq. 3.44 become antisymmetric under interchange of hot and cold baths. Thus the NESB regime of the SSBH model gives very small rectification. Maximum particle rectification R_I is reached when $\omega_0 < T_1$ which is outside this regime.

Thirdly, after the maximum, R_I gradually approaches zero with increase in T_1/ω_0. This is expected because, as we have seen before, at high temperatures, for Ohmic baths, the particle current eventually has the form, $I \approx A\Delta T$, which is antisymmetric under interchange of hot and cold baths. On the other hand, the corresponding NESB rectification (the dotted line in Fig. 3.15) continues to increase with T_1/ω_0, until it saturates to a high value. Thus, as an effect of having all energy levels, and not truncating at two levels, the particle rectification is suppressed at high temperatures.

Fourthly, and most interestingly, energy rectification R_J also has a peak for $\omega_0 < T_1$. However, $R_J = 0$ at $\omega_0 \approx T_1$. At this point, the particle rectification is still positive. So the system behaves as a particle rectifier and not as an energy or heat rectifier. Beyond that point, R_J changes sign. Thus the direction of rectification is reversed. With further increase in T_1/ω_0, energy rectification continues to grow in the reversed direction. Therefore, at high temperatures, the heat rectification occurs in the opposite direction to particle rectification, and continues to grow as temperatures of both hot and cold baths are increased.

Note that all the above observations are for Ohmic baths ($s = 1$ in Eq. 3.21). Finally, we discuss the case of non-Ohmic baths. For superohmic baths (i.e, for $s > 1$), both particle and energy currents show a reversal of direction of rectification. The reversal of energy rectification for superohmic bath occurs at a lower value of T_1/ω_0 than that for the Ohmic bath. However, in all cases, both particle and energy rectifications vary non-monotonically with the interaction strength.

3.2.5 Transient time dynamics

Until now, we have discussed the properties of the NESS of the out-of-equilibrium SSBH model. In this section, we look at the transient time dynamics of the various physical

quantities we have so far calculated in NESS.

To do this we revert to the equation for time evolution of ρ_n, Eq. 3.23. The equation can be re-written and solved in the form

$$\frac{\partial \tilde{\rho}(t)}{\partial t} = -\varepsilon^2 \mathcal{M} \tilde{\rho}(0) \Rightarrow \tilde{\rho}(t) = e^{-\varepsilon^2 \mathcal{M} t} \tilde{\rho}(0) \tag{3.52}$$

where $\tilde{\rho}$ is an infinite dimensional column vector containing diagonal elements of the density matrix and $\mathcal{M}$ is a infinite dimensional non-Hermitian square matrix containing the entries of Eq. 3.23. $\mathcal{M}$ has the form

$$\mathcal{M} = \begin{bmatrix} C_0 + D_0 & -D_1 & 0 & \dots & \dots & \dots \\ -C_0 & C_1 + D_1 & -D_2 & 0 & \dots & \dots \\ 0 & -C1 & C_2 + D_2 & -D_3 & 0 & \dots \\ \vdots & \ddots & \ddots & \ddots & \ddots & \ddots \end{bmatrix} \tag{3.53}$$

where C_n and D_n are as defined in Eq. 3.24. Note that the matrix M has the form of a Markov matrix. The sum of each column is zero ($D_0 = 0$ by definition). This corresponds to the fact that the trace of the density matrix is preserved, i.e, $\sum_n \rho_n = 1$.

To calculate the time dynamics, we choose an initial state with no particles in the system, i.e, initially, $\rho_0(0) = 1$, and $\rho_n(0) = 0 \ \forall n \neq 0$. The Eq. 3.52 is used to numerically obtain the time evolution. Even though the matrices involved are infinite dimensional, for given interaction χ and temperatures T_1 and T_2, only a finite number of levels, determined by the ratio of the temperatures and the interaction, effectively contribute. Thus, starting from a finite matrix size, a convergence is reached as the matrix size is increased. Smaller interaction and higher temperatures require larger matrix sizes. A subtle point to note is that, if the matrix $\mathcal{M}$ is truncated at any finite size, say p, then the constraint that the sum of each column should be zero is not satisfied for the pth column, unless $C_p = 0$. Consequently, the matrix $\mathcal{M}$ can be truncated at size p only if $C_p \ll D_p$.

Since we are using Redfield equation under Born-Markov approximation to obtain transient time dynamics, we need to be careful in choosing the observation times. This is because, as we have seen before, Markov approximation is valid only when observation times are much larger than the time τ_B for decay of bath correlation functions. For our choice of parameters, $\tau_B \sim 2$, in units of Ω_0^{-1} (see Appendix. 6.6).

Time dynamics of physical quantities $\langle N(t) \rangle$, $\langle H_s(t) \rangle$, $I(t)$, $J(t)$ for Ohmic baths ($s = 1$ in Eq. 3.21) are shown in Fig. 3.16, where $I_1(t)$ and $J_1(t)$ are respectively particle
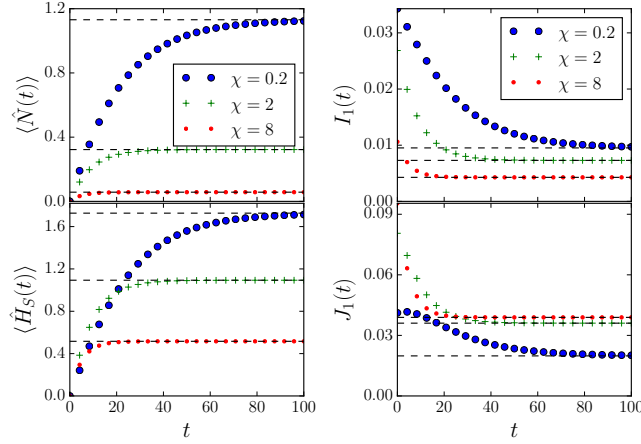
Figure 3.16: *The figure shows time dynamics of (a) average occupation, $\langle \hat{N}(t) \rangle$, (b) average energy, $\langle \hat{H}_s(t) \rangle$, (c) particle current from left bath, $I_1(t)$, and (d) energy current from left bath, $J(t)$, for various values of interaction strength and for a temperature bias $T_1 = 4$ and $T_2 = 2$ for Ohmic baths ($s = 1$ in Eq. 3.21). All physical quantities demonstrate a non-unitary evolution towards a steady state. The approach to steady state is faster for higher interactions. Since physical quatities plotted here are diagonal in the eigenbasis of the system Hamiltonian, none of them shows oscillations with time. Other parameters are $\Omega_0 = 1, \varepsilon = 0.1, \Gamma_1 = 0.4, \Gamma_2 = 1.6, \omega_c = 1000$. All energy variables are measured in units of Ω_0, and time is measured in units of Ω_0^{-1}.*

Figure 3.17: *The figure shows a log-log plot of time to reach NESS, t_{ss} (as defined in Eq. 3.54) as a function of interact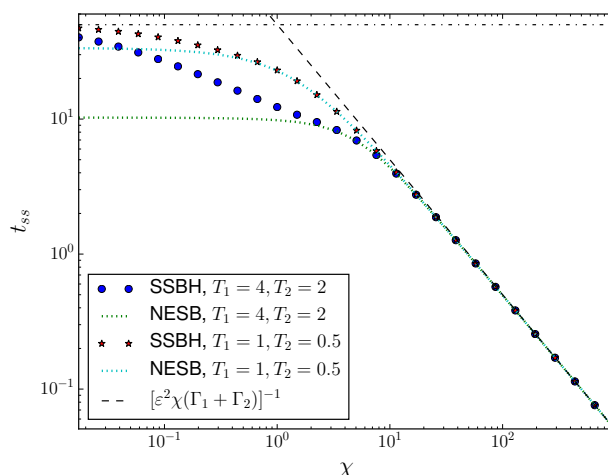ion strength χ for Ohmic baths ($s = 1$ in Eq. 3.21). The horizontal dash-dotted line corresponds to $\left[\varepsilon^2 \sum_{\ell=1}^{2} \mathfrak{J}_\ell(\Omega_0) \right]^{-1}$ which is the t_{ss} for the linear ($\chi = 0$) system. For large χ, $t_{ss} \approx \left[\varepsilon^2 \chi \left(\Gamma_1 + \Gamma_2 \right) \right]^{-1}$, and this is indicated by the dashed line. For intermediate χ, t_{ss} depends on the temperatures of the hot and cold baths. Other parameters are $\Omega_0 = 1, \varepsilon = 0.1, \Gamma_1 = 0.4, \Gamma_2 = 1.6, \omega_c = 1000$. All energy variables are measured in units of Ω_0, and time is measured in units of Ω_0^{-1}.*

and energy currents from the left bath into the system. (Before reaching steady state, the currents from left and right baths are not the same.) We observe that, unlike the two site non-interacting case seen before, here, the currents show no oscillations. More interestingly, we also observe that the time to reach steady state, called t_{ss} hereafter, decreases with increase in the interaction. In the following, we investigate the dependence of t_{ss} on set-up parameters more carefully.

We note from the solution of $\tilde{\rho}(t)$ in Eq. 3.52 that time can be scaled as $\varepsilon^2 t$. It follows that $t_{ss} \propto \varepsilon^{-2}$. Thus, time to reach steady state increases as system-bath coupling becomes weaker.

It is also clear from Eq. 3.52 that the steady state is given by the eigenvector of the matrix $\mathcal{M}$ corresponding to zero eigenvalue. The fact that a unique steady state is reached in long time then implies that all other eigenvalues of the $\mathcal{M}$ have positive real part. Interestingly, we have found in our numerical computation that the eigenvalues of $\mathcal{M}$ are all real (and hence no oscillations in time). The smallest non-zero eigenvalue then

gives a measure of t_{ss}. So, we define

$$t_{ss} \equiv \frac{1}{\varepsilon^2 \lambda_1} \,, \tag{3.54}$$

λ_1 being the smallest non-zero eigenvalue of $\mathcal{M}$.

Even though t_{ss} cannot be calculated for all set-up parameters analytically, in two limiting cases, analytical results can be obtained. The first case corresponds to the NESB regime $\chi \gg \Omega_0, T_1, T_2$. In this case, $C_1 \ll D_1$, only two levels effectively contribute and matrix M has the form

$$\mathcal{M} \approx \begin{bmatrix} C_0 & -D_1 \\ -C_0 & D_1 \end{bmatrix} \tag{3.55}$$

The non-zero eigenvalue of $\mathcal{M}$ is

$$\lambda_1 = [\varepsilon^2 t_{ss}]^{-1} \approx C_0 + D_1 = \sum_{\ell=1}^{2} \mathfrak{J}_\ell(\omega_0) \left(2\mathfrak{n}_\ell(\omega_0) + 1\right) \tag{3.56}$$

The time to reach steady state therefore also depends on the temperatures of the baths. However, for large $\omega_0 = \Omega_0 + \chi$, the Bose distributions are expotentially small. Thus, for $\chi \gg \Omega_0, T_1, T_2$ and for general bath of the form given in Eq. 3.21,

$$t_{ss} \approx \frac{1}{\varepsilon^2 \chi^s \left(\Gamma_1 + \Gamma_2\right)} \,, \tag{3.57}$$

which is independent of the temperatures of the baths. We also see that, for constant baths ($s = 0$ in Eq. 3.21), t_{ss} is independent of interaction strength. For other baths, t_{ss} decreases with increase of interaction strength as a power law.

The second case where t_{ss} can be analytically, calculated corresponds to the linear system, $\chi = 0$. In this case, C_n does not decay with n (Eq. 3.24 for $\chi = 0$) and hence the matrix $\mathcal{M}$ cannot be truncated at any finite size. So, the above method of finding t_{ss} fails. However, since, in this case, we have a non-interacting system, we can find t_{ss} directly from the evolution equation for $\langle \hat{N}(t) \rangle$. The evolution equation for $\langle \hat{N}(t) \rangle$ can be obtained from Eq. 3.40 by setting $\chi = 0$. The resulting equation can be written and solved in the form

$$\frac{d\langle \hat{N}(t) \rangle}{dt} = -\varepsilon^2 \langle \hat{N}(t) \rangle \sum_{\ell=1}^{2} \mathfrak{J}_\ell(\Omega_0) + \varepsilon^2 \sum_{\ell=1}^{2} \mathfrak{J}_\ell(\Omega_0) \mathfrak{n}_\ell(\Omega_0)$$

$$\Rightarrow \langle \hat{N}(t) \rangle = \left(\langle \hat{N}(0) \rangle - N_{ss} \right) e^{-\varepsilon^2 t \sum_{\ell=1}^{2} \mathfrak{J}_\ell(\Omega_0)} + N_{ss} \tag{3.58}$$

with $N_{ss} = \left[\sum_{\ell=1}^{2} \mathfrak{J}_\ell(\Omega_0) \mathfrak{n}_\ell(\Omega_0) \right] / \left[\sum_{\ell=1}^{2} \mathfrak{J}_\ell(\Omega_0) \right]$ being the NESS occupation. From above equation, it is clear that for $\chi = 0$, the t_{ss} is given by

$$t_{ss} = \frac{1}{\varepsilon^2 \sum_{\ell=1}^{2} \mathfrak{J}_\ell(\Omega_0)} \tag{3.59}$$

This is again independent of the temperatures of the baths.

Except for these two limiting cases, t_{ss} needs to be found numerically using the definition Eq. 3.54. Fig. 3.17 shows log-log plot of numerically obtained t_{ss} as a function of interaction strength χ for Ohmic baths for two different choices of temperatures of hot and cold baths. It is seen that except for the limiting cases, t_{ss} depends on the temperatures of the baths. The limiting cases show the behaviour discussed above.

3.2.6 Summary

We have investigated a system consisting of a single bosonic site with Bose-Hubbard interaction weakly coupled to two bosonic baths at different temperatures. We have used the RQME method to obtain analytical results beyond linear response regime. Below, we summarize our main findings and their potential applications.

We have found an analytical result for the population density (diagonal elements of the density matrix in the eigenbasis of system Hamiltonian) of the system in NESS (Eq. 3.26). This has further allowed us to find various physical observables like average occupation and energy, as well as the particle and energy currents in NESS. We have then analytically found interesting scaling behaviour of the physical observables. Our main finding in this respect is that the high temperature behaviour of the system can be described in terms of an effective temperature (Eq. 3.33). Then, it follows that, with the ratio r of the temperatures of cold and hot baths fixed, there occurs a data collapse for various strengths of interaction strength χ, when various physical observables of the system are plotted in terms of the scaling variable T_1/ω_0 (Figs. 3.11,3.13,3.15). The scaling behaviours hold for a general choice of bath spectral functions of the form given in Eq. 3.21. We have also found very interesting rectification behaviour of the system. The most interesting finding is that, for Ohmic and subohmic baths ($0 < s \le 1$ in Eq. 3.21), the energy current shows a reversal in direction of rectification (Fig. 3.15). It follows that there is a non-zero strength of interaction strength, ($\chi \approx T_1 - \Omega_0$, for Ohmic baths), where energy or heat rectification is zero. At this point, the system behaves as a particle rectifier but not as a heat rectifier. For superohmic baths ($s > 1$ in Eq. 3.21),

both particle and energy currents show reversal in direction of rectification. Therefore careful engineering of baths can lead to various interesting rectification behaviour of the system. Such phenomena can be potentially used to create quantum devices, such as, optical diodes. Reversal of direction of thermal rectification of a quantum system has also been previously theoretically seen for a Heisenberg spin chain out of equilibrium [73]. Further, we have computed non-unitary time-dynamics of all the above mentioned physical quantities. We found that, except for constant baths, the time to reach steady state is shorter for higher interactions and higher system-bath couplings. For constant baths, with increase in interaction, the time to reach steady state approaches a constant independent of the strength of interaction. For large χ, the time to reach steady state goes as $t_{ss} \sim \left[\varepsilon^2 \chi^s\right]^{-1}$ for a general choice of bath spectral functions of the form given in Eq. 3.21. All our results also are consistent with the linear, $\chi = 0$ (harmonic oscillator) case, as well as the NESB, $\chi \gg \Omega_0, T_1, T_2$, case.

Our results are experimentally relevant in quantum hybrid systems, where a single site Bose-Hubbard model can be realized, as well as, in molecular junction systems, where our set-up describes a model for anharmonic junctions.

Chapter 4

Transport in extended systems

Having dealt with small systems, in this chapter, we now look at (DC) transport properties of extended systems. In section 4.1, we first review the various ways of classifying transport behaviors. In section 4.2, we then look at transport behavior in 1D quasiperiodic systems. We obtain the high temperature phase diagrams and show a case where different ways of classifying transport give drastically different results. Finally, in section 4.3, we explore the connections between the various ways of classifying transport behavior.

4.1 Review of different ways of classifying transport behavior

We first review the various ways of classifying transport behavior of extended systems. They broadly fall into two categories.

4.1.1 The isolated system in the thermodynamic limit

For an isolated system in thermodynamic limit, the standard linear-response theory can be applied. The most direct way of characterizing transport behavior in this case is by calculating the conductivity via the Green-Kubo formalism. This relates conductivity to integrated total current autocorrelation of the isolated system in the thermodynamic limit in equilibrium. In the following we will only consider particle conductivity. Equivalent treatment is also possible for thermal conductivity. Let the system of interest be described by the system Hamiltonian $\hat{\mathcal{H}}_S$. We will also assume that total particle number $\hat{N}_S$ is

conserved. Let the total particle current operator of an isolated system of length L be given by $\hat{I}_S$. Then the standard Green-Kubo formula for particle conductivity is given by

$$\sigma_{GK} = \lim_{\tau \to \infty} \lim_{L \to \infty} D_L(\tau), \tag{4.1}$$

$$D_L(\tau) = \int_0^\tau dt \int_0^\beta d\lambda \langle \hat{I}_S(-i\lambda)\hat{I}_S(t)\rangle / L \tag{4.2}$$

where $\langle ... \rangle = Tr(\frac{e^{-\beta(\hat{\mathcal{H}}_S - \mu\hat{N}_S)}}{Z}...)$, β being the inverse temperature and μ being the chemical potential of the system. The order of limits in the Green-Kubo conductivity formula is important and cannot be interchanged, and the formula is strictly valid only for infinite system size. But in numerics, one will always have a finite size. To go about numerically calculating Green-Kubo conductivity, one has to look at the behaviour of $D_N(\tau)$ for given system size, for times before the finite-size effects become substantial. If $\hat{\mathcal{H}}_S$ has time translation and time-reversal symmetries, and is 'local', the Green-Kubo formula can be related to the spread of correlations. The proof of this is quite involved. The proof in detail, clearly mentioning the assumptions made is given in Appendix. 6.7.

A system described by a 'local' Hamiltonian can be broken up into surfaces transverse to direction of current flow such that

$$\hat{N}_S = \sum_{p=-\infty}^{\infty} \hat{n}_p, \quad \frac{d\hat{n}_p}{dt} = \hat{I}_p - \hat{I}_{p-1}, \quad \hat{I}_S = \sum_{p=-\infty}^{\infty} \hat{I}_p \tag{4.3}$$

where $\hat{n}_p$ is the local particle density and $\hat{I}_p$ is the local current, and we have already assumed the thermodynamic limit. The Green-Kubo conductivity given in terms of spread of correlations is then,

$$\sigma_{GK} = \lim_{\tau \to \infty} \frac{\beta}{2} \frac{d}{d\tau} m_2^{nn}(\tau), \quad m_2^{nn}(\tau) = \sum_{x=-\infty}^{\infty} x^2 \mathrm{Re}(C(x,t)), \quad C(x,t) = \langle \hat{n}_x(\tau)\hat{n}_0(0)\rangle - \langle \hat{n}_x\rangle\langle \hat{n}_0\rangle. \tag{4.4}$$

Transport behaviour can hence be classified via scaling of $m_2^{nn}(t)$ with time t. For normal diffusive transport,

$$m_2^{nn}(t) = 2Dt, \quad \sigma_{GK} = \lim_{\tau \to \infty} \lim_{L \to \infty} D_L(\tau) = \beta D \ . \tag{4.5}$$

Hence, for normal diffusive transport, we expect that, for large enough L, $D_L(\tau)$ will converge to this value as τ increases, before finite-size effects become substantial.

In general,

$$m_2^{nn}(t) \sim t^{2\tilde{\beta}}. \tag{4.6}$$

As seen above $\tilde{\beta} = 0.5$, for normal diffusive transport. For ballistic transport, $\tilde{\beta} = 1$. If $0.5 < \tilde{\beta} < 1$, transport is super-diffusive. For both super-diffusive and ballistic transports, as seen from Eqs. 4.4,4.5, the σ_{GK} diverges. If $0 < \tilde{\beta} < 0.5$, the transport is sub-diffusive, while for a localized system, $\tilde{\beta} = 0$. In both these cases, σ_{GK} is zero. All cases other than the normal diffusive transport are broadly classified as anomalous transport.

If $\mathrm{Re}\,(C(x,t))$ scales as

$$\mathrm{Re}\,(C(x,t)) \sim (1/t^{\tilde{\beta}}) f(x/t^{\tilde{\beta}}), \tag{4.7}$$

then automatically $m_2^{nn}(t) \sim t^{2\tilde{\beta}}$. For normal diffusive transport, $\mathrm{Re}\,(C(x,t))$ is also expected to be a Gaussian, $\mathrm{Re}\,(C(x,t)) \sim e^{-\frac{x^2}{4Dt}}/\sqrt{4\pi Dt}$. But there may be cases where $m_2^C(\tau) = 2D\tau$ and $\mathrm{Re}\,(C(x,t))$ is non-Gaussian [74, 75, 76, 77, 78, 79, 80, 81]. However, there may occur cases where $C(x,t)$ does not follow a particular scaling form. As shown in Eq. 4.4, even then, the conductivity of the system depends only the time scaling of second moment, and classification of transport based on that is possible. Although all the results here are for quantum systems, high temperature limit of all the results give the answers for classical systems.

In numerics, one always has a finite system size. So the relevant time scaling of $m_2^{nn}(t)$ is before some cut-off time τ_L, after which the finite-size effects become important. The cut-off time τ_L increases with system size L.

4.1.2   Open system

For the open system also, let us only consider particle conductivity. Let the system be connected to two baths at two ends having a chemical potential difference but at same temperature. The open system characterization of transport is done via scaling of NESS particle conductance G with system length L. Here L is the length of the system in between the two baths. The open system conductivity is defined as

$$\sigma_{open} = \lim_{L \to \infty} LG. \tag{4.8}$$

For a diffusive system, conductivity σ_{open} is finite, so $G \sim L^{-1}$. For ballistic transport, current is independent of system size, so $G \sim L^0$. If $G \sim L^{-\tilde{\alpha}}$, with $0 < \tilde{\alpha} < 1$, transport is super-diffusive. In both super-diffusive and ballistic cases, the σ_{open} diverges. If $G \sim L^{-\tilde{\alpha}}$, with $\tilde{\alpha} > 1$, transport is sub-diffusive while for a localized system, $G \sim e^{-L}$ and in these cases, the σ_{open} vanishes.

The open system classification and the isolated system classification discussed in the previous subsection are generically expected to be consistent. But, there may also be cases where the isolated system in the thermodynamic limit and the open system have very different transport behaviors. The fundamental difference between σ_{open} and σ_{GK} is the following. In calculating σ_{GK}, as given in Eq. 4.1, the thermodynamic limit $L \to \infty$ is taken before taking $t \to \infty$ limit. As a consequence, the system can be considered really isolated and there is no effect of any bath. On the other hand, in calculating σ_{open}, the $t \to \infty$ limit is taken first so that the NESS is reached, and then the $L \to \infty$ limit taken. Physically, in the open system approach, there is the effect of a boundary between the system and the bath, while in the Green-Kubo approach, because of taking the thermodynamic limit first, there is no boundary. It is this that may lead to drastically different transport behaviors in the isolated and the open systems. In the following, we will see one such case. We will also investigate in detail in a very general set-up, the relation between σ_{open} and σ_{GK}.

4.2 Transport in 1D quasi-periodic non-interacting systems

[This section closely follows discussions in the published papers (iv), (v).]

In 1D non-interacting systems, presence of even a small amount of disorder leads to spatial localization of eigenstates in the absence of interactions (non-linearities). This is called Anderson localization. In contrast, 1D quasiperiodic non-interacting systems have much richer transport behavior. Quasiperiodic non-interacting and interacting models have been in limelight recently owing to experimental realization in various controllable set-ups and the possibility of observing topological effects and many-body localizations in them [82, 83, 84, 85, 86, 87, 88, 89, 90]. Such lower dimensional systems can also be connected to higher dimensional systems in presence of a magnetic field (like a quantum-Hall set-up) [91, 92, 86]. Such models are not only of interest in Physics, but are also studied in Mathematics [93, 94]. A paradigmatic example of such a system in one-dimension is the Aubry-André-Harper (AAH) model [95, 96]. In the AAH model, with increasing strength of the quasiperiodic potential, there occurs a phase transition from all states being delocalized to all states being localized and hence no mobility edge. We will study the high temperature transport properties of this model and a generalization of this model which

has a mobility edge.

These systems are described by Hamiltonians of the form

$$\hat{\mathcal{H}}_S = \sum_{r=1}^{N} V_r \hat{a}_r^\dagger \hat{a}_r + \sum_{r=1}^{N-1} (\hat{a}_r^\dagger \hat{a}_{r+1} + \hat{a}_{r+1}^\dagger \hat{a}_r) \qquad (4.9)$$

where $\hat{a}_r$ correspond to fermionic annihilation operators defined respectively on r-th lattice point of the system of N sites. The hopping parameter has been set to 1, and this is taken as the energy scale. Also, we will consider lattice spacing to be unity and hence system length $L = N$. V_r is the quasiperiodic potential. For such systems, the local current operator is $\hat{I}_p = i(\hat{a}_p^\dagger \hat{a}_{p+1} - \hat{a}_{p+1}^\dagger \hat{a}_p)$. The Green-Kubo formula for such systems is obtained by using $\hat{I}_S = \sum_{p=1}^{N} \hat{I}_p$ in Eq. 4.1.

$$\sigma_{GK} = \lim_{\tau \to \infty} \lim_{N \to \infty} D_N(\tau), \quad D_N(\tau) = \int_0^\tau \int_0^\beta d\lambda \sum_{p,q=1}^{N-1} \langle \hat{I}_p(-i\lambda) \hat{I}_q(t) \rangle / N. \qquad (4.10)$$

$C(x,t)$ can be written down in terms of the single particle eigenfunctions. We shift the origin to the site $N/2$ and define $x = r - N/2$. We have $\hat{a}_\ell(t) = \sum_{p=1}^{N} G(\ell, t \mid p, 0) \hat{a}_p(0)$, where $G(\ell, t \mid p, 0)$ is the single particle Green's function for the closed system. Let $\Phi_{\ell\alpha}$ be the ℓth component of the single-particle eigenvector corresponding to the single-particle energy eigenvalue ω_α. Thus $\hat{a}_\ell = \sum_{\alpha=1}^{N} \Phi_{\ell\alpha} \hat{A}_\alpha$ where $\hat{A}_\alpha$ are the annihilation operators in the eigenbasis. Here α is eigenstate index and ℓ is the site index. Then $G(\ell, t \mid p, 0) = \sum_{\alpha=1}^{N} e^{-i\epsilon_\alpha t} \Phi_{\ell\alpha} \Phi_{p\alpha}$. In terms of these, we have,

$$C(x,t) = \langle \hat{n}_x(t) \hat{n}_0(0) \rangle - \langle \hat{n}_x \rangle \langle \hat{n}_0 \rangle$$

$$= \sum_{\ell,p=1}^{N} \left[G^*(x + N/2, t \mid \ell, 0) G(x + N/2, t \mid p, 0) \langle \hat{a}_\ell^\dagger(0) \hat{a}_{N/2}(0) \rangle \langle \hat{a}_p(0) \hat{a}_{N/2}^\dagger(0) \rangle \right]$$

$$= \sum_{\alpha,\nu=1}^{N} \left[\Phi_{x+N/2\ \alpha} \Phi_{x+N/2\ \nu} \Phi_{N/2\ \alpha} \Phi_{N/2\ \nu} e^{i(\omega_\omega - \epsilon_\nu)t} n_F(\omega_\alpha)(1 - n_F(\omega_\nu)) \right], \qquad (4.11)$$

where $n_F(\omega) = \left[e^{\beta(\omega - \mu)} + 1 \right]^{-1}$ is the fermi distribution function.

Another related quantity often used to characterize transport [97, 98, 99, 100] in non-interacting systems is the spread of a wavepacket. Let the wavepacket $\psi_r(t)$ be initially localized at the site $N/2$ of the lattice. It evolves according to the Schroedinger equation

$$i\partial\psi_r/\partial t = \psi_{r+1}(t) + \psi_{r-1}(t) + V_r\psi_r(t). \qquad (4.12)$$

We look at the probability $P(x,t) = \mid \psi_x(t) \mid^2$, and its moments

$$m_{2p}(t) = \sum_{x=-N/2}^{N/2-1} (x - \langle x \rangle)^{2p} P(x,t), \qquad (4.13)$$
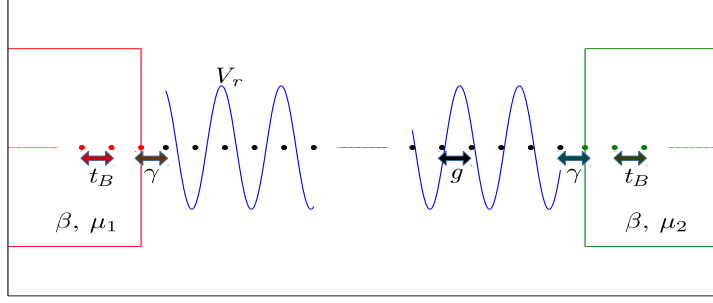
Figure 4.1: *The schematic of the set-up considered for investigation of open system properties of the 1D quasiperiodic systems. The on-site quasiperiodic potential is given by V_r, which is incommensurate with the lattice. The baths are at same inverse temperature β, but the chemical potentials μ_1 and μ_2 are different. The hopping between system sites is g (which is taken as $g = 1$). The explicit model of the baths are as in Eq. 3.1.*

where $\langle x \rangle = \sum_{x=-N/2}^{N/2-1} x P(x, t)$ is the mean. In terms of single-particle wave functions $P(x, t)$ is given by,

$$P(x, t) = \mid G(x + N/2, t \mid N/2, 0) \mid^2 = \sum_{\alpha, \nu = 1}^{N} \Phi_{x+N/2\ \alpha} \Phi_{x+N/2\ \nu} \Phi_{N/2\ \alpha} \Phi_{N/2\ \nu} e^{i(\omega_\alpha - \omega_\nu)t}.$$

(4.14)

This is different from $C(x, t)$ (see Eq. 4.11) by only the factor $n_F(\omega_\alpha)(1 - n_F(\omega_\nu))$ inside the summation. At high temperatures, $n_F(\omega) \sim 1/2$. Thus, at high temperatures,

$$\beta \to 0, \quad C(x, t) \to \frac{P(x, t)}{4}.$$

(4.15)

So the scaling properties of $C(x, t)$ and $P(x, t)$, and hence of $m_2^{nn}(t)$ and $m_2(t)$ are same at high temperatures. Thus, if $C(x, t)$ scales as in Eq. 4.7, then $P(x, t)$ also scales the same way and $[m_{2n}(t)]^{1/n} \sim t^{2\tilde{\beta}}$. The connection to different regimes of transport as discussed before is immediate.

For the open system, the system is connected to two baths at different chemical potentials at the two ends (see Fig. 4.1) and NESS properties can be calculated exactly via QLE as described before. The full Hamiltonian of the system+bath reads as $\mathcal{H} = \mathcal{H}_S + \mathcal{H}_B + \mathcal{H}_{SB}$,

$$\hat{\mathcal{H}}_B = \hat{\mathcal{H}}_B^{(1)} + \hat{\mathcal{H}}_B^{(N)}, \quad \hat{\mathcal{H}}_B^{(p)} = \sum_s \Omega_{ps} \hat{B}_{ps}^\dagger \hat{B}_{ps}, p = 1, N, \quad \hat{\mathcal{H}}_{SB} = \sum_s (\tilde{\kappa}_{ps} \hat{B}_{ps}^\dagger \hat{a}_p + h.c.).$$

(4.16)

Here $\hat{B}_{ps}$ is the annihilation operator of the sth mode of the of the bath attached to pth site of the system. The baths are connected at the 1st and the Nth sites of the system.

Here we consider the case where all operators are fermionic. The baths are initially at same temperature but different chemical potentials. So, we the bath Fermi distributions are given by

$$n_F^{(p)}(\omega) = \left[e^{\beta(\omega-\mu_p)} + 1\right]^{-1}, \quad p = 1, N.$$
(4.17)

The explicit model of bath we will choose will be the one given in Eq. 3.1. Thus, the baths are modelled via semi-infinite tight-binding chains with hopping parameter t_B and bilinearly connected to the system at the one end via system-bath coupling γ. For this case, we have already calculated the bath spectral function

$$\mathfrak{J}(\omega) = \frac{2\gamma^2}{t_B}\sqrt{1 - \left(\frac{\omega}{2t_B}\right)^2},$$
(4.18)

in Eq. 3.2. We will also assume that the two baths have identical spectral functions $\mathfrak{J}(\omega)$. The NESS quantities of our interest will be the particle current I, the particle conductance G and the occupation of the rth site $\langle \hat{n}_r \rangle$. These are can be obtained exactly via QLE (Sec. 2.2)

$$I = \int \frac{d\omega}{2\pi} T(\omega)[\,n_F^{(1)}(\omega) - n_F^{(N)}(\omega)], \quad G = \beta \int \frac{d\omega}{2\pi} T(\omega) n_F(\omega)[1 - n_F(\omega)]$$

$$T(\omega) = \frac{\mathfrak{J}^2(\omega)}{|\det(\mathbb{M}(\omega))|^2},$$

$$\langle \hat{n}_r \rangle = \int \frac{d\omega}{2\pi}\Big[\,|\,\mathbb{G}_{r1}(\omega)\,|^2\,n_F^{(1)}(\omega) + |\,\mathbb{G}_{rN}(\omega)\,|^2\,n_F^{(N)}(\omega)\Big],$$
(4.19)

where $T(\omega)$ is the transmission function, and $\mathbb{M}(\omega)$ and $\mathbb{G}(\omega)$ are as given in Eq. 2.25, 2.27.

At high temperatures, $I \simeq (\mu_1 - \mu_2)G$. So system-size scaling of current can be used to classify transport. Also, note that the system Hamiltonians under consideration, Eq. 4.9 is of the same form as in Eq. 6.37 of Appendix. 6.4. This means, the simple expression for conductance given in Eq. 6.47 will be applicable in the limit of vanishing system-bath coupling. The simple form in Eq. 6.47 will be important for understanding some of the interesting physics in the following.

4.2.1 Transport in Aubry-André-Harper model

The model

The AAH model is given by the Hamiltonian

$$\hat{\mathcal{H}}_S = \sum_{r=1}^{N-1}(\hat{a}_r^\dagger \hat{a}_{r+1} + h.c) + \sum_{r=1}^{N} 2\lambda \cos(2\pi b r + \phi)\hat{a}_r^\dagger \hat{a}_r$$
(4.20)

where b is an irrational number and ϕ is an arbitrary phase, $\hat{a}_r$ correspond to fermionic (bosonic) annihilation operators defined respectively on r-th lattice point of the system of N sites. The hopping parameter has been set to 1, and this is taken as the energy scale. When $\lambda < 1$, all the (single particle) energy eigenstates of this model are delocalized and when $\lambda > 1$, all energy eigenstates are localized. $\lambda = 1$ is the critical point. The eigenstates at the critical point are neither totally delocalized nor localized, but are 'critical' [101]. Via a transformation (akin to a Fourier transform) a dual to the AAH model can be obtained, where localized and delocalized regimes are interchanged. At the critical point, the AAH model is self-dual under this transformation [95].

This holds true for any choice of irrational number b and phase ϕ. The most popular choice for b is the golden mean $(\sqrt{5} - 1)/2$. However, in experiments and numerics all numbers are essentially rational in a strict mathematical sense. The way around is given by the fact that for a system of finite size N, if b is taken as a rational number p/q with $q > N$, b remains 'effectively irrational' and all the observed physics of AAH model is retained. In recent experiments [82, 83, 84], physics of AAH model has been explored by superimposing a $532nm$ optical lattice with a $738nm$ one, making $b = 532/738$. For $q < N$, the system becomes delocalized. Even though the choice of b is irrelevant for various interesting universal features of the AAH model, the exact nature of plots depend on b. In this work, we have considered the following choices of b : golden mean $(\sqrt{5}-1)/2$, silver mean $\sqrt{2}-1$ and the rational number 532/738 used in the experiments in [82, 83, 84]. Further, we perform an average over the phase ϕ by numerically exactly integrating the final results between 0 and 2π and dividing by 2π.

The main question we will be investigating is the nature of transport at the critical point $\lambda = 1$.

Isolated system in thermodynamic limit

We numerically investigate transport behavior of the AAH model in the isolated thermodynamic limit via exact diagonalization. All our results are given up to times before finite-size effects become substantial. We are primarily interested in the transport properties of the AAH model at the critical point ($\lambda = 1$). Fig. 4.2 shows plot of $D_N(\tau)$ with τ for different system sizes, at the critical point for $b = \sqrt{2} - 1$. We see that with increasing N, $D_N(\tau)$ converges to a curve which initially increases and then shows large fluctuations about a constant mean value. Consistently, $m_2^{nn}(t) \sim 0.288t$, and the mean
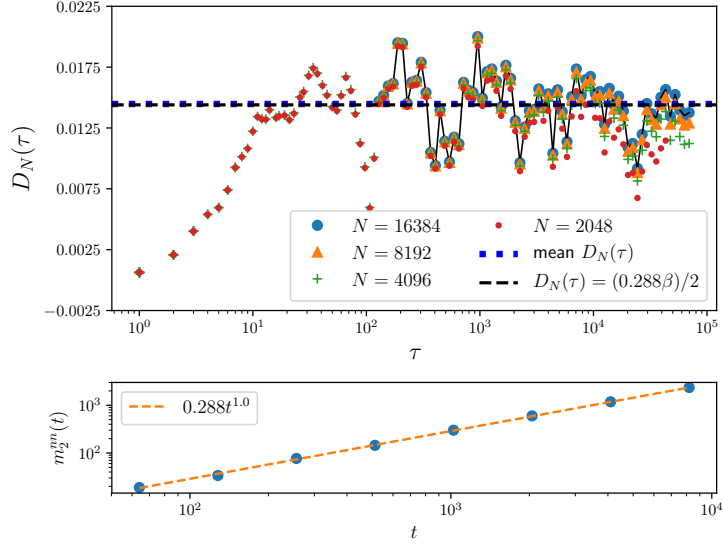
Figure 4.2: **Isolated thermodynamic limit**: *Top panel shows plot of $D_N(\tau)$ as a function of τ at the critical point $\lambda = 1$ for different system sizes. $D_N(\tau)$ initially increases with τ and then shows large fluctuations about a constant mean value. This mean value is quite precisely given by the analytical high temperature approximation result $D_N(\tau) \simeq \beta D$. D is obtained by time scaling of m_2^{nn} (Eq. 4.5) shown in bottom panel. $D = 0.288/2$. For $N = 8192, 16384$, only the large time results have been calculated. The black continuous line is guide-to-eye joining data points for $N = 16384$. The mean $D_N(\tau)$ is calculated from the data points for $N = 16384$. Parameters: $\beta = 0.1$, $\mu = 1$, $b = \sqrt{2} - 1$.*
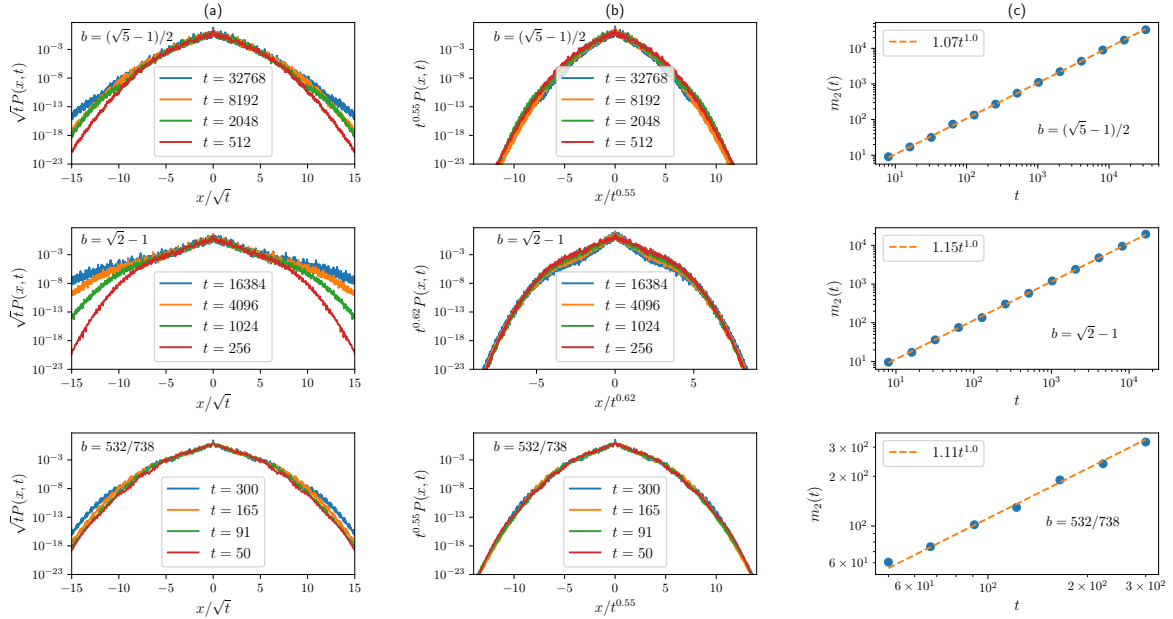
Figure 4.3: **Isolated thermodynamic limit**: *(a) The full distributions $P(x,t) = |\psi(x,t)|^2$, scaled assuming normal diffusive behaviour. Here $x = r - N/2$. $P(x,t)$ scales as $P(x,t) \simeq (1/\sqrt{t})f_1(x/\sqrt{t})$ over a considerable region in the bulk but the scaling function $f_1(z)$ is clearly not Gaussian and also the tails do not collapse. (b) $P(x,t) = |\psi(x,t)|^2$ scaled to collapse the tails of the distribution. The tails show a super-diffusive scaling $P(x,t) \simeq (1/t^{\tilde{\beta}})f_2(x/t^{\tilde{\beta}})$ with $\tilde{\beta} > 0.5$. However, the value of $\tilde{\beta}$ depends on the choice of b. (c) The scaling of second moment $m_2(t)$ of $P(x,t)$ with t for various values of b. $m_2(t) \sim t$. $N = 8192$ for $b = (\sqrt{5}-1)/2, \sqrt{2}-1$. $N = 700$ for $b = 532/738$.*

value is precisely given by βD (see Eqs. 4.5). This seems to suggest that σ_{GK} is finite in the thermodynamic limit, which is akin to a normal 'diffusive' system. However, the fluctuations do not decrease on averaging over ϕ, and may indicate deviation from normal diffusive transport.

To investigate the nature of transport at the critical point more closely, we now look at the scaling of $P(x,t)$. This is shown in Fig. 4.3 for various choices of b. It is clear that although $m_2(t) \sim t$, $P(x,t)$ is non-Gaussian, and does not obey a single scaling form. The bulk of $P(x,t)$ has the scaling form of Eq. 4.7, with $\tilde{\beta} = 0.5$ for all choices of b. However, the tails of $P(x,t)$ do not collapse under the same scaling. This deviation from bulk scaling is most clearly seen for $b = \sqrt{2}-1$. To collapse the tails of $P(x,t)$, one needs

a super-diffusive scaling. Thus we find

$$P(x,t) = \begin{cases} \left(1/\sqrt{t}\right) f_1(x/\sqrt{t}) & \forall \mid x \mid \le z_0\sqrt{t} \\ \left(1/t^{\tilde{\beta}_2}\right) f_2(x/t^{\tilde{\beta}_2}), & \tilde{\beta}_2 > 0.5 \quad \forall \mid x \mid > z_0\sqrt{t} \end{cases} \tag{4.21}$$

where z_0 and $\tilde{\beta}_2$ depend on the choice of b. Note that z_0 is independent of time. The super-diffusive scaling exponent $\tilde{\beta}_2$ is non-universal and depends on the choice of b. For $b = (\sqrt{5}-1)/2$ and for $b = 532/738$, $\tilde{\beta}_2 \sim 0.55$, for $b = \sqrt{2}-1$, $\tilde{\beta}_2 \sim 0.62$.

Note that for $b = (\sqrt{5}-1)/2$ and $b = 532/738$, from Fig. 4.3(b) it may seem that the super-diffusive scaling of $P(x,t)$ holds everywhere. This is because the super-diffusive exponent 0.55 is quite close to 0.5. However, a closer inspection reveals that this is not the case, and the bulk indeed has a diffusive-like scaling. This is clear from the fact that in all cases $m_2(t)$ in Fig. 4.3(c) shows the diffusive behavior, $m_2(t) \sim t$, and not the super-diffusive behavior. Also note that, for $b = \sqrt{2}-1$, $m_2(t) \sim 1.15t \simeq 4m_2^{nn}(t)$, consistent with Eq. 4.15.

Now, let us see if the behavior of tails of $P(x,t)$ can affect the scaling of the moments at extremely long times. To check this, we write $m_{2p}(t)$ as

$$m_{2p}(t) = 2\sum_{x=0}^{x \le z_0\sqrt{t}} x^{2p}P(x,t) + 2\sum_{x > z_0\sqrt{t}}^{\infty} x^{2p}P(x,t)$$

$$\simeq 2\int_0^{z_0\sqrt{t}} x^{2p}P(x,t)dx + 2\int_{z_0\sqrt{t}}^{\infty} x^{2p}P(x,t)dx$$

$$\equiv m_{2p}^{(1)}(t) + m_{2p}^{(2)}(t) \tag{4.22}$$

where $m_{2p}^{(1)}(t)$ is the contribution to moment from the diffusive part, while $m_{2p}^{(2)}(t)$ is the contribution to moment from the tails. Here we have used the fact that $\langle x \rangle = 0$, and $P(x,t)$ is an even function of x. Now, changing variables to $z_1 = x/\sqrt{t}$ and $z_2 = x/t^{\tilde{\beta}_2}$, and using Eq. 4.21, we have

$$m_{2p}(t) \simeq 2t^p \int_0^{z_0} z_1^{2p} f_1(z_1)dz_1 + 2t^{2p\tilde{\beta}_2} \int_{z_0\sqrt{t}/t^{\tilde{\beta}_2}}^{\infty} z_2^{2p} f_2(z_2)dz_2$$

$$= 2t^{2p\tilde{\beta}_2} \left(t^{p(1-2\tilde{\beta}_2)} A_p + F_p(z_0 t^{0.5(1-2\tilde{\beta}_2)}) \right) \tag{4.23}$$

where $A_p = \int_0^{z_0} z_1^{2p} f_1(z_1)dz_1$ and $F_p(\tau) = \int_\tau^{\infty} z_2^{2p} f_2(z_2)dz_2$. Note that A_p is independent of time while F_p is a function of time. So $m_{2p}^{(1)}(t) \sim t^p$, whereas $m_{2p}^{(2)}(t) \sim t^{2p\tilde{\beta}_2}$ only asymptotically. Since $\tilde{\beta}_2 > 0.5$, we have,

$$m_{2p}(t) \sim 2t^{2p\tilde{\beta}_2} F_p(0), \quad t \to \infty. \tag{4.24}$$
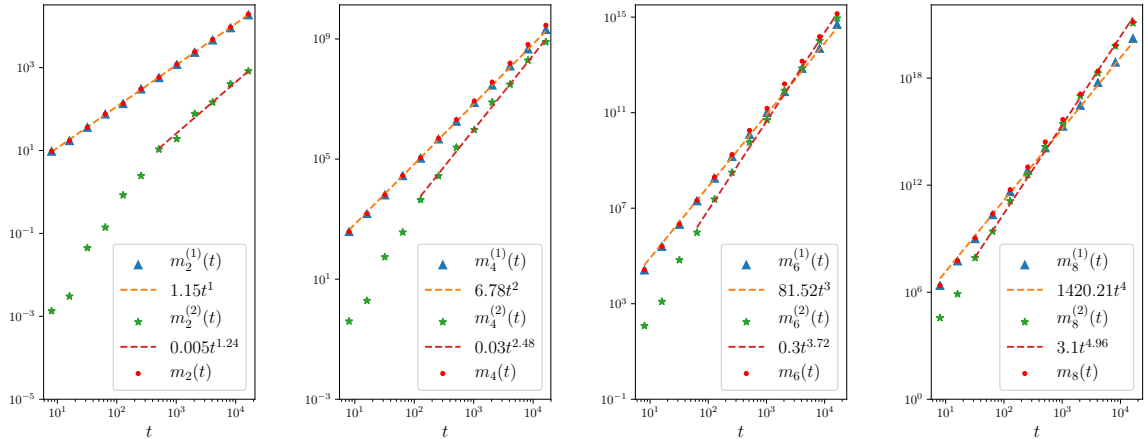
Figure 4.4: **Isolated thermodynamic limit**: *Plots of $m_{2p}^{(1)}(t)$, $m_{2p}^{(2)}(t)$ and $m_{2p}(t)$ (see Eq. 4.22) with time for $b = \sqrt{2} - 1$. $z_0 = 5$. The dashed lines are fits for $m_{2p}^{(1)}(t)$ and $m_{2p}^{(2)}(t)$. $m_{2p}^{(1)}(t) \sim t^p$, whereas, $m_{2p}^{(2)}(t) \sim t^{0.61p}$ for large t, as expected from tail scaling of $P(x,t)$. The crossover of m_{2p} scaling from diffusive to super-diffusive is seen clearly for $m_8(t)$ and $m_6(t)$. From the scaling fits, we see that for $m_2(t)$ this crossover will occur for time $t \gg 10^{10}$. $N = 8192$.*

Thus, the extreme long time behavior of the moments should be super-diffusive. Hence, there will be a crossover in time scaling of moments from diffusive to super-diffusive. The approach to the super-diffusive scaling is faster for higher moments. Let us check this quantitatively for $b = \sqrt{2} - 1$, which is the case where $\tilde{\beta}_2 \sim 0.62$ differs most significantly from the value 0.5. The value of z_0 can be read off from Fig. 4.3 as $z_0 \sim 6$. Fig. 4.4 shows the plots of $m_{2p}(t)$, $m_{2p}^{(1)}(t)$, $m_{2p}^{(2)}(t)$ for $p = 1, 2, 3, 4$. The first thing to note is that the approach to the form $m_{2p}^{(2)}(t) \sim t^{2p\tilde{\beta}_2}$ is faster for higher moments. Secondly, as expected, the crossover to super-diffusive scaling of $m_{2p}(t)$ also occurs faster for higher moments. For $m_8(t)$ and $m_6(t)$, this crossover is clearly seen from our data. On the other hand, for $m_4(t)$ and $m_2(t)$, the crossover occurs later than times accessible in our numerics. From the scaling-fits, it is possible to quantitatively extract the time scales at which the super-diffusive crossover will be seen in the $m_2(t)$ scaling. We find that the super-diffusive scaling of $m_2(t)$ will start showing for $t \gg t^* \sim 10^{10}$. To directly investigate such long time behavior without having finite-size effects, one needs systems of size $N \gg (t^*)^{0.62} \sim 10^7$. Exact numerical analysis of such system sizes is definitely beyond our current computational power. This explains the normal-diffusive-like behavior of Green-Kubo conductivity up to times and system-sizes within our numerical reach, and suggests that at even longer times, the super-diffusive behavior will show up.
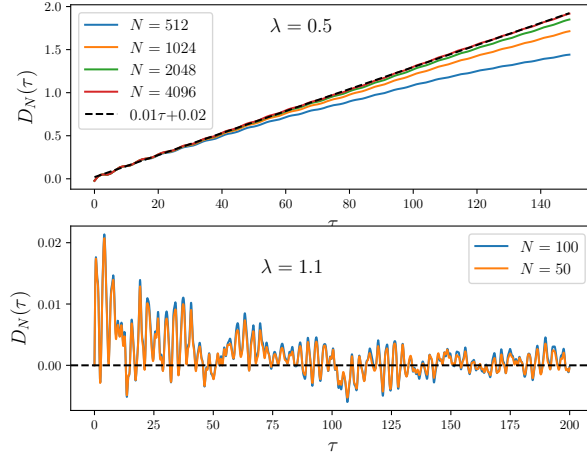
Figure 4.5: **Isolated thermodynamic limit**: *Plot showing $D_N(\tau)$ as a function of τ for delocalized (top panel) and localized (bottom panel) cases for different system sizes. For delocalized case, $D_N(\tau)$ increases linearly with τ before finite size effects come into play. For localized case, $D_N(\tau)$ decays to zero and is independent of N for $N \gg$ localization length$= 1/\log(\lambda) \simeq 10$. Parameters: $\beta = 0.1$, $\mu = 1.$, $b = \sqrt{2} - 1$.*

Therefore, we find *hints of super-diffusive behavior at the critical point of the AAH model in the isolated thermodynamic limit* from the tail scaling of $P(x, t)$ and the time scaling of higher moments of $P(x, t)$. However direct numerical observation of this super-diffusive behavior from $m_2(t)$ scaling or from Green-Kubo conductivity is beyond our current numerical reach. Within our numerical reach, $m_2(t)$ scales diffusively, and Green-Kubo conductivity also shows normal-diffusive-like behavior.

Away from the critical point, the behavior is exactly as expected. Plots of $D_N(\tau)$ for delocalized and localized regimes are shown in Fig. 4.5 for $b = \sqrt{2} - 1$. In the delocalized regime ($\lambda < 1$), $D_N(\tau)$ increases linearly with τ before finite-size effects become significant. Finite size effects start showing after times of $O(N)$. Thus, to numerically take the correct limit (in Eq. 4.10) for a given system size N one needs to look at $\tau \sim N$. This correctly gives the ballistic conductivity scaling with system size, $\sigma \sim N$. It is also trivial to check $m_2(t) \sim t^2$. In the localized regime ($\lambda < 1$), for system sizes much greater than the localization length (given by $1/\log(\lambda)$ [95]), the thermodynamic limit is reached and $D_N(\tau)$ becomes independent of N. We see $D_N(\tau)$ decays to zero as a function of τ for such cases, thus giving zero conductivity. Obviously, because all eigenstates are localized, $m_2(t) \sim t^0$ consistently. We will show below that, when the system is connected to baths, the transport behavior at the critical point of AAH model completely changes.
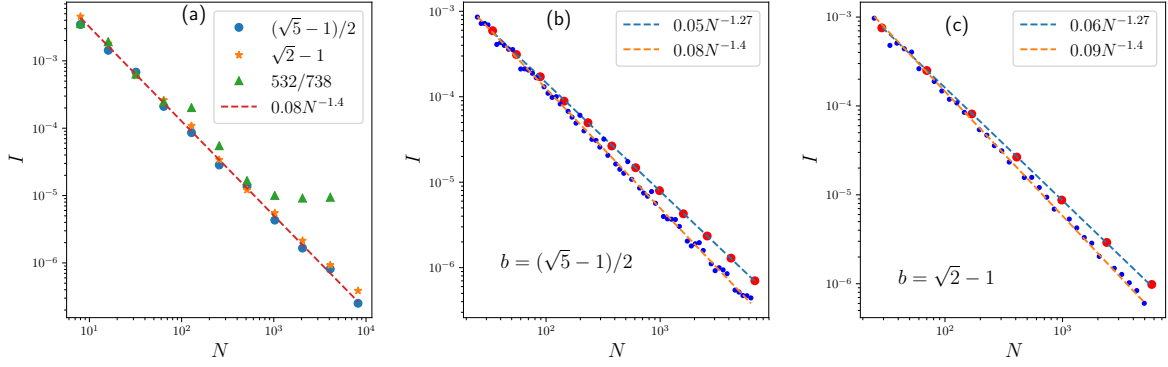
Figure 4.6: **Open system**: *(a) Scaling of current I with system size N for various values of b. $I \sim N^{-1.4 \pm 0.05}$. For $b = 532/738$, current scaling shows ballistic behavior, $I \sim N^0$ for $N \gg 738$, as expected. Here the system sizes taken are powers of 2. (b) Scaling of current with system size for $b = (\sqrt{5} - 1)/2$ with much closely taken points. This reveals that $I \sim N^{-1.27 \pm 0.01}$ for $N =$ Fibonacci numbers (red circles), whereas $I \sim N^{-1.4 \pm 0.05}$ for system sizes away from Fibonacci numbers. (c) Scaling of current with system size for $b = \sqrt{2} - 1$ with much closely taken points. This reveals that $I \sim N^{-1.27 \pm 0.01}$ for $N =$ Pell numbers (red circles), whereas $I \sim N^{-1.4 \pm 0.05}$ for system sizes away from Pell numbers. Parameters : $\beta = 0.1, \mu_1 = 3, \mu_2 = -3, \gamma = 1, t_B = 3$.*

Open system

Current scaling with system size   We explore current with system-size using the set-up shown in Fig. 4.1. Current is calculated by numerical evaluation of the exact result in Eq. 4.19. The current scaling with system size in the open system at the critical point for various choices of b is shown in Fig. 4.6(a). Here system sizes were taken as powers of 2. It is immediately clear that the scaling is sub-diffusive with $I \sim N^{-1.4 \pm 0.05}$. It is also interesting to note that for $b = 532/738$ the current becomes independent of N for $N \gtrsim 738$, which is the signature of the delocalized phase. This is consistent with our previous discussion that $532/738$ remains 'effectively irrational' only for $N \lesssim 738$.

In Fig. 4.6(b), (c), we investigate the current scaling with system size more closely for golden mean and silver mean cases. We see that for golden (silver) mean, the current scaling with system size is different for system sizes equal to Fibonacci (Pell) numbers, where $I \sim N^{-1.27 \pm 0.01}$. Away from these special system sizes, the current scaling is approximately $I \sim N^{-1.4 \pm 0.05}$. An interesting observation follows from noting that any irrational number has an infinite continued fraction representation which, on truncation, gives a rational approximation of the irrational number. We conjecture that at special

system sizes equal to the denominators of the rational approximations, the current deviates from the generic behaviour and has a different scaling. These special system sizes are the Fibonacci (Pell) numbers for the golden (silver) mean.

The current scaling with system size at the critical point for various choices of b is shown in Fig. 4.6(a). Here system sizes were taken as powers of 2. It is immediately clear that the scaling is sub-diffusive with $I \sim N^{-1.4 \pm 0.05}$. It is also interesting to note that for $b = 532/738$ the current becomes independent of N for $N \gtrsim 738$, which is the signature of the delocalized phase. This is consistent with our previous discussion that $532/738$ remains 'effectively irrational' only for $N \lesssim 738$.

In Fig. 4.6(b), (c), we investigate the current scaling with system size more closely for golden mean and silver mean cases. We see that for golden (silver) mean, the current scaling with system size is different for system sizes equal to Fibonacci (Pell) numbers, where $I \sim N^{-1.27 \pm 0.01}$. Away from these special system sizes, the current scaling is approximately $I \sim N^{-1.4 \pm 0.05}$. An interesting observation follows from noting that any irrational number has an infinite continued fraction representation which, on truncation, gives a rational approximation of the irrational number. We conjecture that at special system sizes equal to the denominators of the rational approximations, the current deviates from the generic behaviour and has a different scaling. These special system sizes are the Fibonacci (Pell) numbers for the golden (silver) mean.

Thus, we see that the *transport in the open critical AAH model is sub-diffusive*. This is drastically different from what we found in the isolated thermodynamic limit, where we found hints of super-diffusive behavior. We now investigate the origin of the sub-diffusive behavior. To do this, we first take the $t_B \to$ large limit, so that, the system-bath coupling becomes weak and the bath spectral functions become almost constant (see Eq. 4.18). (Note that in Fig. 4.6, the system-bath coupling was not weak.) In this regime, a simplified expression for conductance can be obtained using the techniques discussed in subsection. 2.3.1. The derivation is given in Appendix. 6.4. The result is

$$G \simeq \frac{\Gamma \beta}{4} W(1, N), \quad \beta \to \text{small}, \ t_B \to \text{large}$$

$$W(p, q) = \sum_{\alpha=1}^{N} \frac{\Phi_{p\alpha}^2 \Phi_{q\alpha}^2}{\Phi_{p\alpha}^2 + \Phi_{q\alpha}^2} \tag{4.25}$$

where $\Gamma = (2\gamma^2)/t_B$ and we have also taken the small β limit so that $n_F(\omega) \simeq 1/2$. Thus, the system-size scaling of G in this limit is given by the system size scaling of $W(1, N)$. Note that by Eq. 6.44, and under the same assumptions as in Eq. 4.25, $W(p, q)$
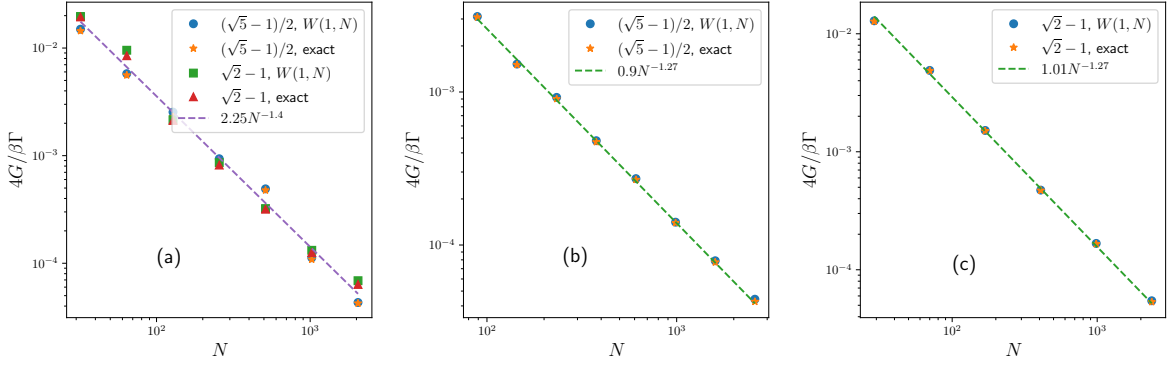
Figure 4.7: **Open system**: *(a) Scaling of conductance G with system size N for various values of b for weak system-bath coupling ($\gamma = 1$, $t_B = 200$) and very high temperature ($\beta = 0.01$). Exact numerical results are obtained via Eq. 4.19, and that is compared with approximate analytical result W (see Eq. 4.25). There is near perfect overlap of exact results with W, and $G \sim N^{-1.4\pm0.05}$. Here the system sizes taken are powers of 2. (b), (c) The different scaling of G with system size equal to Fibonacci and Pell numbers for golden mean and silver mean cases, $G \sim N^{-1.27\pm0.01}$.*

corresponds to conductance of the case when the baths are attached at the pth and qth sites. If the system size scaling of G in this limit is similar to that in Fig. 4.6, which is not guaranteed a priori, we will know that the sub-diffusive scaling is because of the system size scaling of $W(1, N)$.

The system size scaling of conductance calculated in this limit ($\gamma = 1, t_B = 200, \beta = 0.01$) by exact numerical integration, Eq. 4.19, and by Eq. 4.25 is given in Fig. 4.7. There is near perfect overlap of the two results. Note that exact numerical calculation using Eq. 4.19 is more difficult in this regime, because of the nearly singular behavior of the integrand at system eigenenergies. In Fig. 4.7(a), the scaling is shown for system-sizes in powers of 2. The scaling is not as good as that seen in the strong system-bath coupling case, but it is approximately the same, $G \sim N^{-1.4\pm0.05}$. Fig. 4.7(b) (Fig. 4.7(c)) shows the scaling for golden (silver) mean case when system sizes are equal to Fibonacci (Pell) numbers. Here there is an almost perfect scaling of $G \sim N^{-1.27\pm0.01}$ as before. Thus, indeed, the sub-diffusive scaling of current and conductance with system-size is directly related to the sub-diffusive scaling of $W(1, N)$ with system-size.

Note that, for $\lambda < 1$, the single particle eigenfunctions are completely delocalized, hence $\Phi_{\alpha,\ell}^2 \sim N^{-1}$. Thus $W(1, N) \sim N^0$, thereby giving the ballistic scaling of current consistently. On the other hand, for $\lambda > 1$, the single particle eigenfunctions are expo-

nentially localized at some system site, so, $\Phi_{\alpha,1}^2 \sim \Phi_{\alpha,N}^2 \sim e^{-N}$. Thus, $W(1,N) \sim e^{-N}$, thereby giving the exponential decay of current with system-size in this regime also consistently. Thus, the system size scaling of $W(1,N)$ correctly gives the system-size scaling of currents at all regimes of the AAH model. This also shows that the current scaling with system size is independent of the details of the baths, and also independent of the type of particles (bosonic or fermionic).

Hence, the transport behavior of open AAH model is totally governed by the single particle eigenfunctions at the boundaries where the baths are attached. In the isolated thermodynamic limit, there are no boundaries, and the transport behavior is governed by the bulk properties. Looking at Eq. 4.4, 4.11, 4.14, and Eq. 4.25, we see that there is no reason a priori that the isolated thermodynamic limit transport characterized by spread of a wavepacket, and the open system transport characterized by current scaling with system size, need to be consistent with each other in general. It nonetheless turns out that in the delocalized and the localized cases, they can indeed be shown to be consistent. The underlying reason for this is that, for these cases, the eigenstates contributing to transport have similar behavior in the bulk and at the boundaries. But, at the critical point, the eigenstates contributing to transport have different behavior at the bulk and at the boundaries. To clearly see this, in Fig. 4.8 we check the system size scaling of $W(N/4, 3N/4)$ for all three phases and compare them with that of $W(1,N)$. Unlike $W(1,N)$, $W(N/4, 3N/4)$ depends on the bulk behavior of eigenstates. As discussed before, $W(N/4, 3N/4)$ gives conductance for the case where the baths are attached at the $N/4$th and $3N/4$th sites. We see that at the critical point, $W(N/4, 3N/4)$ scales very differently from $W(1,N)$, i.e., $W(N/4, 3N/4) \sim N^{-0.27\pm0.03}$ whereas $W(1,N) \sim N^{-1.4\pm0.05}$. Away from the critical point, $W(N/4, 3N/4)$ and $W(1,N)$ have same scaling with system size,i.e., they are independent of N for $\lambda < 1$ and decay exponentially with N for $\lambda > 1$. Thus, indeed, the eigenstates contributing to transport have different behavior in the bulk and at the boundaries only at the critical point. This leads to drastically different transport behavior in the isolated and in the open critical AAH model. We note that differences between bulk and boundary behaviour of eigenstates have been previously observed in disordered systems and have been attributed to the multifractal nature of the eigenfunctions [102]. But they have not been directly connected to transport properties.

NESS particle density profile Next, we look at the spatial particle density profile, $\langle \hat{n}_r \rangle$ vs r, in NESS in each of delocalized, critical and localized regimes when the two
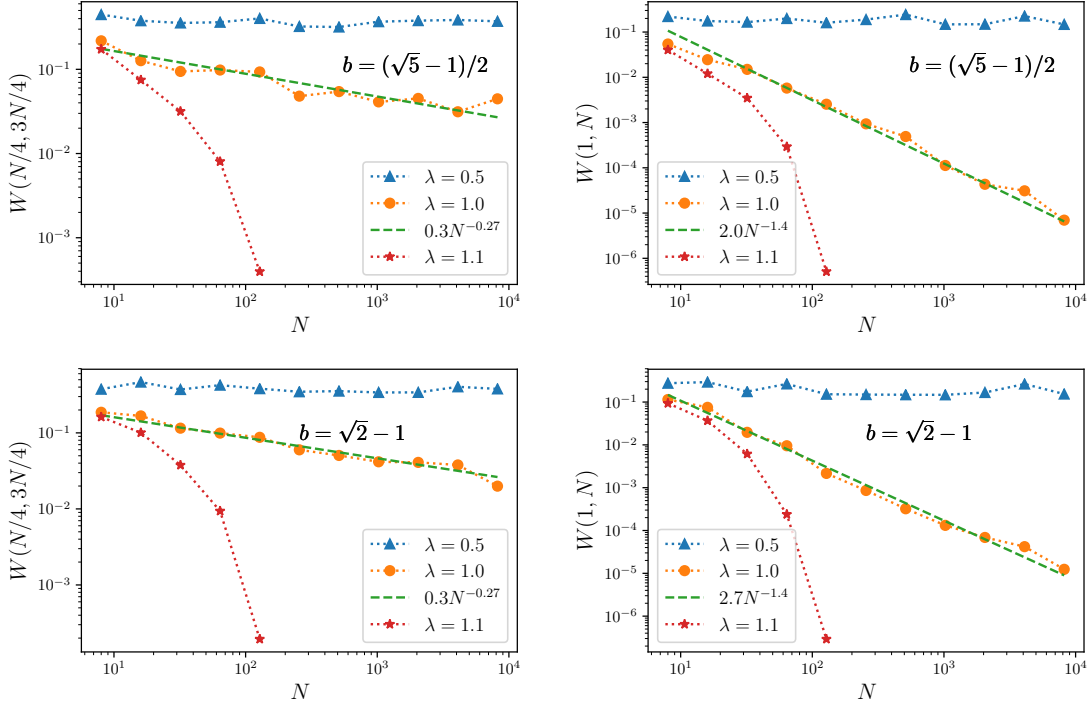
Figure 4.8:   *System size scaling of $W(N/4, 3N/4)$ (left panel) compared with that of $W(1, N)$ (right panel) at all three phases. $W(N/4, 3N/4)$ and $W(1, N)$ scale similarly with N away from the critical point: they are independent of N for $\lambda < 1$ and decay exponentially with N for $\lambda > 1$. At critical point, $\lambda = 1$, $W(N/4, 3N/4)$ and $W(1, N)$ show power-law decay with system size with very different exponents: $W(N/4, 3N/4) \sim N^{-0.27\pm0.03}$ whereas $W(1, N) \sim N^{-1.4\pm0.05}$. System sizes taken here are in powers of 2.*

Figure 4.9: **Open system**: *NESS particle density profile for the three regimes : delocalised ($\lambda = 0.5 < 1$), critical ($\lambda = 1$), localized ($\lambda = 1.1 > 1$) for various system sizes. The particle density profile looks distinctly different in the three regimes. Parameters : $\beta = 0.1$, $\mu_1 = 6, \mu_2 = -6$, $\gamma = 1$, $t_B = 3$, $b = (\sqrt{5} - 1)/2$.*
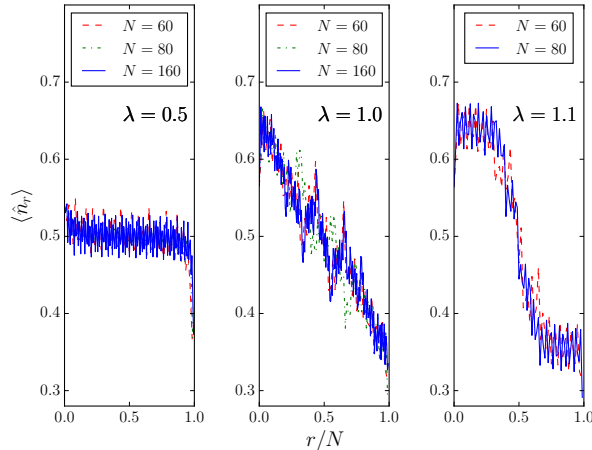
baths are at widely different chemical potentials. We find that the NESS spatial particle density profile (which is related to local chemical potential) behaves very differently in the three regimes (Fig. 4.9). In the de-localized regime, we notice a flat profile, a hallmark of ballistic transport. In the critical regime, we see a continuous (almost linear) curve connecting the boundary densities. Such behaviour is typical of diffusive systems. The localized regime shows a step-like profile and this has recently been reported for other models with localization [103, 104]. Hence, this NESS physical quantity, which is potentially measurable with recent cutting-edge experiments [82, 83, 84, 85, 89], gives a clear real-space signature of localized, critical and delocalized phases. The energy profile (which is related to local temperature) has a similar behaviour.

Summary

We have investigated the high temperature transport properties of the AAH model both in the isolated thermodynamic limit, and in the open system. We have found that the critical point of the AAH model has drastically different transport behavior in the two cases. In the isolated thermodynamic limit, spread of an initially localized wavepacket shows hints of super-diffusive behavior. The super-diffusive scaling exponent is non-universal and depends of the choice of the irrational number b. On the other hand, the open system NESS current I scaling with system size N is clearly sub-diffusive. There are two sub-

diffusive exponents. One is $I \sim N^{-1.27 \pm 0.01}$, which is seen when system sizes are exactly the denominators of the rational approximants of b, while the other is $I \sim N^{-1.4 \pm 0.05}$, which is the scaling for generic system sizes. We have shown that the current scaling with system size is entirely controlled by the system size scaling of eigenfunctions at the boundaries where the baths are attached. Thus, the drastic difference between the isolated and the open system transport properties at the critical point is due to different behaviors of the eigenfunctions at the bulk and at the boundaries.

We would like to point out that looking at the spread of correlations and measuring the current or conductance variation with system size are two different experiments done to characterize transport in many set-ups. Although not guaranteed, in many cases, the results of one experiment can be inferred from that of the other. We showed that at the critical point of the AAH model, this is not possible.

We have also looked that the NESS particle density profile of the open system connected to two baths at different chemical potentials. We have shown the the NESS particle density profile is distinctly different in the delocalized, critical and localized phases.

Thus, we have looked into transport properties of the AAH model in detail. The AAH model does not have a mobility edge. Next we will look into transport properties of a model with a mobility edge.

4.2.2   Transport in a model with a single-particle mobility edge

Even though the AAH model has no mobility edge, various generalizations of it, as well as other quasiperiodic systems, have been shown to have mobility edges in one dimension. Recently, physics of such systems have attracted a lot of attention [105, 106, 107, 108, 109, 110, 111, 112, 113, 114, 115, 116, 117] and has also been experimentally realized [118]. We now focus on one such model that has been recently proposed [105, 106, 107, 108, 109]. This model has a mobility edge, with the additional property that the mobility edge is a self-dual point under a similar transformation as in the conventional AAH model. Henceforth, we call this model the generalized Aubry-André-Harper (GAAH) model.

Although the phase diagram of AAH model is well-known, the phase diagram of GAAH model has not been studied. In general, non-equilibrium phase transitions have received a lot of limelight recently, appear in various contexts [119, 120, 121, 122]. Our main objective in this section is to map out the high temperature non-equilibrium phase diagram of the GAAH model evidenced by open system transport properties.

The model

The generalized AAH model (GAAH) is given by the Hamiltonian

$$\mathcal{H}_S = \sum_{r=1}^{N-1}(\hat{a}_r^\dagger \hat{a}_{r+1} + h.c) + \sum_{r=1}^{N} \frac{2\lambda \cos(2\pi b r + \phi)}{1 - \alpha \cos(2\pi b r + \phi)} \hat{a}_r^\dagger \hat{a}_r, \qquad (4.26)$$

and $\{\hat{a}_r\}$ are fermionic (bosonic) annihilation operators, λ is the strength of the onsite potential, ϕ a phase factor, b is a an irrational number and the parameter $\alpha \in (-1, 1)$. For our analysis, we will restrict ourselves to $\alpha, \lambda > 0$. Other regions can be reconstructed via symmetries in the Hamiltonian. The symmetries can be concisely written as $\mathcal{H}_S(\lambda, \alpha, \phi) = \mathcal{H}_S(-\lambda, -\alpha, \phi + \pi) = -\tilde{\mathcal{H}}_S(-\lambda, \alpha, \phi) = -\tilde{\mathcal{H}}_S(\lambda, -\alpha, \phi + \pi)$, where $\tilde{\mathcal{H}}_S$ is the Hamiltonian obtained after the transformation $\hat{a}_r \rightarrow (-1)^r \hat{a}_r$. For $\alpha = 0$, we get the AAH model, where it is known that $\lambda = 1$ is a critical point exhibiting self-duality. Similarly it is known that for any choice of b and ϕ, the GAAH model shows self-duality at an energy E satisfying the condition $\alpha E = 2\,\mathrm{sgn}(\lambda)(1 - | \lambda |)$, provided E is a single-particle energy eigenvalue. All energy eigenstates with energy less than E are extended while those higher than E are localized. If E falls within the spectrum, then it is a mobility edge. In this paper, we investigate the phase diagram of this system in the α-λ plane. We choose $b = (\sqrt{5} - 1)/2$, which is the golden mean, and, unless otherwise mentioned, all our results are obtained after averaging over ϕ.

Hints of rich phase diagram

The first hint of a rich phase diagram of this model comes from direct calculation of the fraction of localized states in the system. It can be checked via calculation of inverse participation ratio (IPR) that, for $\lambda, \alpha > 0$, the states with energy greater than the self-dual point are localized. Thus, the fraction of localized states is given by the fraction of single particle eigenstates with energy greater than the self-dual point. This is shown in Fig. 4.10(a). We immediately see several regions of different colors (indicating different fraction of localized states) with clear boundaries. Two of the most clear boundaries are shown by the dotted and dashed lines. Below the dotted line, there is no mobility edge and all states are delocalized. This line corresponds to the case where the self-dual point exactly coincides with the highest energy eigenstate of the system. Below the dashed line, there is no mobility edge and all states are localized. This line corresponds to the case where the self-dual point exactly coincides with the lowest energy eigenstate of the system. As we will see below, this is actually a 'critical' line in the non-equilibrium phase
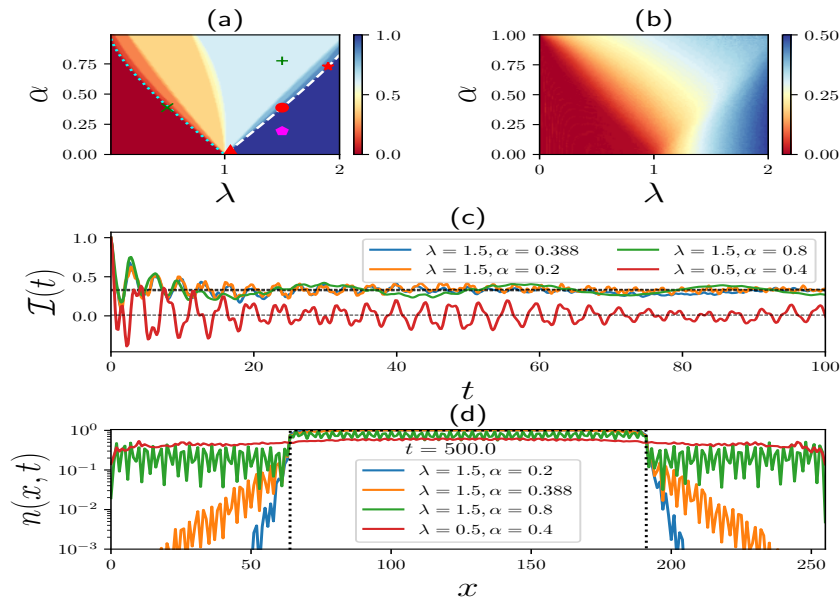
Figure 4.10: **(a)** *Fraction of localized eigenstates (color coded) as a function of α and λ. A possible 'phase diagram' with phase transitions and crossovers is evident. The marked points are considered for further analysis.* **(b)** *The long time value of imbalance $\mathcal{I}$ (color coded) as a function of α and λ maps out a 'phase diagram' quite similar to that in (a).* **(c)** *Behavior of $\mathcal{I}$ with time for some chosen points. (d) A long time snap-shot result of an initially localized profile (shown with the dotted line) for various values of λ and α. Parameters : $N = 1024$ for **(a)**, $N = 256$ for **(b)**, **(c)** and **(d)**.*

diagram. Henceforth, we will call this line the 'critical' line of GAAH model. Note that since the minimum energy eigenvalue depends on the choice of irrational number, the 'critical' line of GAAH model is not independent of choice of irrational number.

Next, we check if a physically measurable quantity can reproduce all the regions shown by the fraction of localized states. To this end, we calculate the population imbalance. This is defined by $\mathcal{I}(t) = \frac{\langle N_e(t) - N_o(t)\rangle_0}{\langle N_e(t) + N_o(t)\rangle_0} = \frac{2}{N}\sum_r (-1)^r \langle \hat{n}_r(t)\rangle_0$, where N_e and N_o are the number of particles at the even and odd sites respectively and $\langle...\rangle_0$ denotes expectation value over the initial state. The initial state is chosen so that only the even sites are occupied. This quantity has been recently experimentally measured for the regular AAH model [82, 83, 84]. $\mathcal{I}(t)$ tends to a steady value in the long time limit (Fig. 4.10(c)). This value depends monotonically on the number of localized states. Hence variation of long time value of $\mathcal{I}(t)$ with α and λ, should be similar to the fraction of localized states plot. This is exactly what we find in Fig. 4.10(b) which shows the long time value of $\mathcal{I}(t)$ (color coded) as a function of α and λ. However, the 'critical' line is not well captured via $\mathcal{I}(t)$. This is because on this line there are still a large number of localized states. While imbalance captures the presence of localized states, it cannot directly capture the effect of having a mobility edge. This is nicely captured by evolution of an initially localized step particle density profile [123] (Fig. 4.10(d)). Delocalized states cause the initially localized profile to spread out with time, while localized states almost do not evolve the initial profile. In presence of a mobility edge, there is a coexistence of both kinds of behaviors due to presence of both localized and delocalized states. This has recently been seen in experiment [118].

The GAAH-AAH model eigenfunction correspondence

When there is a state at the mobility edge, it is a self-dual point. However this does not say anything about the nature of energy eigenstates at or very close to the self-dual point. To check the nature of these states, we plot the eigenfunctions of the GAAH model near the self-dual point. Let the eigenstates be ordered in ascending order of energy. Then, quite surprisingly, we find that, if the νth state of GAAH model is near the self-dual point, then its eigenfunction almost exactly overlap with the νth state of the critical AAH model ($\alpha = 0$, $\lambda = 1$). This remarkable result immediately establishes that states near the self-dual point have a 'critical' nature. This phenomenon is observed not only on the 'critical' line, but anywhere in the α, λ plane where there are eigenstates close
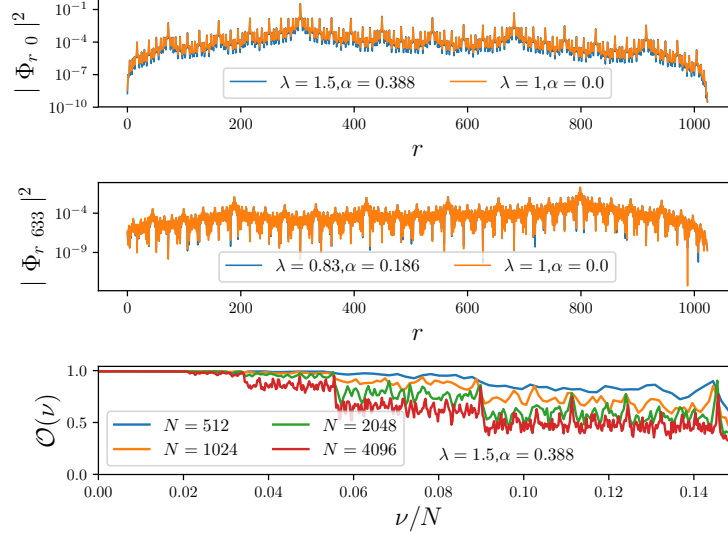
Figure 4.11: *Top two panels: The figure demonstrates a remarkable matching of single particle wavefunctions $\Phi_{r\nu}$ of the GAAH model near the self-dual point with those of critical AAH model ($\alpha = 0$, $\lambda = 1$). Bottom panel: Overlap 'integral' of wavefunctions of GAAH and AAH models as function of eigenstate index for several system sizes. Here ν is the eigenstate index and r is the site index. Parametes: Top two panels: $N = 1024$, $\phi = 0$. Bottom panel is averaged over ϕ.*

to the self-dual point (Fig. 4.11). To quantify this, we calculate the overlap 'integral' of the GAAH model and AAH model wavefunctions as a function of eigenstate index ν, $\mathcal{O}(\nu) = | \sum_{r=1}^{N} \Phi_{r\nu}^{GAAH} \Phi_{r\nu}^{AAH} |$, where $\Phi_{r\nu}^{GAAH}$ is the weight of the νth eigenfunction of the GAAH model at site r and $\Phi_{r\nu}^{GAAH}$ is the corresponding one for the critical AAH model. This is shown in Fig. 4.11 bottom panel for parameters on the 'critical' line. Close to the minimum eigenvalue there is near complete overlap ($> 99\%$). The plot also shows that, for a given system size, there is a finite fraction of such 'critical' states, and the fraction of such states goes down with increase in system size. Note that although it has been previously shown that eigenfunctions of GAAH model near self-dual point and those of critical AAH model have same IPR scaling exponents [106], that does not say anything about the spatial overlap of eigenfunctions. For example, two eigenstates of the critical AAH model have the same IPR scaling exponents but have zero overlap due to orthogonality. On the other hand, knowing that two states are overlapping automatically establishes them to have same scaling exponents. In this sense, the overlap we observe here, is a more direct and much stronger statement about the GAAH-AAH model eigenfunction correspondence.
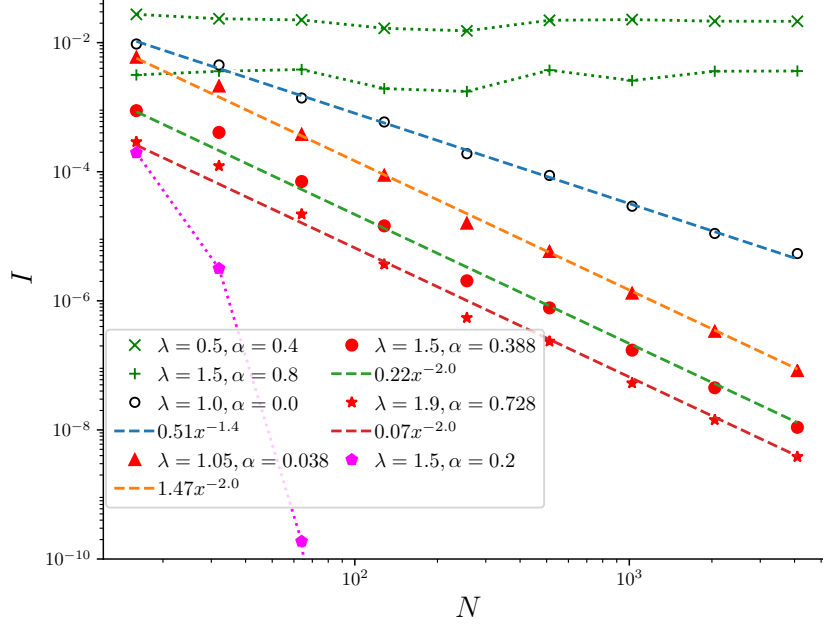
Figure 4.12: *The scaling of current with system size for various parameters of the GAAH model. On the 'critical' line of the GAAH model, current scales as $I \sim N^{-2\pm0.1}$ showing sub-diffusive behaviour (red markers). In contrast, the critical AAH model ($\lambda = 1.0, \alpha = 0.0$) data shows $I \sim N^{-1.4\pm0.05}$ (white circles). For parameters where some states are delocalized, transport is ballistic, $I \sim N^0$ (green markers). When all states are localized, current decays exponentially, $I \sim e^{-N}$ (magenta markers). The points chosen in above plot correspond to the points in Fig. 4.10(a) having the same symbol and color. The dashed lines are power law fits, whereas, the dotted lines are guide-to-eye. Parameters : $\mu_1 = 50, \mu_2 = -50, \beta = 0.1, t_B = 25, \gamma_1 = \gamma_2 = 3$.*

The high temperature non-equilibrium phase diagram

On the 'critical' line of GAAH model, there are no truly delocalized states, but critical and localized states. Hence, contribution to transport properties should primarily come from these critical states. Since the wavefunctions of these states almost exactly overlap with critical AAH model, one can expect the transport properties on the 'critical' line to be similar to that of the critical AAH model. We explore the transport behavior of GAAH model via scaling of current with system-size using the set-up shown in Fig. 4.1.

The variation of current with system-size gives the nature of transport. The following two results are obvious: for parameters in the all-states-delocalized regime, the transport is ballistic and current is independent of system size ($I \sim N^0$) while for parameters in the all-states-localized regime, current decreases exponentially with system size ($I \sim e^{-N}$).
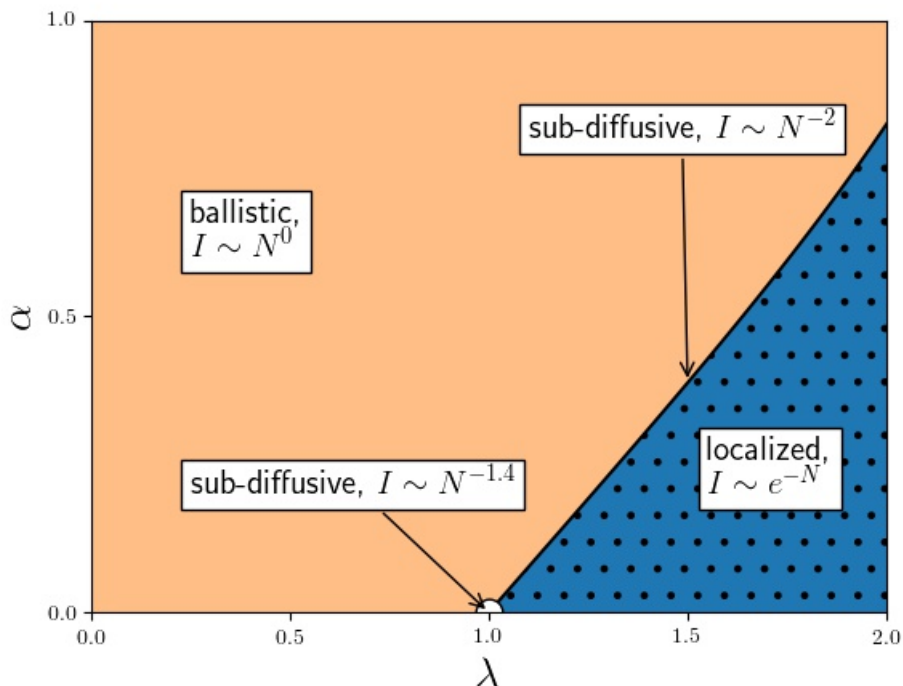
Figure 4.13: *Non-equilibrium phase diagram at high temperatures for the GAAH model obtained from system size scaling of NESS current. Here I is NESS current and N is the system size.*

The interesting question is current scaling with system size in presence of mobility edge. Fig. 4.12 shows current I as a function of system size for various values of α and λ. The most interesting finding is that, for parameters on the 'critical' line, the $I \sim N^{-2\pm0.1}$, thereby showing transport is sub-diffusive. However, this is different from the critical AAH model ($\alpha = 0$, $\lambda = 1$), where current scales as $I \sim N^{-1.4\pm0.05}$. For parameters where there are at least a few delocalized states, I is independent of system size, which is a signature of ballistic transport (Fig. 4.12, bottom panel). The above results are at relatively high temperature ($\beta = 0.1$). At such temperatures, for any choice of chemical potentials μ_1 and μ_2, the same result will be seen. Thus, the above results give us a clear non-equilibrium phase diagram of the GAAH model at high temperatures (Fig. 4.13).

To explain the difference in scaling exponent of I vs N between critical AAH model and 'critical' line of GAAH model, we look at the system size scaling of the coarse-grained transmission near the minimum eigenvalue. For this, we first choose an energy range of interest and divide it into uniform cells of width δE. On this coarse-grained energy axis, the coarse grained transmission $\overline{\mathcal{T}}(\omega)$ is given by $\overline{\mathcal{T}}(E) = \left[\int_{E-\delta E/2}^{E+\delta E/2} \mathcal{T}(\omega)d\omega \right] / \delta E$. We find
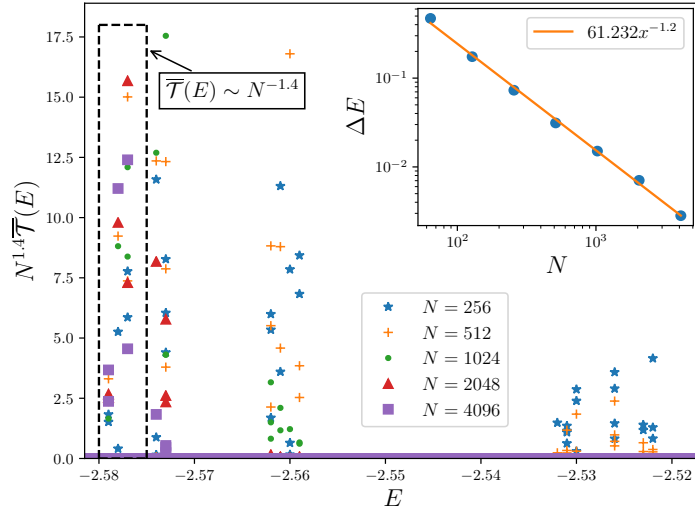
Figure 4.14: *Coarse-grained transmission $\overline{\mathcal{T}}(E)$ near the self-dual point (the minimum energy eigenvalue) for a choice of parameters ($\lambda = 1.5, \alpha = 0.388$) on the 'critical' line of GAAH model, scaled assuming similar scaling as critical AAH model. For larger system sizes, $\overline{\mathcal{T}}(E) \sim N^{-1.4\pm0.05}$ scaling holds over a smaller energy range. Inset: The plot of ΔE vs N. ΔE is the range of energy over which eigenstates of GAAH model that overlap more than 90% with those of critical AAH model. $\Delta E \sim N^{-1.2\pm0.03}$. Other parameters: $t_B = 25, \gamma_1 = \gamma_2 = 3, \delta E = 2 \times 10^{-4}$.*

that close to the minimum eigenvalue $\overline{\mathcal{T}}(E) \sim N^{-1.4\pm0.05}$, but the energy range upto which this scaling is seen decreases with increase in system size (Fig. 4.14 left panel). This energy range corresponds to the energy range where GAAH and critical AAH model wavefunctions overlap. Since current is obtained by integrating over the transmission (with appropriate Fermi distributions), this directly gives a hint as to the reason for different exponent. The transmission, and hence $\overline{\mathcal{T}}(\omega)$, has peaks near system energy eigenvalues. Thus, we can approximate the integral over transmission as $\int \mathcal{T}(\omega)d\omega = \sum \overline{\mathcal{T}}(E)\delta E \sim N^{-1.4\pm0.05}(\frac{\Delta E}{\delta E})^{d_f}$, where ΔE is the energy range where states of GAAH model overlap with critical AAH model, and d_f is the box-counting dimension of the spectrum over this energy range. $\Delta E \sim N^{-1.2\pm0.03}$ (Fig. 4.14 inset). It can be checked that $d_f \sim 0.5$, which is the same as that of critical AAH model [124]. Thus $\int \mathcal{T}(\omega)d\omega$, and hence the current I, scales as $\sim N^{-2\pm0.1}$.

Summary and outlook

Thus, we have mapped out the high temperature non-equilibrium phase diagram of the GAAH model, which is a model with single particle mobility edge. In doing so, we have found a fascinating correspondence between the GAAH model and the conventional AAH model which does not have a mobility edge. It follows from this correspondence that the critical point of AAH model now generalizes to a 'critical line' of GAAH model separating regions of ballistic and localized transport. However, the current scaling with system size on this 'critical line' has a different exponent from that of the critical AAH model. We have also explained this from the GAAH-AAH model correspondence.

The GAAH model is rather unexplored and several questions still remain. However, we will not delve into them further in this thesis. We will only mention some of the interesting directions for future research opened up by the above results. The exact reason behind the GAAH-AAH eigenfunction correspondence is not clear, and requires further work which will be of great interest in mathematical front. Moreover, we would like to point out that, unlike the critical point of AAH model, the 'critical' line of GAAH model depends on the choice of irrational number. The effect of other irrational numbers is also an interesting question. Also, as we have seen before, the critical AAH model has remarkably different transport behaviors in isolated and open system set-ups. Future work thus also involves, detailed investigation of isolated system transport, as well as, low temperature transport of GAAH model.

$$\beta + \frac{\Delta\beta}{2}, \mu + \frac{\Delta\mu}{2} \qquad\qquad \beta - \frac{\Delta\beta}{2}, \mu - \frac{\Delta\mu}{2}$$
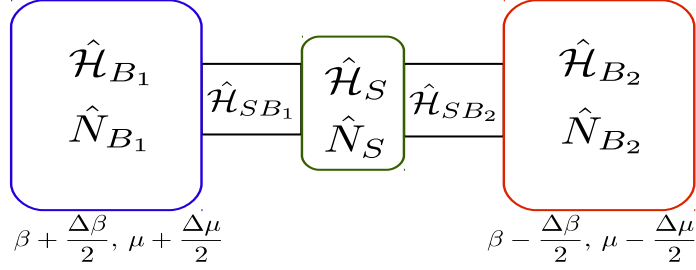
Figure 4.15: *The general set-up for obtaining open system current fluctuation-dissipation relations. $\hat{N}_S, \hat{N}_{B_1}, \hat{N}_{B_2}$ are operators corresponding to total number of particles in system, left bath and right bath. We look at linear response regime, i.e, when $\Delta\beta, \Delta\mu \to 0$, for absolutely general Hamiltonians having time-reversal and time-translation symmetries and showing open system thermalization.*

4.3 Open system current fluctuation-dissipation relations (OCFDR)

[This section closely follows discussions in the paper (vi), which is on arxiv.]

As we have seen, there are both isolated system and open system ways for classifying transport behaviors. It is can be expected that the open system and the isolated system transport properties are related. However, in the critical AAH model, we already saw that the open system and the isolated system characterizations may not give similar results. Mismatch between open system and isolated system transport behaviors has also been reported in [125, 126]. Both the open system (for example, [127, 128, 129, 130, 131, 132, 133, 134] and the isolated system (for example, [135, 136, 137, 138]) approaches are equally popularly used in literature to classify transport behaviors, but the essential rigorous connection between them is missing. Now we explore the connection between the two ways of classifying transport in detail. The key to this is to obtain fluctuation-dissipation relations for currents in the open system.

.

4.3.1 The set-up, definitions and assumptions

We take a system that is connected to two baths at its two ends (Fig. 4.15). The full system+baths Hamiltonian is given by $\hat{\mathcal{H}} = \hat{\mathcal{H}}_S + \hat{\mathcal{H}}_{SB_1} + \hat{\mathcal{H}}_{B_1} + \hat{\mathcal{H}}_{SB_2} + \hat{\mathcal{H}}_{B_2}$, where

$\hat{\mathcal{H}}_S$ is system Hamiltonian, $\hat{\mathcal{H}}_{B_1}$ ($\hat{\mathcal{H}}_{B_2}$) is the left (right) bath Hamiltonian, $\hat{\mathcal{H}}_{SB_1}$ ($\hat{\mathcal{H}}_{SB_2}$) is system-bath coupling Hamiltonian for left (right) bath. We assume system and bath Hamiltonians to be number conserving. So $[\hat{N}_S, \hat{\mathcal{H}}_S] = [\hat{N}_{B_1}, \hat{\mathcal{H}}_{B_1}] = [\hat{N}_{B_2}, \hat{\mathcal{H}}_{B_2}] = 0$, where $\hat{N}_S, \hat{N}_{B_1}, \hat{N}_{B_2}$ are the total number operators of system, left bath and right bath respectively. We will also assume $[\hat{N}_S + \hat{N}_{B_p}, \hat{\mathcal{H}}_{SB_p}] = 0$, $[\hat{\mathcal{H}}_S + \hat{\mathcal{H}}_{B_p}, \hat{\mathcal{H}}_{SB_p}] = 0$, $p = 1, 2$. This physically means that the system-bath coupling Hamiltonians do not act as 'sources' of particle or energy. In this set-up, we define the following current operators:

$$\hat{I}_{B_p \to S} = -i[\hat{N}_{B_p}, \hat{\mathcal{H}}_{SB_p}] = i[\hat{N}_S, \hat{\mathcal{H}}_{SB_p}] = -\hat{I}_{S \to B_p}$$
$$\hat{J}_{B_p \to S} = -i[\hat{\mathcal{H}}_{B_p}, \hat{\mathcal{H}}_{SB_p}] = i[\hat{\mathcal{H}}_S, \hat{\mathcal{H}}_{SB_p}] = -\hat{J}_{S \to B_p}, \qquad (4.27)$$

$p = 1, 2$. The first line gives particle currents between the baths and the system. The second line gives energy currents between the baths and the system. We also define the operators $\hat{I}_S$ and $\hat{J}_S$ as the total particle and energy current operators of the system. We will look at the OCFDR for $\hat{I}_S$, $\hat{J}_S$. This corresponds to the transport coefficients. We assume that each of the system, bath and system-bath coupling Hamiltonians has *time reversal* and *time translation* symmetries. The full system+bath density matrix of the set-up will be denoted by $\rho_{tot}(t)$.

Now we state the most crucial assumption, the open-system thermalization. This says, the set-up is such that, when a system is connected to two baths at same temperatures and chemical potentials, eventually the whole set-up reaches a thermal equilibrium. This is mathematically stated as follows

$$\rho_{EIS}^{\hat{\mathcal{H}}} \equiv \frac{e^{-\beta(\hat{\mathcal{H}}_{B_1} - \mu\hat{N}_{B_1})}}{Z_1} \otimes \rho(0) \otimes \frac{e^{-\beta(\hat{\mathcal{H}}_{B_2} - \mu\hat{N}_{B_2})}}{Z_2}$$
$$\lim_{t \to \infty} e^{-i\hat{\mathcal{H}}t} \rho_{EIS}^{\hat{\mathcal{H}}} e^{i\hat{\mathcal{H}}t} = \frac{e^{-\beta(\hat{\mathcal{H}} - \mu\hat{N})}}{Z} \equiv \rho_{eq}^{\hat{\mathcal{H}}}. \qquad (4.28)$$

$\hat{N} = \hat{N}_S + \hat{N}_{B_1} + \hat{N}_{B_2}$ and Z_1, Z_2, Z are corresponding normalization constants (partition functions). The superscripts denote that time evolution is with the Hamiltonian $\hat{\mathcal{H}}$. A necessary not sufficient condition for this is that the baths have infinite degrees of freedom. In absence of such thermalization, linear response can still be done, but a OCFDR relating NESS currents to fluctuations in equilibrium cannot be derived. We will also make the *mixing assumption* which is as follows. Given two arbitrary operators $\hat{P}$ and $\hat{Q}$, we assume, $\lim_{t \to \infty}\langle \hat{P}(\pm t)\hat{Q}(0)\rangle = \lim_{t \to \infty}\langle \hat{P}(\pm t)\rangle\langle \hat{Q}(0)\rangle$, where $\langle ... \rangle = Tr(...\rho_{eq}^H)$. Note that this condition does *not* require the Markovian assumption that the connected part of correlations decay exponentially. This condition also holds even if correlations decay

as a power law, which is typical for non-Markovian evolution. This assumption is not absolutely necessary, but helps in some simplifications, and is generically expected to be true. Finally, when $\hat{P}$ and $\hat{Q}$ are current operators, we define the following notation

$$M(\hat{Q}, \hat{P}) \equiv \frac{1}{\beta} \int_0^\infty dt \int_0^\beta d\lambda \langle \hat{Q}(-i\lambda)\hat{P}(t) \rangle == \frac{1}{2} \int_{-\infty}^\infty dt \langle \hat{Q}(t)\hat{P}(0) \rangle \qquad (4.29)$$

where $\hat{P}(t) = e^{i\hat{\mathcal{H}}t}\hat{P}e^{-i\hat{\mathcal{H}}t}$. Comparing with Eq. 4.1, the resemblance between $M(\hat{Q}, \hat{P})$ and $D_L(\tau)$ is obvious. The second equality in Eq. 4.29 can be derived using exactly similar steps as given in Eqs. 6.56, 6.57, 6.58, 6.59, 6.60 in Appendix. 6.7. Using time translation and time-reversal symmetries, one can show $M(\hat{Q}, \hat{P}) = M(\hat{P}, \hat{Q})$. This can be shown as follows. Let $\mathcal{T}$ be the time reversal operator. Then, we have

$$\langle \hat{Q}(t)\hat{P}(t') \rangle = \langle \mathcal{T}\hat{Q}(t)\hat{P}(t')\mathcal{T}^{-1} \rangle = \langle \hat{P}(-t')\hat{Q}(-t) \rangle = \langle \hat{P}(-t'+\tau)\hat{Q}(-t+\tau) \rangle \qquad (4.30)$$

where the last line is the statement of time-translation invariance. The choice of $\tau = t + t'$ gives $\langle \hat{Q}(t)\hat{P}(t') \rangle = \langle \hat{P}(t)\hat{Q}(t') \rangle$. With this property, it is obvious that $M(\hat{Q}, \hat{P}) = M(\hat{P}, \hat{Q})$.

4.3.2 The linear response NESS

We are interested in linear response, so let $\beta_\pm = \beta \pm \epsilon\Delta\beta/2$, $\mu_\pm = \mu \pm \epsilon\Delta\mu/2$, $\epsilon \to 0$. We start the set-up in the following non-equilibrium initial state $\rho_{NIS}^{\hat{\mathcal{H}}}$,

$$\rho_{tot}(0) = \rho_{NIS}^{\hat{\mathcal{H}}} \equiv \frac{e^{-\beta_+(\hat{\mathcal{H}}_{B_1} - \mu_+\hat{N}_{B_1})}}{Z_1} \otimes \rho(0) \otimes \frac{e^{-\beta_-(\hat{\mathcal{H}}_{B_2} - \mu_-\hat{N}_{B_2})}}{Z_2}$$

$$= \frac{e^{-\beta(\hat{\mathcal{H}}'_{B_1} - \mu\hat{N}_{B_1})}}{Z_1} \otimes \rho_S \otimes \frac{e^{-\beta(\hat{\mathcal{H}}'_{B_2} - \mu\hat{N}_{B_2})}}{Z_2}, \qquad (4.31)$$

with

$$\hat{\mathcal{H}}'_{B_1} = \hat{\mathcal{H}}_{B_1} + \frac{\epsilon}{2\beta}(\hat{\mathcal{H}}_{B_1}\Delta\beta - \hat{N}_{B_1}\Delta(\mu\beta)),$$

$$\hat{\mathcal{H}}'_{B_2} = \hat{\mathcal{H}}_{B_2} - \frac{\epsilon}{2\beta}(\hat{\mathcal{H}}_{B_2}\Delta\beta - \hat{N}_{B_2}\Delta(\mu\beta)) \qquad (4.32)$$

and $\Delta(\mu\beta) = \beta\Delta\mu + \mu\Delta\beta$. In obtaining the second line of Eq. 4.31, we have only regrouped the terms in the exponentials and neglected the ϵ^2 term. We define $\hat{\mathcal{H}}' \equiv \hat{\mathcal{H}}_S + \hat{\mathcal{H}}_{SB_1} + \hat{\mathcal{H}}'_{B_1} + \hat{\mathcal{H}}_{SB_2} + \hat{\mathcal{H}}'_{B_2} = \hat{\mathcal{H}} + \epsilon\hat{\mathcal{H}}_{pert}$, where

$$\hat{\mathcal{H}}_{pert} = \frac{1}{\beta}[\Delta\beta(\frac{\hat{\mathcal{H}}_{B_1} - \hat{\mathcal{H}}_{B_2}}{2}) + \Delta(-\beta\mu)(\frac{\hat{N}_{B_1} - \hat{N}_{B_2}}{2})], \qquad (4.33)$$

Comparing the second line of Eq. 4.31 with Eq. 4.28, we see that $\rho_{NIS}^{\hat{\mathcal{H}}} = \rho_{EIS}^{\hat{\mathcal{H}}'}$. Thus we make the crucial observation that $\rho_{NIS}^{\hat{\mathcal{H}}}$ is the non-equilibrium initial state when evolved with the Hamiltonian $\hat{\mathcal{H}}$, but, when evolved with $\hat{\mathcal{H}}'$, it is an equilibrium initial state and reaches $\rho_{eq}^{\hat{\mathcal{H}}'}$ in the long time limit,

$$\lim_{t \to \infty} e^{-i\hat{\mathcal{H}}'t} \rho_{NIS}^{\hat{\mathcal{H}}} e^{i\hat{\mathcal{H}}'t} = \lim_{t \to \infty} e^{-i\hat{\mathcal{H}}'t} \rho_{EIS}^{\hat{\mathcal{H}}'} e^{i\hat{\mathcal{H}}'t} = \rho_{eq}^{\hat{\mathcal{H}}'} \tag{4.34}$$

We are interested in time evolution with $\hat{\mathcal{H}}$. This is given by, $\frac{\partial \rho_{tot}}{\partial t} = i[\rho_{tot}, \hat{\mathcal{H}}] = i[\rho_{tot}, \hat{\mathcal{H}}'] - i\epsilon[\rho_{tot}, \hat{\mathcal{H}}_{pert}]$. Assuming $\hat{\mathcal{H}}'$ as the unperturbed Hamiltonian, $\rho_{tot}(t)$ can be solved for upto linear order in ϵ (linear response) using Dyson series. First, we go to interaction picture with respect to $\hat{\mathcal{H}}'$.

$$\rho_{tot}^I(t) = e^{i\hat{\mathcal{H}}'t} \rho_{tot}^I(t) e^{-i\hat{\mathcal{H}}'t}, \quad \hat{\mathcal{H}}_{pert}^I(t) = e^{i\hat{\mathcal{H}}'t} \hat{\mathcal{H}}_{pert}^I e^{-i\hat{\mathcal{H}}'t}. \tag{4.35}$$

Then, we have $\frac{\partial \rho_{tot}^I}{\partial t} = -i\epsilon[\rho_{tot}^I(t), \hat{\mathcal{H}}_{pert}^I(t)]$, which gives

$$\rho_{tot}^I(t) = \rho_{tot}^I(0) - i\epsilon \int_0^t dt' [\rho_{tot}^I(t'), \hat{\mathcal{H}}_{pert}^I(t')] \simeq \rho_{tot}^I(0) - i\epsilon \int_0^t dt' [\rho^I(0), \hat{\mathcal{H}}_{pert}^I(t')]. \tag{4.36}$$

To obtain the second line we have used the first line recursively in the RHS and have kept only terms upto linear order in ϵ. Going back to Schroedinger picture, and recalling $\rho_{tot}^I(0) = \rho_{EIS}^{\hat{\mathcal{H}}'}$, we get

$$\rho_{tot}(t) \simeq e^{-i\hat{\mathcal{H}}'t} \rho_{EIS}^{\hat{\mathcal{H}}'} e^{i\hat{\mathcal{H}}'t} - i\epsilon \int_0^t dt' [e^{-i\hat{\mathcal{H}}'t} \rho_{EIS}^{\hat{\mathcal{H}}'} e^{i\hat{\mathcal{H}}'t}, e^{-i\hat{\mathcal{H}}'t'} \hat{\mathcal{H}}_{pert} e^{i\hat{\mathcal{H}}'t'}]. \tag{4.37}$$

Now, taking $t \to \infty$ and using the thermalization condition Eq. 4.28, we have

$$\rho_{NESS}^{\hat{\mathcal{H}}} = \lim_{t \to \infty} \rho_{tot}(t) = \rho_{eq}^{\hat{\mathcal{H}}'} - i\epsilon \int_0^\infty dt' [\rho_{eq}^{\hat{\mathcal{H}}}, e^{-i\hat{\mathcal{H}}t'} \hat{\mathcal{H}}_{pert} e^{i\hat{\mathcal{H}}t'}] \tag{4.38}$$

In the second term, we have used $\hat{\mathcal{H}}' \to \hat{\mathcal{H}}$, because corrections above this will be of order ϵ^2.

4.3.3 The OCFDR

Let $\hat{O}$ be a particle or energy current operator, then, from Eq. 4.38, we obtain

$$\langle \hat{O} \rangle_{NESS} = i\epsilon \int_0^\infty dt' \langle [\hat{O}(t), \hat{\mathcal{H}}_{pert}] \rangle \tag{4.39}$$

where $\langle ... \rangle_{NESS} = Tr(...\rho_{NESS}^{\hat{\mathcal{H}}})$, and we have used the fact that $Tr(\hat{O}\rho_{eq}(\hat{\mathcal{H}}')) = 0$, because energy and particle current operators are odd under time-reversal while $\hat{\mathcal{H}}'$ is

even under time reversal. Deriving the second equality in above equation involves a standard technique used in deriving Kubo formula, which we call the Kubo trick. We have $\langle[\hat{O}(t), \hat{\mathcal{H}}_{pert}]\rangle = Tr(\hat{O}(t)[\hat{\mathcal{H}}_{pert}, \rho])$. Let $\hat{K} = (\hat{\mathcal{H}} - \mu\hat{N})$. Then,

$$[\hat{\mathcal{H}}_{pert}, \rho] = [\hat{\mathcal{H}}_{pert}, \frac{e^{-\beta\hat{K}}}{Z}] = \rho\tilde{\Phi}(\beta), \quad \tilde{\Phi}(\lambda) = e^{\lambda\hat{K}}\hat{\mathcal{H}}_{pert}e^{-\lambda\hat{K}} - \hat{\mathcal{H}}_{pert} \tag{4.40}$$

Thus,

$$\frac{d\tilde{\Phi}(\lambda)}{d\lambda} = e^{\lambda\hat{K}}[\hat{K}, \hat{\mathcal{H}}_{pert}]e^{-\lambda\hat{K}} = e^{\lambda\hat{\mathcal{H}}}[\hat{\mathcal{H}}, \hat{\mathcal{H}}_{pert}]e^{-\lambda\hat{\mathcal{H}}} = -ie^{\lambda\hat{\mathcal{H}}}\frac{d\hat{\mathcal{H}}_{pert}}{dt}e^{-\lambda\hat{\mathcal{H}}} = -i\dot{\hat{\mathcal{H}}}_{pert}(-i\lambda) \tag{4.41}$$

where we have used $[\hat{\mathcal{H}}_{pert}, N] = 0$ and $\dot{\hat{\mathcal{H}}}_{pert} \equiv \frac{d\hat{\mathcal{H}}_{pert}}{dt} = -i[\hat{\mathcal{H}}_{pert}, \hat{\mathcal{H}}]$. Then, we have,

$$\tilde{\Phi}(\beta) = -i\int_0^\beta d\lambda\dot{\hat{\mathcal{H}}}_{pert}(-i\lambda) \tag{4.42}$$

Using Eq. 4.40, Eq. 4.42, we have

$$\langle[\hat{O}(t), \hat{\mathcal{H}}_{pert}]\rangle = -i\int_0^\beta d\lambda Tr(\hat{O}(t)\rho\dot{\hat{\mathcal{H}}}_{pert}(-i\lambda)) = -i\int_0^\beta d\lambda\langle\dot{\hat{\mathcal{H}}}_{pert}(-i\lambda)\hat{O}(t)\rangle \tag{4.43}$$

Putting this result in Eq. 4.39 and using Eq. 4.29, we obtain,

$$\langle\hat{O}\rangle_{NESS} = \epsilon\beta M(\dot{\hat{\mathcal{H}}}_{pert}, \hat{O}) \tag{4.44}$$

where $\dot{\hat{\mathcal{H}}}_{pert} = -i[\hat{\mathcal{H}}_{pert}, \hat{\mathcal{H}}]$. Writing Eq. 4.44 explicitly for $\hat{I}_S$ and $\hat{J}_S$, using Eqs. 4.33, 4.27, and omitting ϵ for notational convenience, we obtain the transport coefficients

$$\begin{pmatrix} \langle\hat{J}_S\rangle_{NESS} \\ \langle\hat{I}_S\rangle_{NESS} \end{pmatrix} \equiv \begin{pmatrix} L_{11} & L_{12} \\ L_{21} & L_{22} \end{pmatrix} \begin{pmatrix} \Delta\beta \\ \Delta(-\mu\beta) \end{pmatrix}$$
$$= \begin{pmatrix} M(\hat{J}_B, \hat{J}_S) & M(\hat{I}_B, \hat{J}_S) \\ M(\hat{J}_B, \hat{I}_S) & M(\hat{I}_B, \hat{I}_S) \end{pmatrix} \begin{pmatrix} \Delta\beta \\ \Delta(-\mu\beta) \end{pmatrix}. \tag{4.45}$$

where $\hat{I}_B(t) = [\hat{I}_{B_1 \to S}(t) - \hat{I}_{B_2 \to S}(t)]/2$, $\hat{J}_B(t) = [\hat{J}_{B_1 \to S}(t) - \hat{J}_{B_2 \to S}(t)]/2$. The LHS of above equation involves expectation value of total system currents in NESS under infinitesimal bias, while, the RHS involves expectation value of current fluctuations in the thermal state of the whole system+bath set-up. Thus we have the OCFDR. High temperature limit of Eq. 4.45 reproduces the results for classical Hamiltonian systems connected to Langevin baths [139, 140]. The result can be straightforwardly generalized to multiple (more than two) baths. Eq. 4.45 has a form similar to definition of Onsager transport coefficients, but the Onsager relation $L_{12} = L_{21}$ clearly does not hold in general ($M(\hat{I}_B, \hat{J}_S) \neq M(\hat{J}_B, \hat{I}_S)$). Note that, since $M(\hat{Q}, \hat{P}) = M(\hat{P}, \hat{Q})$, this would not be the case if $\langle\hat{J}_B\rangle_{NESS}$, $\langle\hat{I}_B\rangle_{NESS}$ were calculated instead. Using this fact, the Onsager relation is recovered under the assumption of a *'local' system Hamiltonian*.

4.3.4 Recovering Onsager relations

A system described by a *'local' system Hamiltonian* can be broken up into L surfaces transverse to direction of current flow such that $\hat{\mathcal{H}}_S = \sum_{\ell=1}^{L} \hat{\mathfrak{H}}_\ell$, $\hat{N}_S = \sum_{\ell=1}^{L} \hat{\mathcal{N}}_\ell$, and $\hat{I}_S = \sum_{\ell=1}^{L-1} \hat{I}_{\ell \to \ell+1}$, $\hat{J}_S = \sum_{\ell=1}^{L-1} \hat{J}_{\ell \to \ell+1}$. Here $\hat{\mathfrak{H}}_\ell$ ($\hat{\mathcal{N}}_\ell$) is the 'local' energy (particle number) operator of ℓth surface, and $\hat{J}_{\ell \to \ell+1}$ ($\hat{I}_{\ell \to \ell+1}$) is the 'local' current operator giving energy (particle) flow between ℓth and $\ell + 1$th surfaces. We can write down the continuity equations

$$
\frac{d\hat{\mathcal{N}}_\ell}{dt} = \hat{I}_{\ell-1 \to \ell} - \hat{I}_{\ell \to \ell+1}, \qquad \frac{d\hat{\mathfrak{H}}_\ell}{dt} = \hat{J}_{\ell-1 \to \ell} - \hat{J}_{\ell \to \ell+1}
$$

$$
\frac{d\hat{N}_1}{dt} = \hat{I}_{B_1 \to S} - \hat{I}_{1 \to 2}, \qquad \frac{d\hat{N}_L}{dt} = \hat{I}_{L-1 \to L} - \hat{I}_{S \to B_2}
$$

$$
\frac{d\hat{\mathfrak{H}}_1}{dt} = \hat{J}_{B_1 \to S} - \hat{J}_{1 \to 2}, \qquad \frac{d\hat{\mathfrak{H}}_L}{dt} = \hat{J}_{L-1 \to L} - \hat{J}_{S \to B_2} \tag{4.46}
$$

By definition, in the (non-equilibrium) steady state, the LHS of the above equations will be zero on average. This leads us to $\langle \hat{I}_B \rangle_{NESS} = \langle (\hat{I}_{B_1 \to S} + \hat{I}_{S \to B_2}) \rangle_{NESS}/2 = \langle \hat{I}_{B_1 \to S} \rangle_{NESS} = \langle \hat{I}_{\ell \to \ell+1} \rangle_{NESS} = \langle \hat{I}_S \rangle_{NESS}/(L-1)$, and similarly for energy currents. Using Eq. 4.44 for $\langle \hat{I}_B \rangle_{NESS}$, $\langle \hat{J}_B \rangle_{NESS}$, we have,

$$
\begin{pmatrix} \langle \hat{J}_S \rangle_{NESS} \\ \langle \hat{I}_S \rangle_{NESS} \end{pmatrix} \equiv \begin{pmatrix} L_{11} & L_{12} \\ L_{21} & L_{22} \end{pmatrix} \begin{pmatrix} \Delta\beta \\ \Delta(-\mu\beta) \end{pmatrix} == (L-1) \begin{pmatrix} \langle \hat{J}_B \rangle_{NESS} \\ \langle \hat{I}_B \rangle_{NESS} \end{pmatrix}
$$

$$
= (L-1) \begin{pmatrix} M(\hat{J}_B, \hat{J}_B) & M(\hat{I}_B, \hat{J}_B) \\ M(\hat{J}_B, \hat{I}_B) & M(\hat{I}_B, \hat{I}_B) \end{pmatrix} \begin{pmatrix} \Delta\beta \\ \Delta(-\mu\beta) \end{pmatrix}. \tag{4.47}
$$

Alternatively, we can use the same trick as used in Refs. [139, 140] for classical systems. In the following, we only consider particle currents. Exactly similar analysis is possible for energy currents. We define the quantity, $\hat{\mathcal{D}}_m^{\mathcal{N}} \equiv \sum_{\ell=1}^{m} \hat{\mathcal{N}}_\ell - \sum_{\ell=m}^{L} \hat{\mathcal{N}}_\ell$. Taking time derivative using Eq. 4.46, we have

$$
\frac{d\hat{\mathcal{D}}_m^{\mathcal{N}}}{dt} = 2(\hat{I}_B(t) - \hat{I}_{m \to m+1}(t)) \Rightarrow \hat{\mathcal{D}}_m^{\mathcal{N}}(\infty) - \hat{\mathcal{D}}_m^{\mathcal{N}}(-\infty) = 2 \int_{-\infty}^{\infty} dt \left(\hat{I}_B(t) - \hat{I}_{m \to m+1}(t) \right)
$$

$$
\tag{4.48}
$$

Multiplying on the right by $\hat{I}_S(0)$ and taking expectation value, we have,

$$
\langle \hat{\mathcal{D}}_m^{\mathcal{N}}(\infty)\hat{I}_S(0) \rangle - \langle \hat{\mathcal{D}}_m^{\mathcal{N}}(-\infty)\hat{I}_S(0) \rangle = 4 \left(M(\hat{I}_B, \hat{I}_S) - \int_{-\infty}^{\infty} dt \frac{\langle \hat{I}_{m \to m+1}(t)\hat{I}_S(0) \rangle}{2} \right). \tag{4.49}
$$

Using the *mixing assumption*, $\langle \hat{\mathcal{D}}_m^{\mathcal{N}}(\pm\infty)\hat{I}_S(0) \rangle = \langle \hat{\mathcal{D}}_m^{\mathcal{N}}(\pm\infty) \rangle \langle \hat{I}_S(0) \rangle = 0$. So, summing over m, we have, $(L-1)M(\hat{I}_B, \hat{I}_S) = M(\hat{I}_S, \hat{I}_S)$. Using similar steps for other transport

coefficients also, we obtain

$$
\begin{pmatrix} \langle \hat{J}_S \rangle_{NESS} \\ \langle \hat{I}_S \rangle_{NESS} \end{pmatrix} \equiv \begin{pmatrix} L_{11} & L_{12} \\ L_{21} & L_{22} \end{pmatrix} \begin{pmatrix} \Delta\beta \\ \Delta(-\mu\beta) \end{pmatrix}
$$
$$
= \frac{1}{L-1} \begin{pmatrix} M(\hat{J}_S, \hat{J}_S) & M(\hat{I}_S, \hat{J}_S) \\ M(\hat{J}_S, \hat{I}_S) & M(\hat{I}_S, \hat{I}_S) \end{pmatrix} \begin{pmatrix} \Delta\beta \\ \Delta(-\mu\beta) \end{pmatrix}. \qquad (4.50)
$$

Since $M(Q, P) = M(P, Q)$, in Eqs. 4.47,4.50 the Onsager relation $L_{12} = L_{21}$ is satisfied. Thus Onsager relation is not satisfied if the $\hat{\mathcal{H}}_S$ is not 'local'. The forms of OCFDR given in Eq. Eqs. 4.47,4.50 may be expected based on experiments [141, 142, 143] and previous investigations in non-interacting quantum systems [144, 145, 146]. However, our derivation is a rigorous microscopic derivation of them for a very general case including interacting quantum systems. In Eq. 4.50, the OCFDR look very similar to the SGKF. But, there are two important differences. First, it involves equilibrium current fluctuations in presence of the baths. Second, the baths must have infinite degrees of freedom, but the system can be finite. These relations are thus well-defined for small and mesoscopic systems also, unlike those obtained from the SGKF. Below, we will exploit the formal similarity to establish a connection between the OCFDR and the SGKF.

4.3.5 Crossover between the open-system and the isolated thermodynamic limit

We will be looking at particle conductivity. Similar steps can be followed for OCFDR corresponding to other transport coefficients also. To this end let us define:

$$
D_L^O(t) = -\frac{\beta}{2(L-1)} \int_{-t}^{t} dt' \langle \hat{I}_S(t') \hat{I}_S(0) \rangle
$$
$$
D_L^S(t) = -\frac{\beta}{2(L-1)} \int_{-t}^{t} dt' \langle\langle \hat{I}_S(t') \hat{I}_S(0) \rangle\rangle_S \qquad (4.51)
$$

where $\langle\langle ... \rangle\rangle_S$ denotes that the average is taken over the system thermal state $\rho_S = e^{-\beta(\hat{\mathcal{H}}_S - \mu\hat{N}_S)}/Tr(e^{-\beta(\hat{\mathcal{H}}_S - \mu\hat{N}_S)})$ and the time translation operator involves only $\hat{\mathcal{H}}_S$. Note that $D_L^S(t)$ is a closed system quantity calculated with 'free boundary conditions' (as opposed to periodic boundary conditions). On the other hand, in the first line, the average is over $\rho_{eq}^{\hat{\mathcal{H}}}$, and the time translation operator involves the full system+bath Hamiltonian $\hat{\mathcal{H}}$. We call $D_L^O(t)$ the integrated equilibrium current-current correlation of the open system. Physically, this is related to open system total current noise in equilibrium

[145, 143]. The particle conductivity given by SGKF is

$$\sigma_{GK} = \lim_{t \to \infty} \left(\lim_{L \to \infty} D_L^S(t) \right), \tag{4.52}$$

where the order of limits is important and cannot be interchanged, while our open system result, when $\hat{\mathcal{H}}_S$ is 'local' (Eq. 4.50 with $\Delta\beta = 0$), says

$$\sigma_{open}(L) \equiv \lim_{\Delta\mu \to 0} \frac{\langle \hat{I}_S \rangle_{NESS}}{\Delta\mu} = \lim_{t \to \infty} D_L^O(t). \tag{4.53}$$

Now, we ask what is the behavior of $D_L^O(t)$ at a fixed t with increase in L. Since H_S is 'local' and the baths are attached only at the ends, it is intuitive that on increasing L, the effects of the baths will be seen at later times. Hence, keeping t fixed, if L is increased, the effect of the baths decrease, and $D_L^O(t)$ will tend to the closed system result $D_L^S(t)$. This reasoning leads us to conjecture

$$\lim_{L \to \infty} D_L^O(t) = \lim_{L \to \infty} D_L^S(t), \tag{4.54}$$

which implies,

$$\sigma_{GK} \equiv \lim_{t \to \infty} \left(\lim_{L \to \infty} D_L^S(t) \right) = \lim_{t \to \infty} \left(\lim_{L \to \infty} D_L^O(t) \right). \tag{4.55}$$

Here again, the order of limits cannot be interchanged. Thus, *the OCFDR and the SGKF are just two different limits of the same open system object $D_L^O(t)$.* Hence, we have obtained the relation between σ_{open} and σ_{GK} that we were after. Combining Eqs. 4.53 and 4.54, we see that $D_L^O(t)$ shows a crossover from open system behavior to isolated thermodynamic limit behavior with increase in L for fixed t, and a crossover from isolated thermodynamic limit behavior to open system behaviour with increase in t for fixed L. Note that there is no assumption of weak system-bath coupling. Studying such crossovers will allow us to quantify under what experimental conditions is the isolated thermodynamic limit effectively reached. Also, due to Eq. 4.54, our treatment can be taken as an alternate 'derivation' of the SGKF. This suggests that the SGKF may not give a transport coefficient if system Hamiltonian has long range terms. Also, the analog of Eq. 4.54 for thermal currents gives a derivation of the standard thermal conductivity formula without any assumption of local equilibrium or 'gravitational field'.

However, Eq. 4.54 is a conjecture based on physical reasoning and is hard to prove in a general setting. Let us go back to completely general the non-interacting set-up where the system and the bath Hamiltonians are quadratic and the system-bath coupling Hamiltonians as described in Eq. 2.10. The QLE for the eigenbasis annhilation operators $\{\hat{A}_\nu\}$

(defined after Eq. 2.13) is given by Eq. 2.17, which we rewrite here again for discussion,

$$\frac{d\hat{A}_\nu}{dt} = -i\varepsilon_\nu \hat{A}_\nu(t) - i\hat{\xi}_\nu(t) - \sum_\ell{}' \sum_\sigma \Phi_{\ell\nu}\Phi_{\ell\sigma} \int_0^t \mathfrak{f}_\ell(t-t')\hat{A}_\sigma(t')dt', \qquad (4.56)$$

where $\hat{\xi}_\nu(t)$ is noise operator with properties ,$\langle \hat{\xi}_\sigma(t) \rangle = 0$, $\langle \hat{\xi}_\nu^\dagger(t)\hat{\xi}_\sigma(t') \rangle = \sum_\ell{}' \Phi_{\ell\nu}\Phi_{\ell\sigma}\mathfrak{F}_\ell(t-t')$. $\mathfrak{f}_\ell(t)$ and$\mathfrak{F}_\ell(t)$ are as defined in Eq. 2.18, 2.19. $\Phi_{\ell\sigma}$, as defined in Eq. 2.13, is the coefficient of the single-particle eigenfunction of with energy ω_ν at site ℓ. This shows that the effective system-bath coupling between the νth system eigenmode and the bath attached at site ℓ goes as $\sim \sum_\sigma \Phi_{\ell\nu}\Phi_{\ell\sigma}$. The number of terms in the summation is $\sim L$. For ballistic transport, the single particle eigenfunctions are completely delocalized and each term in the summation scales as $\sim 1/L$. Thus, the effective system-bath coupling of each mode is independent of L. However, for other non-interacting cases where transport is slower than ballistic (in presence of disorder, quasiperiodic potential etc.), the single particle eigenfunctions are not completely delocalized. So each term in the summation will decay faster than $1/L$. Consequently, the effective system-bath coupling of each system eigenmode will typically decay with L. An exception will be an eigenmode localized at site ℓ, but such modes will not contribute to transport properties. By this argument, to prove Eq. 4.54 for the non-interacting set-up, it is sufficient to show that it holds for the ballistic case.

To show this, we consider the following simple set-up which shows ballistic transport,

$$\hat{\mathcal{H}}_S = \sum_{\ell=1}^L g(\hat{a}_\ell^\dagger \hat{a}_{\ell+1} + h.c), \hat{\mathcal{H}}_{B_1} = t_B\left(\sum_{s=-\infty}^0 \hat{b}_s^{1\dagger}\hat{b}_{s+1}^1 + h.c.\right), \hat{\mathcal{H}}_{B_2} = t_B\left(\sum_{s=L+1}^\infty \hat{b}_s^{2\dagger}\hat{b}_{s+1}^2 + h.c.\right),$$

$$\hat{\mathcal{H}}_{SB_1} = \gamma(\hat{a}_1^\dagger \hat{b}_0^1 + h.c.), \;\; \hat{\mathcal{H}}_{SB_2} = \gamma(\hat{a}_L^\dagger \hat{b}_{L+1}^2 + h.c.) \qquad (4.57)$$

Thus, we have a set-up where the full system+bath Hamiltonian is an infinite nearest neighbour tight-binding chain. The left bath consists of sites from $-\infty$ to 0 (with annihilation operators $\hat{b}_s^1$), the sites from 1 to L is our system (with annihilation operators $\hat{a}_\ell$), while the sites from $L+1$ to ∞ is our right bath (with annihilation operators $\hat{b}_s^2$). The two baths have same hopping parameter t_B, while the system has a different hopping parameter g. The system-bath coupling to each bath is the hopping from the system to the bath, given by the parameter γ.

For this set-up,We can calculate $\sigma_{open}(L) = (L-1)G$ directly using Eq. 4.19. To calculate $D_L^S(t)$, we use exact diagonalization of H_S. We obtain $D_L^O(t)$ by exact diagonalization of full system+bath Hamiltonian H by considering finite but large baths, and looking at times before the finite size effects of the bath become significant.
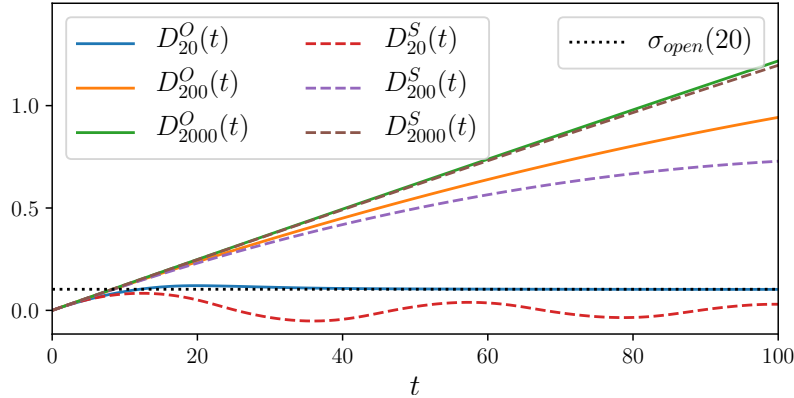
Figure 4.16: *Open to closed system crossover behavior of $D_L^O(t)$ up to a fixed time as L is increased. Parameters: $g = 0.5$, $t_B = 1$, $\gamma = 1$, $\beta = 0.1$, $\mu = 0.4$, number of bath sites=$N_B = 2000$. We have checked that for a bath of size N_B, the finite-size effects start when $t \sim N_B$.*

Plots of $D_L^O(t)$ and $D_L^S(t)$ up to a finite time $t = 100$ for several system-sizes L are shown in Fig. 4.16. We see that for small L ($L = 20$), $D_L^O(t)$ quickly saturates to the long time value $\sigma^{NESS}(L)$, while for large L ($L = 2000$), the curve for $D_L^O(t)$ approaches that for $D_L^S(t)$. Hence Eq. 4.54 holds for non-interacting set-ups and $D_L^O(t)$ shows crossover between open and closed system behaviors. Note that system-bath coupling is *not* weak ($\gamma = 1$). The situation is not so clear in presence of interactions and requires further work.

4.3.6 Summary

Thus, we have obtained several important and fundamental results in non-equilibrium statistical physics. We have considered the absolutely general open quantum set-up of a system connected to two baths with slightly different temperatures and chemical potentials. Assuming only open system thermalization, we have first given a general expression for NESS density matrix of the whole set-up in linear response regime. This expression shows that in linear response regime a unique NESS will be reached. Using this, and time-reversal and time-translation symmetries, we have obtained the open-system current fluctuation-dissipation relations without any further approximations. These have the structure of Onsager coefficients for thermoelectric transport, but the Onsager relation is not manifestly satisfied at this level. The assumption of local system Hamiltonian is required for further simplifications to obtain expressions consistent with the Onsager

relation.

Finally and most interestingly, we have argued that the integrated total current-current correlations of the open-system in equilibrium can show a crossover between open system behavior and isolated thermodynamic limit behavior. This gives the missing link between transport coefficients obtained from the open-system approach and those obtained via the Green-Kubo formalism. We have demonstrated this by direct calculation in a simple set-up showing ballistic transport, and have given a concrete argument on why the same is expected in any non-interacting set-up. This new kind of out-of-equilibrium crossover provides a general way to quantify, via current fluctuations, the conditions under which the isolated thermodynamic limit is reached in real set-ups. However, the further work is required to explore the situation in presence of interactions which is beyond the scope of the thesis.

Chapter 5

Conclusion

In this thesis, we have investigated the transport in open quantum systems with and without Born-Markov approximation. We have first developed the formalism to treat absolutely general open quantum set-ups for non-interacting systems under Born-Markov approximation. We have shown the equivalence of QME and QLE approaches in such set-ups. The evolution equation for the correlation matrix has the form of a Lyapunov equation and the condition for a unique steady state to exist is just the stability condition for the Lyapunov equation. We have checked that the Redfield QME indeed gives proper open system thermalization and have obtained a simplified expression for current for a 1D nearest neighbour chain. Then, we have extended the formalism to the case where the temperatures and/or chemical potentials of the baths are periodic functions of time (AC drive). Again, in terms of the correlation matrix, this offers a tremendous simplification and a number of physical observations can be directly made from the evolution equation for the correlation matrix.

Next, we have applied the formalisms so developed on the simple set-up of a two-site non-interacting system with each site connected to its own bath. We have compared the results from the Born-Markov approximation with exact results which is possible to obtain for such small systems. We have found very good agreement. We have also discussed results from some phenomenological Lindblad QMEs that are widely used and have shown that the Redfield QME agrees over a much wider range of parameters. In the AC driven case, we have looked at two fermionic sites connected to two baths at same temperature but with periodically varying chemical potentials. We have made a number of experimentally relevant observations. Two most important of them are as follows. Instantaneous currents under AC voltage can be orders of magnitude higher than the

time period averaged current, especially at resonances. Instantaneous current inside the system under a symmetric AC bias, i.e, where chemical potentials of both baths follow exactly the same time-dependence, can be used as a measure of asymmetry of system-bath coupling. Further, we have applied the Redfield QME to a simple interacting problem of a non-linear oscillator connected to two baths at different temperatures. We have obtained an analytical expression for the NESS density matrix. We have shown that the non-linear oscillator can have extremely interesting rectification effects, high temperature scaling and a non-trivial dependence of approach time to reach steady state on non-linearity and temperatures.

Much of the physics we have discovered under Born-Markov approximation in the AC driven and in the non-linear oscillator cases would be quite difficult to obtain without the Born-Markov approximation. They would have also been missed by some of the most widely used phenomenological Lindblad QMEs.

In the later part of the thesis, we have focussed on transport of 1D non-interacting quasiperiodic systems. This time NESS currents are calculated exactly, i.e, without Born-Markov approximation. We have looked at transport in two 1D quasiperiodic systems: the Aubry-André-Harper (AAH) model, which does not have a mobility edge and a generalization of it which has a mobility edge. We have shown that, at the critical point of the AAH model, transport behavior obtained from the open system approach and from the standard linear-response theory (spread of correlations) are drastically different. Spread of correlations in the isolated system in the thermodynamic limit shows hints of super-diffusive transport. However, the NESS current scaling with system size shows clear sub-diffusive behavior. We have explained the origin of the sub-diffusive behavior by using the simplified expression for current obtained previously under Born-Markov approximation. In the generalized AAH (GAAH) model, we have obtained the high temperature non-equilibrium phase diagram based on the current scaling with system size. We have also obtained a surprising correspondence between the eigenfuctions of the GAAH model and the AAH model. The high temperature non-equilibrium phase diagram can be explained via this correspondence and fractal properties of the spectrum.

Finally, we have given the connection between the transport coefficients obtained via open system approach and those obtained via the standard linear-response theory for isolated systems. We have shown that they are different limits of the total current auto-correlation of the open system. In the standard linear-response theory, the thermo-

dynamic limit is taken first and then the infinite time limit is taken, while in open system approach, the infinite time limit is taken first, so that the NESS is reached.

Chapter 6

Appendix

6.1 Quantum Markov process

Quantum definition of Markovianity is as follows. Let evolution equation for the density matrix $\rho(t)$ of the system be written as [21, 147]

$$\rho(t) = \Lambda(t, t_0)\rho(t_0). \tag{6.1}$$

$\Lambda(t, t_0)$ is called the propagator. The quantum process is Markovian if the propagator satisfies the following semi-group property,

$$\Lambda(t_3, t_1) = \Lambda(t_3, t_2)\Lambda(t_2, t_1), \quad \forall \ \ t_3 > t_2 > t_1. \tag{6.2}$$

What this physically means is that a process of evolving from time t_0 to time t can be broken up into arbitrary number of smaller time steps governed by the same evolution equation. If this is possible, then the process is Markovian, otherwise it is not. An explicitly non-Markovian process has the following form [21, 147]

$$\frac{\partial \rho}{\partial t} = \int_{t_0}^{t} dt' K(t - t')\rho(t'). \tag{6.3}$$

This involves a time-convolution with the density matrix. However, using the Nakajima-Zwanzig projection operator methods, such equations can also be brought into time-convolution less (TCL) form [21]. Now, let us look at two types of TCL QMEs [147] which we consider in this thesis

Case A:

$$\frac{\partial \rho}{\partial t} = \mathcal{L}\rho(t), \tag{6.4}$$

where $\mathcal{L}$ is called the Lioville operator or the Liovillian. In this case, the Liovillian is independent of time. Thus,

$$\rho(t) = e^{(t-t_0)\mathcal{L}}\rho(t_0), \quad \Rightarrow \Lambda(t, t_0) = e^{(t-t_0)\mathcal{L}}. \tag{6.5}$$

It is trivial to check this propagator satisfies the Markovian condition in Eq. 6.2. Thus, a QME where the Lioville operator is independent of time is Markovian.

Case B:

$$\frac{\partial \rho}{\partial t} = \mathcal{L}(t - t_0)\rho(t). \tag{6.6}$$

In this case, the Liovillian not only depends on time, but also has time translation invariance. The propagator for this case is

$$\Lambda(t, t_0) = T_{\leftarrow}e^{\int_{t_0}^{t} dt' \mathcal{L}(t'-t_0)} = T_{\leftarrow}e^{\int_{0}^{t-t_0} dt' \mathcal{L}(t')}, \tag{6.7}$$

where $T_{\leftarrow}$ refers to time-ordering. Now, for $t_3 > t_2 > t_1$, we have

$$\Lambda(t_3, t_2)\Lambda(t_2, t_1) = T_{\leftarrow}e^{\int_{0}^{t_3-t_2} dt' \mathcal{L}(t')} T_{\leftarrow}e^{\int_{0}^{t_2-t_1} dt' \mathcal{L}(t')}$$

$$\neq T_{\leftarrow}e^{\int_{0}^{t_3-t_1} dt' \mathcal{L}(t')} = \Lambda(t_3, t_1). \tag{6.8}$$

Thus, this case is not Markovian according to Eq. 6.2.

6.2 Nakajima-Zwanzig projection operators method

Here we derive QMEs under weak system-bath coupling using Nakajima-Zwanzig projection operators method. To this end, we consider a system, connected to a bath defined by the full system+bath Hamiltonian,

$$\hat{\mathcal{H}} = \hat{\mathcal{H}}_S + \hat{\mathcal{H}}_B + \varepsilon\hat{\mathcal{H}}_{SB}. \tag{6.9}$$

Here, $\hat{\mathcal{H}}_S$ is the system Hamiltonian, $\hat{\mathcal{H}}_B$ is the bath Hamiltonian, and $\hat{\mathcal{H}}_{SB}$ is the system-bath coupling Hamiltonian. ε is the small parameter controlling system-bath coupling. The whole system+bath set-up is assumed to be isolated. Let ρ_{tot} be the density matrix of the whole system+bath set-up. We will assume product initial state for the set-up

$$\rho_{tot}(t_0) = \rho(t_0) \otimes \rho_B, \tag{6.10}$$

where $\rho(t_0)$ is the initial state of the system and ρ_B is the initial state of the bath, and t_0 is the initial time. Our goal is to obtain the equation of motion for

$$\rho(t) = Tr_B(\chi(t)), \tag{6.11}$$

where $Tr_B(...)$ refers to trace over the bath degrees of freedom. First, we go to interaction picture with respect to $\hat{\mathcal{H}}_S + \hat{\mathcal{H}}_B$,

$$\hat{\mathcal{H}}_{SB}^I(t) = e^{i(\hat{\mathcal{H}}_S + \hat{\mathcal{H}}_B)t} \hat{\mathcal{H}}_{SB} e^{-i(\hat{\mathcal{H}}_S + \hat{\mathcal{H}}_B)t}$$

$$\rho_{tot}^I(t) = e^{i(\hat{\mathcal{H}}_S + \hat{\mathcal{H}}_B)t} \rho_{tot}(t) e^{-i(\hat{\mathcal{H}}_S + \hat{\mathcal{H}}_B)t}, \tag{6.12}$$

and $\rho^I(t) = Tr_B(\rho_{tot}^I(t))$. The equation of motion for $\rho_{tot}^I(t)$ is,

$$\frac{\partial \rho_{tot}^I}{\partial t} = -i\varepsilon[\hat{\mathcal{H}}_{SB}^I(t), \rho_{tot}^I(t)] \equiv \varepsilon \mathcal{L}(t)\rho_{tot}^I(t), \tag{6.13}$$

where the Liovillian is defined by the operation, $\mathcal{L}(t)\bullet \equiv -i[\hat{\mathcal{H}}_{SB}^I(t), \bullet]$.

Now, we define the Nakajima-Zwanzig projection operators,

$$\mathbb{P}\bullet \equiv (Tr_B(\bullet)) \otimes \rho_B, \quad \mathbb{Q} = \mathbb{I} - \mathbb{P}, \tag{6.14}$$

where $\mathbb{I}$ is the identity operator. $\mathbb{P}\rho_{tot}^I(t) \equiv (Tr_B(\rho_{tot}^I(t))) \otimes \rho_B = \rho^I(t) \otimes \rho_B$. It can be checked that $\mathbb{P}$ and $\mathbb{Q}$ have the usual properties of projection operators

$$\mathbb{P}^2 = \mathbb{P}, \quad \mathbb{Q}^2 = \mathbb{Q}, \quad \mathbb{P}\mathbb{Q} = \mathbb{Q}\mathbb{P} = 0. \tag{6.15}$$

We make a simplifying assumption that holds true for most commonly used bath Hamiltonians $\hat{\mathcal{H}}_B$ and system-bath couplings $\hat{\mathcal{H}}_{SB}$,

$$Tr_B\left(\hat{\mathcal{H}}_{SB}^I(t)\rho_B\right) = 0. \tag{6.16}$$

With this assumption,

$$\mathbb{P}\mathcal{L}(t)\mathbb{P}\rho_{tot}^I(t) = \mathbb{P}\left(\mathcal{L}(t)\mathbb{P}\right) = -i\mathbb{P}\left([\hat{\mathcal{H}}_{SB}^I(t), \mathbb{P}\rho_{tot}^I(t)]\right)$$

$$= -i\mathbb{P}\left([\hat{\mathcal{H}}_{SB}^I(t), \rho^I(t) \otimes \rho_B]\right)$$

$$= -iTr_B\left([\hat{\mathcal{H}}_{SB}^I(t), \rho^I(t) \otimes \rho_B]\right) \otimes \rho_B$$

$$= -i[Tr_B\left(\hat{\mathcal{H}}_{SB}^I(t)\rho_B\right), \rho^I(t)] \otimes \rho_B \tag{6.17}$$

$$\Rightarrow \mathbb{P}\mathcal{L}(t)\mathbb{P}\rho_{tot}^I(t) = 0, \tag{6.18}$$

where in the last line we have used Eq. 6.16. We operate $\mathbb{P}$ and $\mathbb{Q}$ on the equation of motion for $\rho_{tot}^I(t)$, Eq. 6.13,

$$\mathbb{P}\frac{\partial \rho_{tot}^I}{\partial t} = \frac{\partial \mathbb{P}\rho_{tot}^I}{\partial t} = \frac{\partial \rho^I}{\partial t} \otimes \rho_B = \varepsilon\mathbb{P}\mathcal{L}(t)\rho_{tot}^I(t) \tag{6.19}$$

$$\mathbb{Q}\frac{\partial \rho_{tot}^I}{\partial t} = \varepsilon\mathbb{Q}\mathcal{L}(t)\rho_{tot}^I(t) \tag{6.20}$$

It is clear that we need to simplify Eq. 6.19 to obtain the equation of motion for ρ. The idea is to formally solve Eq. 6.20 and use the solution in Eq. 6.19. To do this, first, using the resolution of identity, $\mathbb{I} = \mathbb{P} + \mathbb{Q}$, we rewrite Eqs. 6.19, 6.20,

$$\frac{\partial \mathbb{P}\rho_{tot}^I}{\partial t} = \varepsilon\mathbb{P}\mathcal{L}(t)(\mathbb{P} + \mathbb{Q})\rho_{tot}^I(t) = \varepsilon\mathbb{P}\mathcal{L}(t)\mathbb{Q}\rho_{tot}^I(t) \tag{6.21}$$

$$\frac{\partial \mathbb{Q}\rho_{tot}^I}{\partial t} = \varepsilon\mathbb{Q}\mathcal{L}(t)(\mathbb{P} + \mathbb{Q})\rho_{tot}^I(t)$$

$$= \varepsilon\mathbb{Q}\mathcal{L}(t)\mathbb{Q}\rho_{tot}^I(t) + \varepsilon\mathbb{Q}\mathcal{L}(t)\mathbb{P}\rho_{tot}^I(t), \tag{6.22}$$

where in Eq. 6.21 we have used Eq. 6.18. The formal solution of Eq. 6.22 is given by

$$\mathbb{Q}\rho_{tot}^I(t) = \varepsilon\int_{t_0}^t dt' G_{\leftarrow}(t,t')\mathcal{L}(t')\mathbb{P}\rho_{tot}^I(t'), \quad \text{where,}$$

$$G_{\leftarrow}(t,t_0) = T_{\leftarrow}e^{\varepsilon\int_{t_0}^t dt' \mathbb{Q}\mathcal{L}(t')}. \tag{6.23}$$

Here we have used the fact that the initial state is factorized as in Eq. 6.10, so that $\mathbb{Q}\rho_{tot}(t_0) = 0$. Using this solution in Eq. 6.21, we have

$$\frac{\partial \mathbb{P}\rho_{tot}^I}{\partial t} = \varepsilon^2\int_{t_0}^t dt' \mathbb{P}\mathcal{L}(t)G_{\leftarrow}(t,t')\mathcal{L}(t')\mathbb{P}\rho_{tot}^I(t'). \tag{6.24}$$

The above QME has a time-convolution and is hence explicitly non-Markovian. We now reduce Eq. 6.24 to time-convolution-less form. To do that, we go back to Eq. 6.13, and write down the formal solution for $\rho_{tot}^I(t)$

$$\rho_{tot}^I(t) = G_{\leftarrow}^{\rho_{tot}}(t,t_0)\rho_{tot}^I(t_0), \quad G_{\leftarrow}^{\rho_{tot}}(t,t_0) = T_{\leftarrow}e^{\varepsilon\int_{t_0}^t dt' \mathcal{L}(t')}. \tag{6.25}$$

Since the full system+bath is isolated, the time-dynamics of $\rho_{tot}^I(t)$ is not dissipative. So, $G_{\leftarrow}^{\rho_{tot}}(t,t_0)$ can be inverted to obtain the time-reversed equation,

$$\rho_{tot}^I(t') = G_{\rightarrow}^{\rho_{tot}}(t',t)\rho_{tot}^I(t),$$

$$G_{\rightarrow}^{\rho_{tot}}(t',t) = T_{\rightarrow}e^{\varepsilon\int_t^{t'} dt_1 \mathcal{L}(t_1)}, \quad \text{where } t' < t, \tag{6.26}$$

and $T_{\rightarrow}$ refers to time anti-ordering. Using Eq. 6.26 in Eq. 6.24, we have

$$\frac{\partial \mathbb{P}\rho_{tot}^I}{\partial t} = \varepsilon^2\int_{t_0}^t dt' \mathbb{P}\mathcal{L}(t)G_{\leftarrow}(t,t')\mathcal{L}(t')\mathbb{P}G_{\rightarrow}^{\rho_{tot}}(t',t)\rho_{tot}^I(t). \tag{6.27}$$

Now, we have the time-convolution-less form, the RHS depending only on $\rho_{tot}^I(t)$, and not on an integration over all previous times. But still the non-Markovian nature is preserved, as seen from the fact that it was derived from Eq. 6.24 without any further assumptions. $G_{\leftarrow}(t,t')$ and $G_{\rightarrow}^{\rho_{tot}}(t',t)$ can both be expanded as a power series in ε, and hence, order by order expansion in ε is possible. We see that the leading order term in Eq. 6.27 is $O(\varepsilon^2)$, since $G_{\leftarrow}(t,t') = \mathbb{I} + O(\varepsilon)$, $G_{\rightarrow}^{\rho_{tot}}(t',t) = \mathbb{I} + O(\varepsilon)$. The Born approximation pertains to keeping only the leading order term. Thus, the QME up to leading order term is

$$\frac{\partial \mathbb{P}\rho_{tot}^I}{\partial t} = \varepsilon^2 \int_{t_0}^t dt' \mathbb{P}\mathcal{L}(t)\mathcal{L}(t')\mathbb{P}\rho_{tot}^I(t),$$

$$\Rightarrow \frac{\partial \rho^I}{\partial t} = -\varepsilon^2 \int_{t_0}^t dt' Tr_B[\hat{\mathcal{H}}_{SB}^I(t),[\hat{\mathcal{H}}_{SB}^I(t'),\rho^I(t)\otimes\rho_B]], \qquad (6.28)$$

where the second line is obtained by explicitly writing out the the first line using the definitions of the notations. Eq. 6.28 is sometimes called the TCL2 (time-convolution-less, up to second order) in literature. Going back to Schroedinger picture, we have,

$$\frac{\partial \rho}{\partial t} = i[\rho,\hat{\mathcal{H}}_S] - \varepsilon^2 \int_0^{t-t_0} dt' Tr_B[\hat{\mathcal{H}}_{SB},[\hat{\mathcal{H}}_{SB}^I(-t'),\rho(t)\otimes\rho_B]], \qquad (6.29)$$

where $\hat{\mathcal{H}}_{SB}^I(t')$ is as defined in Eq. 6.12. This equation has the form of Eq. 6.6 and hence is non-Markovian.

6.3 The perturbative solution of the Lyapunov equation and thermalization

Although Eq. 2.41 can be exactly solved, it gives correct answers only up to the leading order term in ε (as discussed in Sec. 2.1.3 and [27]). So, it is useful to find analytical expressions for $\mathbf{C}(t)$ up to the leading order term in ε. Using the form given in Eq. 2.33, it is possible to find such perturbative solution under the condition

$$\omega_\alpha - \omega_\nu \gg \varepsilon^2 \left(v_{\alpha\alpha} + v_{\nu\nu}^*\right), \quad \forall \ \alpha \neq \nu. \qquad (6.30)$$

To this end, first we define

$$w_{\alpha\nu} = i(\omega_\alpha - \omega_\nu) + \varepsilon^2 \left(v_{\alpha\alpha} + v_{\nu\nu}^*\right). \qquad (6.31)$$

The perturbative solutions of Eq. 2.33 up to leading order in ε are given by

$$C_{\alpha\alpha}(t) \simeq C_{\alpha\alpha}(0)e^{-2\varepsilon^2 f_{\alpha\alpha}(\omega_\alpha)t} + \frac{F_{\alpha\alpha}(\omega_\alpha)}{f_{\alpha\alpha}(\omega_\alpha)}(1 - e^{-2\varepsilon^2 f_{\alpha\alpha}(\omega_\alpha)t})$$

$$C_{\alpha\nu}(t) \simeq C_{\alpha\nu}(0)e^{-w_{\alpha\nu}t} - \frac{i\varepsilon^2 Q_{\alpha\nu}}{\omega_\alpha - \omega_\nu}(1 - e^{-w_{\alpha\nu}t})$$

$$+ \frac{i\varepsilon^2}{\omega_\alpha - \omega_\nu}\left[v_{\nu\alpha}^* C_{\alpha\alpha}(0)(e^{-2\varepsilon^2 f_{\alpha\alpha}(\omega_\alpha)t} - e^{-w_{\alpha\nu}t}) + v_{\alpha\nu} C_{\nu\nu}(0)(e^{-2\varepsilon^2 f_{\nu\nu}(\omega_\alpha)t} - e^{-w_{\alpha\nu}t}) \right]$$

$$+ \frac{i\varepsilon^2}{\omega_\alpha - \omega_\nu}\left[v_{\nu\alpha}^* \frac{F_{\alpha\alpha}(\omega_\alpha)}{f_{\alpha\alpha}(\omega_\alpha)}(1 - e^{-2\varepsilon^2 f_{\alpha\alpha}(\omega_\alpha)t}) + v_{\alpha\nu} \frac{F_{\nu\nu}(\omega_\nu)}{f_{\nu\nu}(\omega_\nu)}(1 - e^{-2\varepsilon^2 f_{\nu\nu}(\omega_\nu)t}) \right]. \quad (6.32)$$

Real part of $w_{\alpha\nu}$ is $f_{\alpha\alpha}(\omega_\alpha) + f_{\nu\nu}(\omega_\nu)$ (see Eqs. 2.31, 6.31). $f_{\alpha\alpha}(\omega_\alpha) > 0$ by construction (see Eq. 2.23). Thus, for time $t \gg [\varepsilon^2 f_{\alpha\alpha}(\omega_\alpha)]^{-1}$, the steady state is reached. The perturbative results for the steady state are given by

$$C_{\alpha\alpha}(\infty) = \frac{F_{\alpha\alpha}(\omega_\alpha)}{f_{\alpha\alpha}(\omega_\alpha)} = \frac{\sum_\ell' \Phi_{\ell\alpha}^2 \mathfrak{J}_\ell(\omega_\alpha)\mathfrak{n}_\ell(\omega_\alpha)}{\sum_\ell' \Phi_{\ell\alpha}^2 \mathfrak{J}_\ell(\omega_\alpha)} \quad (6.33)$$

$$C_{\alpha\nu}(\infty) = \frac{i\varepsilon^2}{\omega_\alpha - \omega_\nu}\left[\frac{v_{\nu\alpha}^* F_{\alpha\alpha}(\omega_\alpha)}{f_{\alpha\alpha}(\omega_\alpha)} + \frac{v_{\alpha\nu} F_{\nu\nu}(\omega_\nu)}{f_{\nu\nu}(\omega_\nu)} - Q_{\alpha\nu} \right]. \quad (6.34)$$

These equations reveal the very important physics of thermalization. In equilibrium all baths have same temperatures and chemical potentials, i.e, the Bose or Fermi distributions of all the baths are exactly the same, $\mathfrak{n}_\ell(\omega) \to \mathfrak{n}(\omega)$. Thus, from Eq. 6.33, $C_{\alpha\alpha}(\infty) = \mathfrak{n}(\omega_\alpha)$. So we get the non-trivial and physically important result that

$$\text{in equilibrium,} \quad \lim_{\varepsilon \to 0}\left(\lim_{t \to \infty} \rho(t) \right) = \frac{e^{\beta(\hat{\mathcal{H}}_S - \mu\hat{N}_S)}}{Tr\left(e^{\beta(\hat{\mathcal{H}}_S - \mu\hat{N}_S)} \right)}, \quad (6.35)$$

where the order of limits cannot be changed, and $\hat{N}_S = \sum_{\alpha=1}^N \hat{A}_\alpha^\dagger \hat{A}_\alpha$. Note that the $\varepsilon \to 0$ limit is consistent with Eq. 6.30. Thus the set-up shows thermalization in this sense.

Away from equilibrium, when the temperatures and chemical potentials of the baths are different, there will be non-zero current in NESS. For systems with time-reversal symmetry, as we are considering here, the current in NESS depends directly on the imaginary part of the off-diagonal elements $C_{\alpha\nu}$. The imaginary part of $C_{\alpha\nu}$ can be explicitly written as

$$\text{Im}\left(C_{\alpha\nu}(\infty) \right) = \frac{\varepsilon^2}{\omega_\alpha - \omega_\nu}\left[\frac{\sum_{\ell,m}' \Phi_{m\alpha}^2 \Phi_{\ell\alpha}\Phi_{\ell\nu}\mathfrak{J}_\ell(\omega_\alpha)\mathfrak{J}_m(\omega_\alpha)\left(\mathfrak{n}_m(\omega_\alpha) - \mathfrak{n}_\ell(\omega_\alpha) \right)}{\sum_\ell' \Phi_{\ell\alpha}^2 \mathfrak{J}_\ell(\omega_\alpha)} + (\alpha \leftrightarrow \nu) \right].$$

$$(6.36)$$

In equilibrium, $\mathfrak{n}_\ell(\omega_\alpha) = \mathfrak{n}_m(\omega_\alpha) = \mathfrak{n}(\omega_\alpha)$, so $\text{Im}(C_{\alpha\nu}(\infty)) = 0$, which is consistent with the fact that there is no steady state current in equilibrium. Eq. 6.36 can be used for a 1D chain to obtain a simplified expression for current.

The perturbative results in this section hold in the regime where the condition in Eq. 6.30 is satisfied. Outside this regime, one has to use the full solution in Eq. 2.44.

6.4   Simple expression for current and conductance for 1D chain

Here we derive a simple and insightful expression for current for 1D chain with nearest neighbour hopping using Eq. 6.36. The system Hamiltonian we will be considering is given by

$$\hat{\mathcal{H}}_S = \sum_{\ell=1}^{N} V_\ell \hat{a}_\ell^\dagger \hat{a}_\ell + \sum_{\ell=1}^{N-1} g_\ell \left(\hat{a}_\ell^\dagger \hat{a}_{\ell+1} + \hat{a}_{\ell+1}^\dagger \hat{a}_\ell \right). \tag{6.37}$$

In other words, $\mathbf{H}^S$ in Eq. 2.10 is now the tridiagonal matrix

$$\mathbf{H}^S = \begin{bmatrix} V_1 & g_1 & 0 & \cdots & \cdots \\ g_1 & V_2 & g_2 & 0 & \cdots \\ 0 & g_2 & V_3 & g_3 & 0 \\ \vdots & \ddots & \ddots & \ddots & \ddots \\ \cdots & \cdots & 0 & g_{N-1} & V_N \end{bmatrix} \tag{6.38}$$

In going to the single-particle eigenbasis we have to diagonalise $\mathbf{H}^2$ as in Eq. 2.13. Writing out Eq. 2.13 explicitly for Eq. 6.38, we have the following set of equations

$$\Phi_{\ell\alpha}(\omega_\alpha - V_\ell) = g_\ell \Phi_{\ell+1\alpha} + g_{\ell-1}\Phi_{\ell-1\alpha} \quad \forall \quad \ell \neq 1, N;$$

$$\Phi_{1\alpha}(\omega_\alpha - V_1) = g_1 \Phi_{2\alpha}, \quad \Phi_{N\alpha}(\omega_\alpha - V_N) = g_{N-1}\Phi_{N-1\alpha}. \tag{6.39}$$

The expression for particle current is obtained from the continuity equation of local density $\langle \hat{a}_p^\dagger \hat{a}_p \rangle$. The expression for particle current I is

$$I = g_p \mathrm{Im}(\langle \hat{a}_p^\dagger \hat{a}_{p+1} \rangle) = g_p \sum_{\alpha,\nu=1}^{N} \Phi_{p\alpha}\Phi_{p\nu}\mathrm{Im}(C_{\alpha\nu}). \tag{6.40}$$

Using Eq. 6.34, and simplifying, the expression for NESS current becomes,

$$I = \varepsilon^2 g_p \sum_{\alpha,\nu=1}^{N} \frac{\Phi_{p\alpha}\Phi_{p+1\nu} - \Phi_{p\nu}\Phi_{p+1\alpha}}{\omega_\alpha - \omega_\nu} \left[\frac{\sum'_{\ell,m} \Phi_{m\alpha}^2 \Phi_{\ell\alpha}\Phi_{\ell\nu}\mathfrak{J}_\ell(\omega_\alpha)\mathfrak{J}_m(\omega_\alpha)\left(\mathfrak{n}_m(\omega_\alpha) - \mathfrak{n}_\ell(\omega_\alpha)\right)}{\sum'_\ell \Phi_{\ell\alpha}^2\mathfrak{J}_\ell(\omega_\alpha)} \right].$$

$$\tag{6.41}$$

Remember, since we have used Eq. 6.36, above expression for current is only valid when Eq. 6.30 is satisfied. Current in NESS is same everywhere. However, in above expression it seems to depend on the site p where it is evaluated. But that is actually not the case as we will find via further simplification. For this, we now obtain an interesting result for tridiagonal matrices using Eq. 6.39,

$$\Phi_{p\alpha}\Phi_{p+1\nu} - \Phi_{p\nu}\Phi_{p+1\alpha} = \frac{\omega_\nu - \omega_\alpha}{g_p} \sum_{k=1}^{p} \Phi_{k\alpha}\Phi_{k\nu}. \qquad (6.42)$$

Also, the eigenvectors are orthogonal, so

$$\sum_{\nu=1}^{N} \Phi_{\ell\alpha}\Phi_{m\nu} = \delta_{\ell m}. \qquad (6.43)$$

Using Eqs. 6.42, 6.43 in Eq. 6.41, we obtain the final expression for current

$$I = \varepsilon^2 \sum_{\alpha=1}^{N} \left[\frac{\sum'_{\ell,m} \Phi_{m\alpha}^2 \Phi_{\ell\alpha}^2 \mathfrak{J}_\ell(\omega_\alpha)\mathfrak{J}_m(\omega_\alpha)\left(\mathfrak{n}_\ell(\omega_\alpha) - \mathfrak{n}_m(\omega_\alpha)\right)}{\sum'_\ell \Phi_{\ell\alpha}^2 \mathfrak{J}_\ell(\omega_\alpha)} \right]. \qquad (6.44)$$

Now, I is independent of the site p where it is evaluated and hence is same everywhere, as physically expected. Remember that $\sum'$ refers to sum over the points where the baths are attached. So, we see that current in this limit (Eq. 6.30) is governed by the amplitudes of the single-particle eigenfunctions at the sites where the baths are attached.

Now, let us consider the case where the baths are attached only at two sites, say p and q, and the bath spectral functions are same, $\mathfrak{J}_\ell(\omega) = \mathfrak{J}(\omega)$, $\ell = r, s$. Then,

$$I = \varepsilon^2 \sum_{\alpha=1}^{N} \left[\frac{\Phi_{r\alpha}^2 \Phi_{s\alpha}^2}{\Phi_{r\alpha}^2 + \Phi_{s\alpha}^2} \mathfrak{J}(\omega_\alpha)\left(\mathfrak{n}_r(\omega_\alpha) - \mathfrak{n}_s(\omega_\alpha)\right) \right]. \qquad (6.45)$$

We can now obtain an insightful expression for particle conductance of a fermionic system. Let set-up be fermionic with the two baths have same temperature, $\beta_r = \beta_s = \beta$, but different chemical potentials, $\mu_r = \mu + \Delta\mu, \mu_s = \mu$. Then particle conductance is given by,

$$\begin{aligned} G &= \lim_{\Delta\mu \to 0} \frac{dI}{d\mu} \\ &= \varepsilon^2 \beta \sum_{\alpha=1}^{N} \left[\frac{\Phi_{r\alpha}^2 \Phi_{s\alpha}^2}{\Phi_{r\alpha}^2 + \Phi_{s\alpha}^2} \mathfrak{J}(\omega_\alpha)\mathfrak{n}^2(\omega_\alpha)e^{\beta(\omega_\alpha - \mu)} \right] \end{aligned} \qquad (6.46)$$

In the so called 'wide-band limit', the bath spectral function is constant, $\mathfrak{J}(\omega_\alpha) = \Gamma$. In the high temperature limit, $\mathfrak{n}^2(\omega_\alpha)e^{\beta(\omega_\alpha - \mu)} \simeq 1/4$. So particle conductance of the fermionic system in wide-band and high temperature limit is given by

$$G = \varepsilon^2 \frac{\Gamma\beta}{4} W(r,s), \quad W(r,s) = \sum_{\alpha=1}^{N} \left[\frac{\Phi_{r\alpha}^2 \Phi_{s\alpha}^2}{\Phi_{r\alpha}^2 + \Phi_{s\alpha}^2} \right] \qquad (6.47)$$

Thus, in this limit, $W(r, s)$ is proportional to conductance. It is interesting to note that $W(r, s)$ depends only on system eigenfunctions and is independent of the baths. It is essentially an isolated system quantity, but to derive Eq. 6.47, we required to consider an open system. This expression is used in subsection. 4.2.1 to explain the sub-diffusive behavior of current in the open AAH model at the critical point.

6.5   Problem with ELQME

In the ELQME (Eq. 3.1.1), problems arise in the definitions of NESS current. For our Hamiltonian Eq. 3.1, current can be derived from the following equations:

$$\frac{d\langle \hat{a}_1^\dagger \hat{a}_1 \rangle}{dt} = I_{B^{(1)} \to 1} - I_{1 \to 2} \tag{6.48}$$

$$\frac{d\langle \hat{a}_1^\dagger \hat{a}_1 + \hat{a}_2^\dagger \hat{a}_2 \rangle}{dt} = I_{B^{(1)} \to 1} - I_{2 \to B^{(2)}} \tag{6.49}$$

where $I_{B^{(1)} \to 1}$ is the current between left bath and left system site, $I_{1 \to 2}$ is the current between left and right system sites and $I_{2 \to B^{(2)}}$ is the current between right site and right bath. Note that the expression for $I_{1 \to 2}$ is same from all three approaches RQME, LLQME, ELQME because it comes from the non-dissipative part of the QME. On the other hand, depending on whether the approach is RQME or LLQME or ELQME, the expressions for $I_{B^{(1)} \to 1}$ and $I_{2 \to B^{(2)}}$ are different as they come from the dissipative part. In NESS all three currents defined above are equal. This is true for RQME and LLQME. But ELQME gives $I_{1 \to 2} = 0$ even in NESS while giving an non-zero current for $I_{B^{(1)} \to 1}$. In fact, Eq. 6.48, from ELQME, becomes of the form $\frac{d\langle \hat{a}_1^\dagger \hat{a}_1 \rangle}{dt} = I_{B^{(1)} \to 1} - I_{1 \to B^{(2)}}$, where a fictitious $I_{1 \to B^{(2)}}$ current from left site to right bath appears which is completely unphysical as there is no direct connection between left site and right bath. However, if Eq. 6.49 is used, then ELQME gives the same result as obtained from the RQME in the limit $g \gg (\varepsilon^2/t_B)$. This is because $I_{B^{(1)} \to 1}$ obtained from Eq. 6.49 depends only on N_1, N_2 which are correctly given by ELQME when $g \gg (\varepsilon^2/t_B)$. Thus, though ELQME is not physically self consistent, this trick can be used to obtain the correct current in our setup, as done in various places [44, 45]. However, this trick will not work in cases with different geometries. For example, if two sites of a ring are connected to two different baths, ELQME will not be able to give current flowing in the two arms.
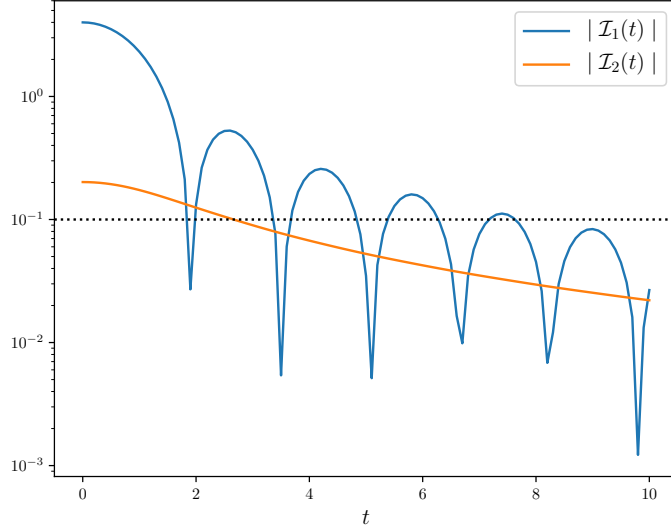
Figure 6.1: *Plots of absolute values of $\mathcal{I}_1(t)$ and $\mathcal{I}_2(t)$ (Eq. 6.50) for the parameters of the lower temperature bath in Fig. 3.4. The parameters are $t_B = 1$, $\Gamma = 4$ (see Eq. 6.51), $\beta = 1.8$, $\mu = -2.5$, $\varepsilon = 0.1$. The horizontal dotted line corresponds to the value of ε, which is $\varepsilon = 0.1$. From the plot it is clear that $\tau_B \sim 7$, which is the time by which both $\mathcal{I}_1(t)$ and $\mathcal{I}_2(t)$ have decayed to $O(\varepsilon)$. Time is measured in units of ω_0^{-1} and energies are measured in units of ω_0 (see Eq. 3.1).*

6.6 Finding bath relaxation time

Estimation of the bath relaxation time τ_B is important to ensure validity of the Born-Markov approximation. Let,

$$\mathcal{I}_1(t) = \int \frac{d\omega}{2\pi} \mathfrak{J}(\omega) e^{-i\omega t}, \quad \mathcal{I}_2(t) = \int \frac{d\omega}{2\pi} \mathfrak{J}(\omega) \mathfrak{n}(\omega) e^{i\omega t} \tag{6.50}$$

where $\mathfrak{J}(\omega)$ is the bath spectral function and $\mathfrak{n}(\omega)$ is the Bose or Fermi distribution of the bath (see Eqs. 2.12, 2.11). Let ε be the small parameter controlling strength of system-bath coupling. Under Born-Markov approximation, the evolution equations are written down up to leading order in ε. Then, as discussed in Sec. 2.3.1, the bath relaxation time τ_B is governed by the time required for $\mathcal{I}_1(t)$ and $\mathcal{I}_2(t)$ to decay to $O(\varepsilon)$. Let τ_{B_1} (τ_{B_2}) be the time in which $\mathcal{I}_1(t)$ ($\mathcal{I}_2(t)$) decay to $O(\varepsilon)$. Then τ_B is given by $max\{\tau_{B_1}, \tau_{B_2}\}$. The Markov approximation is valid for observation time t satisfying $t \gg \tau_B$. It is clear from the forms of $\mathcal{I}_1(t)$ and $\mathcal{I}_2(t)$ that τ_B will be smaller if the integrands are non-zero over a wider range of ω. Thus, τ_B will decrease with increasing temperature and bandwidth of the bath. We now find the values of τ_B for the various choices of baths spectral functions and bath parameters used in Chap. 3. This is particularly important for the time dynamics
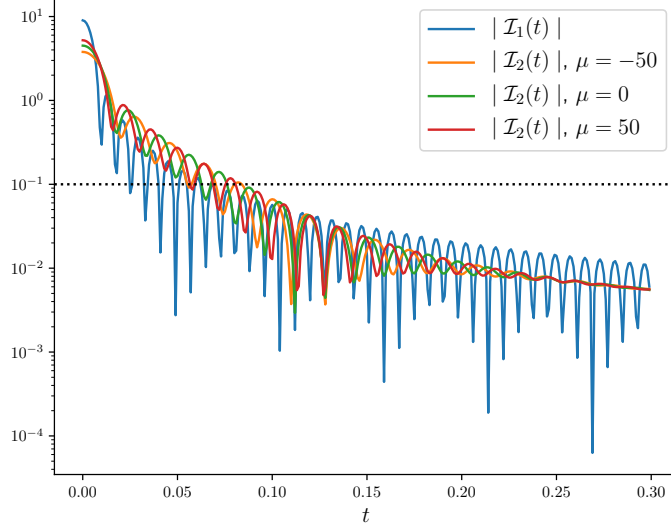
Figure 6.2: *Plots of absolute values of $\mathcal{I}_1(t)$ and $\mathcal{I}_2(t)$ (Eq. 6.50) for the parameters of the bath that is stronger coupled to the system in Fig. 3.6. The parameters are $t_B = 200$, $\Gamma = 9$ (see Eq. 6.51), $\beta = 0.1$. $| \mathcal{I}_2(t) |$ has been shown for three values of μ. The horizontal dotted line corresponds to the value of ε, which is $\varepsilon = 0.1$. From the plot it is clear that $\tau_B \sim 0.1$, which is the time by which both $\mathcal{I}_1(t)$ and $\mathcal{I}_2(t)$ have decayed to $O(\varepsilon)$. This value does not change on changing μ. Time is measured in units of ω_0^{-1} and energies are measured in units of ω_0 (see Eq. 3.1).*

of approach to steady state, and for the AC driven case.

First, let us find τ_B for the parameters of Sec. 3.1.1. The time dynamics in the DC case has been presented in Figs. 3.3, 3.4 for the bosonic system. The bath spectral function is

$$\mathfrak{J}(\omega) = \Gamma\sqrt{1 - \frac{\omega^2}{4t_B^2}}, \quad \Gamma = \frac{2\gamma^2}{t_B}. \tag{6.51}$$

The plots of absolute values of $\mathcal{I}_1(t)$ and $\mathcal{I}_2(t)$ for the parameters of the lower temperature bath in Fig. 3.4 are given in Fig. 6.1. From the plots it is clear that $\tau_B \sim 7$ ($\tau_{B_1} \sim 7, \tau_{B_2} \sim 3$), in units of ω_0^{-1} (see Eq. 3.1).

Next, we look at Sec. 3.1.2, which is the considers two fermionic sites under AC voltage. The bath spectral function is still of the form Eq. 6.51. However, this has a more stringent requirement, because, Born-Markov approximation has to hold in every time step, and for all values of chemical potentials. The bath spectral function here is the same as Eq. 6.51. However, now, t_B is taken very large, $t_B = 200$ to make the Born-Markov approximation very accurate. Fig. 6.2 shows plots of absolute values of $\mathcal{I}_1(t)$ and $\mathcal{I}_2(t)$ for the parameters of the bath that is stronger coupled to the system in Fig. 3.6. From the plot it is clear
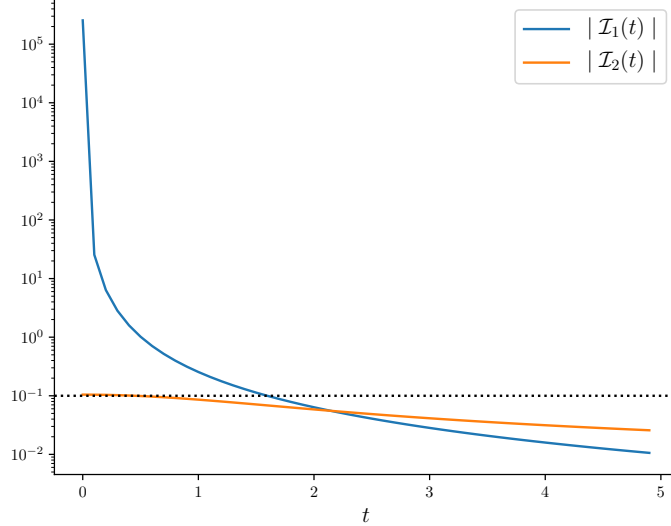
Figure 6.3: *Plots of absolute values of $\mathcal{I}_1(t)$ and $\mathcal{I}_2(t)$ (Eq. 6.50) for the parameters of the lowest temperature bath in Fig. 3.17. The parameters are $s = 1$, $\Gamma = 1.6$, $\beta = 2.0$, $\omega_c = 1000$. The horizontal dotted line corresponds to the value of ε, which is $\varepsilon = 0.1$. From the plot it is clear that $\tau_B \sim 2$, which is the time by which both $\mathcal{I}_1(t)$ and $\mathcal{I}_2(t)$ have decayed to $O(\varepsilon)$. Time is measured in units of Ω_0^{-1} and energies are measured in units of Ω_0 (see Eq. 3.17).*

that $\tau_B \sim 0.1$ (both $\tau_{B_1} \sim 0.1, \tau_{B_2} \sim 0.1$), in units of ω_0^{-1}, irrespective of the chemical potential μ of the bath.

Finally, we look at the baths of Sec. 3.2. In this case, the bath spectral function is as given in Eq. 3.21,

$$\mathfrak{J}(\omega) = \Gamma \omega^s e^{-\omega/\omega_c} \theta(\omega) , \tag{6.52}$$

where ω_c gives the cut-off frequency and $\theta(\omega)$ is Heaviside step function. The cut-off frequency is considered very large so that the system energy levels near the edge of the bath spectrum correspond to extremely high energies, which do not really contribute to the system properties at the chosen set of temperatures and chemical potentials. Also, we have set $\mu_1 = \mu_2 = 0$. Our results are mainly for the Ohmic bath, i.e, for $s = 1$. The plots of absolute values of $\mathcal{I}_1(t)$ and $\mathcal{I}_2(t)$ for the parameters of the lowest temperature bath in Fig. 3.17 is shown in Fig. 6.3. From the figure, it is clear that $\tau_B \sim 2$, in units of Ω_0^{-1} (see Eq. 3.17).

For $s < 1$, $\mathcal{I}_2(t)$ has a divergence at small ω when chemical potential of Bose distribution is $\mu = 0$. As a result Born-Markov approximation fails. Note that when considering

the bath spectral function in Eq.. 6.51 for the bosonic case, $\mu = -2.5$ was taken so that $\mu < -2t_B$ $(t_B = 1)$. This ensures there is no divergence. If this condition was not satisfied, Born-Markov approximation would have failed in that case also.

6.7 From Green-Kubo formula to spread of correlations

If $\hat{\mathcal{H}}_S$ has time translation and time-reversal symmetries, and is 'local', the Green-Kubo formula Eq. 4.1 can be related to the spread of correlations. The proof of this is quite involved, and below we will go through the proof in detail, clearly mentioning the assumptions made.

Time-reversal symmetry of $\hat{\mathcal{H}}_S$ implies $\langle \hat{I}_S \rangle = 0$. This can be shown as follows. Let $\mathcal{T}$ time-reversal operator. $\hat{I}_S$ is odd under time-reversal, while $\hat{\mathcal{H}}_S$ and $\hat{N}_S$ are even under time-reversal. So,

$$
\begin{aligned}
\langle \hat{I}_S \rangle &= Tr(\frac{e^{-\beta(\hat{\mathcal{H}}_S - \mu \hat{N}_S)}}{Z} \hat{I}_S) = Tr(\mathcal{T} \frac{e^{-\beta(\hat{\mathcal{H}}_S - \mu \hat{N}_S)}}{Z} \mathcal{T}^{-1} \hat{I}_S) \\
&= Tr(\frac{e^{-\beta(\hat{\mathcal{H}}_S - \mu \hat{N}_S)}}{Z} \mathcal{T}^{-1} \hat{I}_S \mathcal{T}) = -Tr(\frac{e^{-\beta(\hat{\mathcal{H}}_S - \mu \hat{N}_S)}}{Z} \hat{I}_S) = -\langle \hat{I}_S \rangle \\
&\Rightarrow \langle \hat{I}_S \rangle = 0
\end{aligned}
\tag{6.53}
$$

We start with the mixing assumption which is generically expected to be valid in the thermodynamic limit. This says that, given two arbitrary operators $\hat{Q}_1$ and $\hat{Q}_2$,

$$
\lim_{t \to \infty} \langle \hat{Q}_1(t) \hat{Q}_2(0) \rangle = \lim_{t \to \infty} \langle \hat{Q}_1(t) \rangle \langle \hat{Q}_2 \rangle
\tag{6.54}
$$

Thus, using Eqs. 6.53, 6.54, we have,

$$
\lim_{t \to \infty} \langle \hat{I}_S(t) \hat{I}_S(0) \rangle = 0.
\tag{6.55}
$$

Since the total number of particles in the system is conserved, one can show $[\hat{I}_S, \hat{N}_S] = 0$ (even though $[\hat{I}_S, \hat{\mathcal{H}}_S] \neq 0$). For two operators, $\hat{Q}_1, \hat{Q}_2$ which commute with $\hat{N}_S$,

$$
\begin{aligned}
\langle \hat{Q}_1(t) \hat{Q}_2(t) \rangle &= \frac{Tr(e^{-\beta(\hat{\mathcal{H}}_S - \mu \hat{N})} \hat{Q}_1(t) \hat{Q}_2(t))}{Z} = \frac{Tr(e^{-\beta \hat{\mathcal{H}}_S} \hat{Q}_1(t) e^{\beta \hat{\mathcal{H}}_S} e^{-\beta(\hat{\mathcal{H}}_S - \mu \hat{N}_S)} \hat{Q}_2(t))}{Z} \\
&= \langle \hat{Q}_1(t) \hat{Q}_2(t + i\beta) \rangle,
\end{aligned}
\tag{6.56}
$$

where in the second line we have used the fact that $[\hat{Q}_1, \hat{N}_S] = 0$.

$$
\begin{aligned}
\sigma_{GK} &= \lim_{\tau \to \infty} \lim_{L \to \infty} \int_0^\tau dt \int_0^\beta d\lambda \langle \hat{I}_S(-i\lambda)\hat{I}_S(t)\rangle / L \\
&= \lim_{\tau \to \infty} \lim_{L \to \infty} \int_0^\tau dt \int_0^\beta d\lambda \langle \hat{I}_S(t)\hat{I}_S(i(\beta - \lambda))\rangle / L \quad \text{(Using Eq. 6.56)} \\
&= \lim_{\tau \to \infty} \lim_{L \to \infty} \int_0^\tau dt \int_0^\beta d\lambda \langle \hat{I}_S(t)\hat{I}_S(i\lambda)\rangle / L \quad (\lambda \to \beta - \lambda) \\
&= \lim_{\tau \to \infty} \lim_{L \to \infty} \int_0^\tau dt \int_0^\beta d\lambda \langle \hat{I}_S(-i\lambda)\hat{I}_S(-t)\rangle / L \quad \text{(Using time-reversal)} \\
&= \lim_{\tau \to \infty} \lim_{L \to \infty} \int_{-\tau}^0 dt \int_0^\beta d\lambda \langle \hat{I}_S(-i\lambda)\hat{I}_S(t)\rangle / L \quad (t \to -t) \\
&= \lim_{\tau \to \infty} \lim_{L \to \infty} \frac{1}{2} \int_{-\tau}^\tau dt \int_0^\beta d\lambda \langle \hat{I}_S(-i\lambda)\hat{I}_S(t)\rangle / L \\
&= \lim_{\tau \to \infty} \lim_{L \to \infty} \frac{1}{2} \int_0^\beta d\lambda \left[\int_{-\tau+i\lambda}^{\tau+i\lambda} dz \langle \hat{I}_S(0)\hat{I}_S(z)\rangle / L \right].
\end{aligned} \tag{6.57}
$$

The last step requires time-translation by $t + i\lambda$ and changing variable to $z \to t + i\lambda$. We can now do the integration over z using contour integration. For this, we choose a contour of the rectangle in complex-plane joining the points $(-\tau, i\lambda)$, $(\tau, i\lambda)$, $(\tau, 0)$, $(-\tau, 0)$. Since this contour integral is zero (assuming no singularities), we have

$$
\int_{-\tau+i\lambda}^{\tau+i\lambda} dz \langle \hat{I}_S(0)\hat{I}_S(z)\rangle = \int_{-\tau}^\tau dt \langle \hat{I}_S(0)\hat{I}_S(t)\rangle + i \int_0^\lambda dy \left[\langle \hat{I}_S(0)\hat{I}_S(\tau + iy)\rangle - \langle \hat{I}_S(0)\hat{I}_S(-\tau + iy)\rangle \right] \tag{6.58}
$$

By Eq. 6.55 and time-translation symmetry, we have

$$
\lim_{\tau \to \infty} \langle \hat{I}_S(0)\hat{I}_S(\pm\tau + iy)\rangle = \langle \hat{I}_S(0)\rangle \langle \hat{I}_S(\pm\infty)\rangle = 0, \tag{6.59}
$$

Hence, substituting in Eq. 6.57, we get

$$
\begin{aligned}
\sigma_{GK} &= \lim_{\tau \to \infty} \lim_{L \to \infty} \frac{\beta}{2} \int_{-\tau}^\tau dt \langle \hat{I}_S(0)\hat{I}_S(t)\rangle / L \\
&= \lim_{\tau \to \infty} \lim_{L \to \infty} \frac{\beta}{2} \left[\int_0^\tau dt \langle \hat{I}_S(0)\hat{I}_S(t)\rangle / L + \int_{-\tau}^0 dt \langle \hat{I}_S(0)\hat{I}_S(t)\rangle / L \right] \\
&= \lim_{\tau \to \infty} \lim_{L \to \infty} \frac{\beta}{2} \left[\int_0^\tau dt \langle \hat{I}_S(0)\hat{I}_S(t)\rangle / L + \int_{-\tau}^0 dt \langle \hat{I}_S(-t)\hat{I}_S(0)\rangle / L \right] \quad \text{(time-translation by } -t) \\
&= \lim_{\tau \to \infty} \lim_{L \to \infty} \frac{\beta}{2} \int_0^\tau dt \left[\langle \hat{I}_S(0)\hat{I}_S(t)\rangle + \langle \hat{I}_S(t)\hat{I}_S(0)\rangle \right] / L \quad \text{(change variable } t \to -t) \\
&= \lim_{\tau \to \infty} \lim_{L \to \infty} \beta \int_0^\tau dt \, \text{Re}\left(\langle \hat{I}_S(t)\hat{I}_S(0)\rangle \right) / L \tag{6.60}
\end{aligned}
$$

where Re(...) stands for real part, and in the last step we have used the fact that $\hat{I}_S$ is Hermitian so, $\left(\hat{I}_S(t)\hat{I}_S(0) \right)^\dagger = \hat{I}_S(0)\hat{I}_S(t)$.

128

Now, let us assume that the system Hamiltonian is 'local', i.e, it does not have long range terms. Such a system can be broken up into surfaces transverse to direction of current flow such that

$$\hat{N}_S = \sum_{p=-\infty}^{\infty} \hat{n}_p, \quad \frac{d\hat{n}_p}{dt} = \hat{I}_p - \hat{I}_{p-1}, \quad \hat{I}_S = \sum_{p=-\infty}^{\infty} \hat{I}_p \tag{6.61}$$

where $\hat{n}_p$ is the local particle density and $\hat{I}_p$ is the local current, and we have already assumed the thermodynamic limit. Then we observe that

$$\frac{d}{dt_1}\frac{d}{dt_2}\left[\sum_{p,q=-\infty}^{\infty} (p-q)^2 \langle \hat{n}_p(t_1)\hat{n}_q(t_2)\rangle\right] = \sum_{p,q=-\infty}^{\infty} (p-q)^2 \langle \left(\hat{I}_p(t_1) - \hat{I}_{p-1}(t_1)\right)\left(\hat{I}_q(t_2) - \hat{I}_{q-1}(t_2)\right)\rangle$$

$$= \sum_{p,q=-\infty}^{\infty} \langle \hat{I}_p(t_1)\hat{I}_q(t_2)\rangle \left[(p-q)^2 - (p-q+1)^2 - (p-q-1)^2 + (p-q)^2\right] \quad \text{(Shifting indices)}$$

$$= -2\sum_{p,q=-\infty}^{\infty} \langle \hat{I}_p(t_1)\hat{I}_q(t_2)\rangle. \tag{6.62}$$

We define $\tau = t_1 - t_2$, then $\frac{d}{dt_1} = \frac{d}{d\tau}$, $\frac{d}{dt_2} = -\frac{d}{d\tau}$. Using time translation symmetry, this gives,

$$\frac{d^2}{d\tau^2}\left[\sum_{p,q=-\infty}^{\infty} (p-q)^2 \langle \hat{n}_p(\tau)\hat{n}_q(0)\rangle\right] = 2\sum_{p,q=-\infty}^{\infty} \langle \hat{I}_p(\tau)\hat{I}_q(0)\rangle$$

$$\Rightarrow \frac{d^2}{d\tau^2}\left[\sum_{x,q=-\infty}^{\infty} x^2 \langle \hat{n}_{x+q}(\tau)\hat{n}_q(0)\rangle\right] = 2\langle \hat{I}_S(\tau)\hat{I}_S(0)\rangle$$

$$\Rightarrow \frac{d}{d\tau}\left[\sum_{x,q=-\infty}^{\infty} x^2 \langle \hat{n}_{x+q}(\tau)\hat{n}_q(0)\rangle\right] = 2\int_0^{\tau} dt \langle \hat{I}_S(t)\hat{I}_S(0)\rangle. \tag{6.63}$$

Using Eq. 6.63 and Eq. 6.60, we have,

$$\sigma_{GK} = \lim_{\tau\to\infty}\lim_{L\to\infty}\frac{\beta}{2}\frac{d}{d\tau}\left[\sum_{x,q=-L/2}^{L/2} x^2 \text{Re}\left(\langle \hat{n}_{x+q}(\tau)\hat{n}_q(0)\rangle\right)\right]/L \tag{6.64}$$

Note that the above Eq. 6.63 holds strictly in the thermodynamic limit. For a finite system of length L, there will be some corrections from the boundary terms. However, the finite-size version of Eq. 6.63 in the RHS of can be used because those terms are suppressed by the factor $1/L$ as $L \to \infty$.

Till now, we have not used any spatial translation symmetry. Now, if we further assume that the system has spatial translation symmetry, we have

$$\sigma_{GK} = \lim_{\tau\to\infty}\frac{\beta}{2}\frac{d}{d\tau}m_2^{nn}(\tau), \quad m_2^{nn}(\tau) = \sum_{x=-\infty}^{\infty} x^2 \text{Re}\left(C(x,t)\right), \quad C(x,t) = \langle \hat{n}_x(\tau)\hat{n}_0(0)\rangle - \langle \hat{n}_x\rangle\langle \hat{n}_0\rangle$$

$$\tag{6.65}$$

Here we have used the fact that $\langle \hat{n}_x \rangle \langle \hat{n}_0 \rangle$ is time independent and hence its time-derivative is zero. $m_2^{nn}(\tau)$ is the 'second moment' of correlation function $\mathrm{Re}\,(C(x,t))$. Thus, σ_{GK} is depends on spread of density correlations with time.

Bibliography

[1] D. L. Underwood, W. E. Shanks, J. Koch, and A. A. Houck, "Low-disorder microwave cavity lattices for quantum simulation with photons," *Phys. Rev. A*, vol. 86, p. 023837, Aug 2012.

[2] M. Kulkarni, B. Öztop, and H. E. Türeci, "Cavity-mediated near-critical dissipative dynamics of a driven condensate," *Phys. Rev. Lett.*, vol. 111, p. 220408, Nov 2013.

[3] M. Aspelmeyer, T. J. Kippenberg, and F. Marquardt, "Cavity optomechanics," *Rev. Mod. Phys.*, vol. 86, pp. 1391–1452, Dec 2014.

[4] J. Stehlik, Y.-Y. Liu, C. Eichler, T. R. Hartke, X. Mi, M. J. Gullans, J. M. Taylor, and J. R. Petta, "Double quantum dot floquet gain medium," *Phys. Rev. X*, vol. 6, p. 041027, Nov 2016.

[5] L. Venkataraman, J. E. Klare, C. Nuckolls, M. S. Hybertsen, and M. L. Steigerwald, "Dependence of single-molecule junction conductance on molecular conformation," *Nature*, vol. 442, no. 7105, pp. 904–907, 2006.

[6] M. Boissonneault, J. M. Gambetta, and A. Blais, "Dispersive regime of circuit qed: Photon-dependent qubit dephasing and relaxation rates," *Phys. Rev. A*, vol. 79, p. 013819, Jan 2009.

[7] A. J. Hoffman, S. J. Srinivasan, S. Schmidt, L. Spietz, J. Aumentado, H. E. Türeci, and A. A. Houck, "Dispersive photon blockade in a superconducting circuit," *Phys. Rev. Lett.*, vol. 107, p. 053602, Jul 2011.

[8] T. R. Hartke, Y.-Y. Liu, M. J. Gullans, and J. R. Petta, "Microwave detection of electron-phonon interactions in a cavity-coupled double quantum dot," *Phys. Rev. Lett.*, vol. 120, p. 097701, Feb 2018.

[9] K. L. Hur, L. Henriet, A. Petrescu, K. Plekhanov, G. Roux, and M. Schir, "Many-body quantum electrodynamics networks: Non-equilibrium condensed matter physics with light," *Comptes Rendus Physique*, vol. 17, no. 8, pp. 808 – 835, 2016. Polariton physics / Physique des polaritons.

[10] Z.-L. Xiang, S. Ashhab, J. Q. You, and F. Nori, "Hybrid quantum circuits: Superconducting circuits interacting with other quantum systems," *Rev. Mod. Phys.*, vol. 85, pp. 623–653, Apr 2013.

[11] Y.-Y. Liu, J. Stehlik, C. Eichler, X. Mi, T. R. Hartke, M. J. Gullans, J. M. Taylor, and J. R. Petta, "Threshold dynamics of a semiconductor single atom maser," *Phys. Rev. Lett.*, vol. 119, p. 097702, Aug 2017.

[12] D. Segal and A. Nitzan, "Spin-boson thermal rectifier," *Phys. Rev. Lett.*, vol. 94, p. 034301, Jan 2005.

[13] D. Segal and A. Nitzan, "Heat rectification in molecular junctions," *The Journal of Chemical Physics*, vol. 122, no. 19, p. 194704, 2005.

[14] B. Xu and Y. Dubi, "Negative differential conductance in molecular junctions: an overview of experiment and theory," *Journal of Physics: Condensed Matter*, vol. 27, no. 26, p. 263202, 2015.

[15] A. Dhar and D. Sen, "Nonequilibrium green's function formalism and the problem of bound states," *Phys. Rev. B*, vol. 73, p. 085119, Feb 2006.

[16] A. Dhar and D. Roy, "Heat transport in harmonic lattices," *Journal of Statistical Physics*, vol. 125, pp. 801–820, Nov 2006.

[17] I. Weymann, B. R. Bułka, and J. Barnaś, "Dark states in transport through triple quantum dots: The role of cotunneling," *Phys. Rev. B*, vol. 83, p. 195302, May 2011.

[18] K. Wrześniewski and I. Weymann, "Dark states in spin-polarized transport through triple quantum dot molecules," *Phys. Rev. B*, vol. 97, p. 075425, Feb 2018.

[19] H. Haug and A.-P. Jauho, *Quantum Kinetics in Transport and Optics of Semiconductors*. Springer, Berlin, Heidelberg, 2008.

[20] G. W. Ford, M. Kac, and P. Mazur, "Statistical mechanics of assemblies of coupled oscillators," *Journal of Mathematical Physics*, vol. 6, no. 4, pp. 504–515, 1965.

[21] H.-P. Breuer and F. Petruccione, *The Theory of Open Quantum Systems*. Oxford University Press, 2002.

[22] A. Rivas and S. F. Hulega, *Open Quantum Systems*. Springer,Berlin, Heidelberg, 2012.

[23] H. J. Carmichael, *Statistical Methods in Quantum Optics*. Springer, 2002.

[24] W.-M. Zhang, P.-Y. Lo, H.-N. Xiong, M. W.-Y. Tu, and F. Nori, "General non-markovian dynamics of open quantum systems," *Phys. Rev. Lett.*, vol. 109, p. 170402, Oct 2012.

[25] V. Gorini, A. Kossakowski, and E. C. G. Sudarshan, "Completely positive dynamical semigroups of nlevel systems," *Journal of Mathematical Physics*, vol. 17, no. 5, pp. 821–825, 1976.

[26] G. Lindblad, "On the generators of quantum dynamical semigroups," *Communications in Mathematical Physics*, vol. 48, pp. 119–130, Jun 1976.

[27] C. H. Fleming and N. I. Cummings, "Accuracy of perturbative master equations," *Phys. Rev. E*, vol. 83, p. 031117, Mar 2011.

[28] A.-P. Jauho, N. S. Wingreen, and Y. Meir, "Time-dependent transport in interacting and noninteracting resonant-tunneling systems," *Phys. Rev. B*, vol. 50, pp. 5528–5544, Aug 1994.

[29] Y. Zhu, J. Maciejko, T. Ji, H. Guo, and J. Wang *Phys. Rev. B*, vol. 71, p. 075317, 2005.

[30] J. Maciejko, J. Wang, and H. Guo, "Time-dependent quantum transport far from equilibrium: An exact nonlinear response theory," *Phys. Rev. B*, vol. 74, p. 085324, Aug 2006.

[31] M. W. Y. Tu and W.-M. Zhang, "Non-markovian decoherence theory for a double-dot charge qubit," *Phys. Rev. B*, vol. 78, p. 235311, Dec 2008.

[32] J. Jinshuang, W.-Y. T. Matisse, Z. Wei-Min, and Y. YiJing, "Non-equilibrium quantum theory for nanodevices based on the feynmanvernon influence functional," *New Journal of Physics*, vol. 12, no. 8, p. 083013, 2010.

[33] M. Ridley, A. MacKinnon, and L. Kantorovich *Phys. Rev. B*, vol. 91, p. 125433, 2015.

[34] M. Ridley, A. MacKinnon, and L. Kantorovich *Phys. Rev. B*, vol. 93, p. 205408, 2016.

[35] M. Ridley, A. MacKinnon, and L. Kantorovich, "Partition-free theory of time-dependent current correlations in nanojunctions in response to an arbitrary time-dependent bias," *Phys. Rev. B*, vol. 95, p. 165440, Apr 2017.

[36] P.-Y. Yang and W.-M. Zhang *arXiv:1611.04242*, 2016.

[37] E. Perfetto, D. Sangalli, A. Marini, and G. Stefanucci *Phys. Rev. B*, vol. 92, p. 205304, 2015.

[38] H. K. Yadalam and U. Harbola *Phys. Rev. B*, vol. 93, p. 035312, 2016.

[39] E. Perfetto, A.-M. Uimonen, R. van Leeuwen, and G. Stefanucci *Journal of Physics: Conference Series*, vol. 696, no. 1, p. 012004, 2016.

[40] S.-A. Biehs and G. S. Agarwal, "Dynamical quantum theory of heat transfer between plasmonic nanosystems," *J. Opt. Soc. Am. B*, vol. 30, pp. 700–707, Mar 2013.

[41] A. Asadian, D. Manzano, M. Tiersch, and H. J. Briegel, "Heat transport through lattices of quantum harmonic oscillators in arbitrary dimensions," *Phys. Rev. E*, vol. 87, p. 012109, Jan 2013.

[42] R. Dümcke and H. Spohn, "The proper form of the generator in the weak coupling limit," *Zeitschrift für Physik B Condensed Matter*, vol. 34, pp. 419–422, Dec 1979.

[43] H. Wichterich, M. J. Henrich, H.-P. Breuer, J. Gemmer, and M. Michel, "Modeling heat transport through completely positive maps," *Phys. Rev. E*, vol. 76, p. 031115, Sep 2007.

[44] M. Esposito, U. Harbola, and S. Mukamel, "Fluctuation theorem for counting statistics in electron transport through quantum junctions," *Phys. Rev. B*, vol. 75, p. 155316, Apr 2007.

[45] A. Levy and R. Kosloff, "The local approach to quantum transport may violate the second law of thermodynamics," *EPL (Europhysics Letters)*, vol. 107, no. 2, p. 20004, 2014.

[46] B. Warner, F. El Hallak, H. Prüser, J. Sharp, M. Persson, A. J. Fisher, and C. F. Hirjibehedin, "Tunable magnetoresistance in an asymmetrically coupled single-molecule junction," *Nature nanotechnology*, vol. 10, no. 3, pp. 259–263, 2015.

[47] G. Zhang, M. A. Ratner, and M. G. Reuter, "Is molecular rectification caused by asymmetric electrode couplings or by a molecular bias drop?," *Jour. Phys. Chem.*, vol. 119, no. 11, pp. 6254–6260, 2015.

[48] K. Wang, J. Zhou, J. M. Hamill, and B. Xu, "Measurement and understanding of single-molecule break junction rectification caused by asymmetric contacts," *Jour. Chem. Phys.*, vol. 141, no. 5, p. 054712, 2014.

[49] J. Trasobares, D. Théron, and N. Clément, "A 17ghz molecular rectifier," *Nature Communications*, vol. 7, p. 12850, 2016.

[50] M. J. Hartmann and M. B. Plenio, "Strong photon nonlinearities and photonic mott insulators," *Phys. Rev. Lett.*, vol. 99, p. 103601, Sep 2007.

[51] Z. Ling, L. Zhong-Ju, Y. Wei-Bin, and M. Qing-Xia, "Effective bosehubbard interaction with enhanced nonlinearity in an array of coupled cavities," *Chinese Physics B*, vol. 20, no. 7, p. 074205, 2011.

[52] D. Schwarzer, P. Kutne, C. Schrder, and J. Troe, "Intramolecular vibrational energy redistribution in bridged azulene-anthracene compounds: Ballistic energy transport through molecular chains," *The Journal of Chemical Physics*, vol. 121, no. 4, pp. 1754–1764, 2004.

[53] R. Y. Wang, R. A. Segalman, and A. Majumdar, "Room temperature thermal conductance of alkanedithiol self-assembled monolayers," *Applied Physics Letters*, vol. 89, no. 17, p. 173113, 2006.

[54] T. Meier, F. Menges, P. Nirmalraj, H. Hölscher, H. Riel, and B. Gotsmann, "Length-dependent thermal transport along molecular chains," *Phys. Rev. Lett.*, vol. 113, p. 060801, Aug 2014.

[55] M. D. Losego, M. E. Grady, N. R. Sottos, D. Cahill, and P. Braun, "Effects of chemical bonding on heat transport across interfaces.," *Nat. Mater.*, vol. 11, p. 502, 2012.

[56] N. I. Rubtsova, C. M. Nyby, H. Zhang, B. Zhang, X. Zhou, J. Jayawickramarajah, A. L. Burin, and I. V. Rubtsov, "Room-temperature ballistic energy transport in molecules with repeating units," *The Journal of Chemical Physics*, vol. 142, no. 21, p. 212412, 2015.

[57] N. I. Rubtsova and I. V. Rubtsov, "Vibrational energy transport in molecules studied by relaxation-assisted two-dimensional infrared spectroscopy," *Annual Review of Physical Chemistry*, vol. 66, no. 1, pp. 717–738, 2015. PMID: 25747112.

[58] D. Segal and B. K. Agarwalla, "Vibrational heat transport in molecular junctions," *Annual Review of Physical Chemistry*, vol. 67, no. 1, pp. 185–209, 2016. PMID: 27215814.

[59] P. D. Drummond and D. F. Walls, "Quantum theory of optical bistability. i. nonlinear polarisability model," *Journal of Physics A: Mathematical and General*, vol. 13, no. 2, p. 725, 1980.

[60] F. Haake, H. Risken, C. Savage, and D. Walls, "Master equation for a damped nonlinear oscillator," *Phys. Rev. A*, vol. 34, pp. 3969–3973, Nov 1986.

[61] G. J. Milburn and C. A. Holmes, "Dissipative quantum and classical liouville mechanics of the anharmonic oscillator," *Phys. Rev. Lett.*, vol. 56, pp. 2237–2240, May 1986.

[62] H. Risken, C. Savage, F. Haake, and D. F. Walls, "Quantum tunneling in dispersive optical bistability," *Phys. Rev. A*, vol. 35, pp. 1729–1739, Feb 1987.

[63] R. Alicki, "Master equations for a damped nonlinear oscillator and the validity of the markovian approximation," *Phys. Rev. A*, vol. 40, pp. 4077–4081, Oct 1989.

[64] F. X. Kärtner and A. Schenzle, "Analytic solution for the dissipative anharmonic quantum oscillator and semiclassical analysis," *Phys. Rev. A*, vol. 48, pp. 1009–1019, Aug 1993.

[65] D. Segal, "Heat flow in nonlinear molecular junctions: Master equation analysis," *Phys. Rev. B*, vol. 73, p. 205415, May 2006.

[66] T. Ruokola and T. Ojanen, "Thermal conductance in a spin-boson model: Co-tunneling and low-temperature properties," *Phys. Rev. B*, vol. 83, p. 045417, Jan 2011.

[67] K. Saito and T. Kato, "Kondo signature in heat transfer via a local two-state system," *Phys. Rev. Lett.*, vol. 111, p. 214301, Nov 2013.

[68] D. Segal, "Heat transfer in the spin-boson model: A comparative study in the incoherent tunneling regime," *Phys. Rev. E*, vol. 90, p. 012148, Jul 2014.

[69] J. Thingna, J. L. García-Palacios, and J.-S. Wang, "Steady-state thermal transport in anharmonic systems: Application to molecular junctions," *Phys. Rev. B*, vol. 85, p. 195452, May 2012.

[70] D. He, J. Thingna, J.-S. Wang, and B. Li, "Quantum thermal transport through anharmonic systems: A self-consistent approach," *Phys. Rev. B*, vol. 94, p. 155411, Oct 2016.

[71] A. Dhar, K. Saito, and P. Hänggi, "Nonequilibrium density-matrix description of steady-state quantum transport," *Phys. Rev. E*, vol. 85, p. 011126, Jan 2012.

[72] Y.-Y. Liu, J. Stehlik, C. Eichler, M. J. Gullans, J. M. Taylor, and J. R. Petta, "Semiconductor double quantum dot micromaser," *Science*, vol. 347, no. 6219, pp. 285–287, 2015.

[73] L. Zhang, Y. Yan, C.-Q. Wu, J.-S. Wang, and B. Li, "Reversal of thermal rectification in quantum systems," *Phys. Rev. B*, vol. 80, p. 172301, Nov 2009.

[74] J. Wang, Y. Zhang, and H. Zhao, "Non-gaussian normal diffusion induced by delocalization," *Phys. Rev. E*, vol. 93, p. 032144, Mar 2016.

[75] G. Forte, F. Cecconi, and A. Vulpiani, "Non-anomalous diffusion is not always gaussian," *The European Physical Journal B*, vol. 87, no. 5, p. 102, 2014.

[76] M. V. Chubynsky and G. W. Slater, "Diffusing diffusivity: A model for anomalous, yet brownian, diffusion," *Phys. Rev. Lett.*, vol. 113, p. 098302, Aug 2014.

[77] J. Kim, C. Kim, and B. J. Sung, "Simulation study of seemingly fickian but heterogeneous dynamics of two dimensional colloids," *Phys. Rev. Lett.*, vol. 110, p. 047801, Jan 2013.

[78] B. Wang, J. Kuo, S. C. Bae, and S. Granick, "When Brownian diffusion is not Gaussian," *Nature Materials*, vol. 11, pp. 481–485, June 2012.

[79] B. Wang, S. M. Anthony, S. C. Bae, and S. Granick, "Anomalous yet brownian," *Proceedings of the National Academy of Sciences*, vol. 106, no. 36, pp. 15160–15164, 2009.

[80] K. H. Andersen, P. Castiglione, A. Mazzino, and A. Vulpiani, "Simple stochastic models showing strong anomalous diffusion," *Eur. Phys. J. B*, vol. 18, no. 3, pp. 447–452, 2000.

[81] X. P. Kong and E. G. D. Cohen, "Anomalous diffusion in a lattice-gas wind-tree model," *Phys. Rev. B*, vol. 40, pp. 4838–4845, 1989.

[82] H. P. Lüschen, P. Bordia, S. Scherg, F. Alet, E. Altman, U. Schneider, and I. Bloch, "Observation of slow dynamics near the many-body localization transition in one-dimensional quasiperiodic systems," *Phys. Rev. Lett.*, vol. 119, p. 260401, Dec 2017.

[83] H. P. Lüschen, P. Bordia, S. S. Hodgman, M. Schreiber, S. Sarkar, A. J. Daley, M. H. Fischer, E. Altman, I. Bloch, and U. Schneider, "Signatures of many-body localization in a controlled open quantum system," *Phys. Rev. X*, vol. 7, p. 011034, Mar 2017.

[84] M. Schreiber, S. S. Hodgman, P. Bordia, H. P. Lüschen, M. H. Fischer, R. Vosk, E. Altman, U. Schneider, and I. Bloch, "Observation of many-body localization of interacting fermions in a quasirandom optical lattice," *Science*, vol. 349, no. 6250, pp. 842–845, 2015.

[85] C. D. Érrico, M. Moratti, E. Lucioni, L. Tanzi, B. Deissler, M. Inguscio, G. Modugno, M. B. Plenio, and F. Caruso, "Quantum diffusion with disorder, noise and interaction," *New Journal of Physics*, vol. 15, no. 4, p. 045007, 2013.

[86] Y. E. Kraus, Z. Ringel, and O. Zilberberg, "Four-dimensional quantum hall effect in a two-dimensional quasicrystal," *Phys. Rev. Lett.*, vol. 111, p. 226401, Nov 2013.

[87] M. Verbin, O. Zilberberg, Y. E. Kraus, Y. Lahini, and Y. Silberberg, "Observation of topological phase transitions in photonic quasicrystals," *Phys. Rev. Lett.*, vol. 110, p. 076403, Feb 2013.

[88] Y. E. Kraus, Y. Lahini, Z. Ringel, M. Verbin, and O. Zilberberg, "Topological states and adiabatic pumping in quasicrystals," *Phys. Rev. Lett.*, vol. 109, p. 106402, Sep 2012.

[89] Y. Lahini, R. Pugatch, F. Pozzi, M. Sorel, R. Morandotti, N. Davidson, and Y. Silberberg, "Observation of a localization transition in quasiperiodic photonic lattices," *Phys. Rev. Lett.*, vol. 103, p. 013901, Jun 2009.

[90] G. Roati, C. D. Érrico, L. Fallani, M. Fattori, C. Fort, M. Zaccanti, G. Modugno, M. Modugno, and M. Inguscio, "Anderson localization of a non-interacting bose-einstein condensate," *Nature*, vol. 453, p. 895, Jun 2008.

[91] D. R. Hofstadter, "Energy levels and wave functions of bloch electrons in rational and irrational magnetic fields," *Phys. Rev. B*, vol. 14, pp. 2239–2249, Sep 1976.

[92] Y. E. Kraus and O. Zilberberg, "Topological equivalence between the fibonacci quasicrystal and the harper model," *Phys. Rev. Lett.*, vol. 109, p. 116404, Sep 2012.

[93] A. Avila and S. Jitomirskaya, "The ten martini problem," *Annals of Mathematics*, vol. 170, no. 1, pp. 303–342, 2009.

[94] Y. Last, "Zero measure spectrum for the almost mathieu operator," *Communications in Mathematical Physics*, vol. 164, no. 2, pp. 421–432, 1994.

[95] S. Aubry and G. Andre *Ann. Israel Phys. Soc*, vol. 3, p. 18, 1980.

[96] P. G. Harper, "Single band motion of conduction electrons in a uniform magnetic field," *Proceedings of the Physical Society. Section A*, vol. 68, no. 10, p. 874, 1955.

[97] H. Hiramoto and S. Abe, "Dynamics of an electron in quasiperiodic systems. i. fibonacci model," *Journal of the Physical Society of Japan*, vol. 57, no. 1, pp. 230–240, 1988.

[98] J. Zhong, R. B. Diener, D. A. Steck, W. H. Oskay, M. G. Raizen, E. W. Plummer, Z. Zhang, and Q. Niu, "Shape of the quantum diffusion front," *Phys. Rev. Lett.*, vol. 86, pp. 2485–2489, 2001.

[99] G. S. Ng and T. Kottos, "Wavepacket dynamics of the nonlinear harper model," *Phys. Rev. B*, vol. 75, p. 205120, May 2007.

[100] R. Ketzmerick, K. Kruse, S. Kraut, and T. Geisel, "What determines the spreading of a wave packet?," *Phys. Rev. Lett.*, vol. 79, pp. 1959–1963, Sep 1997.

[101] S. Ostlund, R. Pandit, D. Rand, H. J. Schellnhuber, and E. D. Siggia, "One-dimensional schrödinger equation with an almost periodic potential," *Phys. Rev. Lett.*, vol. 50, pp. 1873–1876, Jun 1983.

[102] F. Evers and A. D. Mirlin, "Anderson transitions," *Rev. Mod. Phys.*, vol. 80, pp. 1355–1417, Oct 2008.

[103] W. De Roeck, A. Dhar, F. Huveneers, and M. Schütz, "Step density profiles in localized chains," *Journal of Statistical Physics*, vol. 167, no. 5, pp. 1143–1163, 2017.

[104] C. Monthus, "Boundary-driven lindblad dynamics of random quantum spin chains : strong disorder approach for the relaxation, the steady state and the current," *arXiv:1701.02102*, 2017.

[105] D.-L. Deng, S. Ganeshan, X. Li, R. Modak, S. Mukerjee, and J. H. Pixley, "Many-body localization in incommensurate models with a mobility edge," *arXiv:1612.00976*, 2016.

[106] X. Li, J. H. Pixley, D.-L. Deng, S. Ganeshan, and S. Das Sarma, "Quantum nonergodicity and fermion localization in a system with a single-particle mobility edge," *Phys. Rev. B*, vol. 93, p. 184204, May 2016.

[107] X. Li, S. Ganeshan, J. H. Pixley, and S. Das Sarma, "Many-body localization and quantum nonergodicity in a model with a single-particle mobility edge," *Phys. Rev. Lett.*, vol. 115, p. 186601, Oct 2015.

[108] R. Modak and S. Mukerjee, "Many-body localization in the presence of a single-particle mobility edge," *Phys. Rev. Lett.*, vol. 115, p. 230401, Dec 2015.

[109] S. Ganeshan, J. H. Pixley, and S. Das Sarma, "Nearest neighbor tight binding models with an exact mobility edge in one dimension," *Phys. Rev. Lett.*, vol. 114, p. 146601, 2015.

[110] Sun, M. L., Wang, G., Li, N. B., and Nakayama, T., "Localization-delocalization transition in self-dual quasi-periodic lattices," *EPL*, vol. 110, no. 5, p. 57003, 2015.

[111] M. Johansson, "Comment on localization-delocalization transition in self-dual quasi-periodic lattices by sun m. l. et al.," *EPL (Europhysics Letters)*, vol. 112, no. 1, p. 17002, 2015.

[112] S. Nag and A. Garg, "Many-body mobility edges in a one-dimensional model of interacting fermions," *arXiv:1701.00236v2*, 2017.

[113] J. Biddle and S. Das Sarma, "Predicted mobility edges in one-dimensional incommensurate optical lattices: An exactly solvable model of anderson localization," *Phys. Rev. Lett.*, vol. 104, p. 070601, Feb 2010.

[114] J. Biddle, D. J. Priour, B. Wang, and S. Das Sarma, "Localization in one-dimensional lattices with non-nearest-neighbor hopping: Generalized anderson and aubry-andré models," *Phys. Rev. B*, vol. 83, p. 075105, Feb 2011.

[115] X. Li, X. Li, and S. D. Sarma, "Mobility edges in 1d bichromatic incommensurate potentials," *arXiv:1704.04498*, 2017.

[116] S. Gopalakrishnan, "Self-dual quasiperiodic systems with power-law hopping," *arXiv:1706.05382*, 2017.

[117] T. Mishra, R. Shashidhara, T. Guha Sarkar, and J. N. Bandyopadhyay, "Phase transition in an aubry-andré system with a rapidly oscillating magnetic field," *Phys. Rev. A*, vol. 94, p. 053612, Nov 2016.

[118] H. P. Lüschen, S. Scherg, T. Kohlert, M. Schreiber, P. Bordia, X. Li, S. Das Sarma, and I. Bloch, "Exploring the single-particle mobility edge in a one-dimensional quasiperiodic optical lattice," *arXiv:1709.03478*, 2017.

[119] K. Baumann, C. Guerlin, F. Brennecke, and T. Esslinger *Nature*, vol. 464, p. 1301, 2010.

[120] R. Mottl, F. Brennecke, K. Baumann, R. Landig, T. Donner, and T. Esslinger *Science*, vol. 336, p. 1570, 2012.

[121] M. Kulkarni, B. Öztop, and H. E. Türeci, "Cavity-mediated near-critical dissipative dynamics of a driven condensate," *Phys. Rev. Lett.*, vol. 111, p. 220408, 2013.

[122] F. Brennecke, R. Mottl, K. Baumann, R. Landig, T. Donner, and T. Esslinger, "Real-time observation of fluctuations at the driven-dissipative dicke phase transition," *Proceedings of the National Academy of Sciences*, vol. 110, no. 29, pp. 11763–11767, 2013.

[123] C. Karrasch, J. E. Moore, and F. Heidrich-Meisner, "Real-time and real-space spin and energy dynamics in one-dimensional spin-$\frac{1}{2}$ systems induced by local quantum quenches at finite temperatures," *Phys. Rev. B*, vol. 89, p. 075139, 2014.

[124] C. Tang and M. Kohmoto, "Global scaling properties of the spectrum for a quasiperiodic schrödinger equation," *Phys. Rev. B*, vol. 34, pp. 2041–2044, Aug 1986.

[125] J. M. Deutsch and O. Narayan, "Correlations and scaling in one-dimensional heat conduction," *Phys. Rev. E*, vol. 68, p. 041203, Oct 2003.

[126] S. G. Das, A. Dhar, and O. Narayan, "Heat conduction in the $\alpha\beta$ fermi–pasta–ulam chain," *Journal of Statistical Physics*, vol. 154, pp. 204–213, Jan 2014.

[127] L. G. G. V. Dias da Silva, C. H. Lewenkopf, E. Vernek, G. J. Ferreira, and S. E. Ulloa, "Conductance and kondo interference beyond proportional coupling," *Phys. Rev. Lett.*, vol. 119, p. 116801, Sep 2017.

[128] D. Hagenmüller, J. Schachenmayer, S. Schütz, C. Genes, and G. Pupillo, "Cavity-enhanced transport of charge," *Phys. Rev. Lett.*, vol. 119, p. 223601, Nov 2017.

[129] C. W. Groth, M. Wimmer, A. R. Akhmerov, and X. Waintal, "Kwant: a software package for quantum transport," *New Journal of Physics*, vol. 16, no. 6, p. 063065, 2014.

[130] M. Kulkarni, S. M. Hein, E. Kapit, and C. Aron, "Permanent spin currents in cavity-qubit systems," *Phys. Rev. B*, vol. 97, p. 064506, Feb 2018.

[131] K. Ptaszyński, "Nonrenewal statistics in transport through quantum dots," *Phys. Rev. B*, vol. 95, p. 045306, Jan 2017.

[132] A. K. Eissing, V. Meden, and D. M. Kennes, "Renormalization in periodically driven quantum dots," *Phys. Rev. Lett.*, vol. 116, p. 026801, Jan 2016.

[133] M. Žnidarič and M. Ljubotina, "Interaction instability of localization in quasiperiodic systems," *arXiv:1801.02955*, 2018.

[134] M. Žnidarič, A. Scardicchio, and V. K. Varma, "Diffusive and subdiffusive spin transport in the ergodic phase of a many-body localizable system," *Phys. Rev. Lett.*, vol. 117, p. 040601, Jul 2016.

[135] C. Carbogno, R. Ramprasad, and M. Scheffler, "Ab initio," *Phys. Rev. Lett.*, vol. 118, p. 175901, Apr 2017.

[136] C. Karrasch, D. M. Kennes, and F. Heidrich-Meisner, "Thermal conductivity of the one-dimensional fermi-hubbard model," *Phys. Rev. Lett.*, vol. 117, p. 116401, Sep 2016.

[137] V. Brosco, L. Benfatto, E. Cappelluti, and C. Grimaldi, "Unconventional dc transport in rashba electron gases," *Phys. Rev. Lett.*, vol. 116, p. 166602, Apr 2016.

[138] J. H. García, L. Covaci, and T. G. Rappoport, "Real-space calculation of the conductivity tensor for disordered topological matter," *Phys. Rev. Lett.*, vol. 114, p. 116602, Mar 2015.

[139] A. Kundu, A. Dhar, and O. Narayan, "The greenkubo formula for heat conduction in open systems," *Journal of Statistical Mechanics: Theory and Experiment*, vol. 2009, no. 03, p. L03001, 2009.

[140] O. Narayan, "Linear response formula for open systems," *Phys. Rev. E*, vol. 83, p. 061110, Jun 2011.

[141] J. B. Johnson, "Thermal agitation of electricity in conductors," *Phys. Rev.*, vol. 32, pp. 97–109, Jul 1928.

[142] H. Nyquist, "Thermal agitation of electric charge in conductors," *Phys. Rev.*, vol. 32, pp. 110–113, Jul 1928.

[143] P. L. Garrity and K. L. Stokes, "Thermal noise as a spectroscopic tool to determine transport properties," *Philosophical Magazine*, vol. 89, no. 25, pp. 2129–2147, 2009.

[144] D. S. Fisher and P. A. Lee, "Relation between conductivity and transmission matrix," *Phys. Rev. B*, vol. 23, pp. 6851–6854, Jun 1981.

[145] Y. Blanter and M. Büttiker, "Shot noise in mesoscopic conductors," *Physics Reports*, vol. 336, no. 1, pp. 1 – 166, 2000.

[146] K. Saito and A. Dhar, "Fluctuation theorem in quantum heat conduction," *Phys. Rev. Lett.*, vol. 99, p. 180601, Oct 2007.

[147] D. Chruściński and A. Kossakowski, "Non-markovian quantum dynamics: Local versus nonlocal," *Phys. Rev. Lett.*, vol. 104, p. 070406, Feb 2010.